

Black Hole Dynamics in Stellar Clusters

Markus Strickert

Lund Observatory
Lund University



2022-EXA196

Degree project of 60 higher education
credits (for a degree of Master)

June 2022

Supervisor: Abbas Askar

Lund Observatory
Box 43
SE-221 00 Lund
Sweden

Abstract

Star clusters can harbour many exotic objects, including black holes (BHs), X-ray binaries and blue straggler stars. In dense stellar environments like globular clusters (GCs), two-body relaxation drives their dynamical evolution, where gravitational interactions between stars strive to equalize their kinetic energy in the cluster. Theoretical studies have indicated that some of these clusters can retain a substantial number of stellar-mass black holes. As these black holes are more massive than typical stars, they segregate to the cluster centre due to dynamical friction and can form a black hole subsystem (BHS). In the last decade, several BH candidates have been observed in GCs.

In crowded cores of GCs, frequent gravitational encounters between stars and binary systems can occur. The exchange of energy in these interactions help sustain the cluster's core from collapsing. Abundant interactions among BHs can lead to their coalescence under the emission of gravitational waves to create intermediate-mass BHs (IMBHs) with masses of a few hundred to thousands of times the mass of our Sun. This project sheds light on how the presence of a BHS or an IMBH can influence the evolution and present-day observable properties of GCs.

We utilize results from over 1500 GC models that were simulated using the MOCCA code for evolving realistic star clusters. We correlate the clusters' dynamical state to the distributions and observable signatures of various stellar populations. Using the simulation output, we investigate cluster morphologies, retention rates of BHs and the distributions of observable stellar populations in the absence or presence of BHs or IMBHs. We quantify the segregation between stellar populations using the Δ_{r50} and A^+ parameters, which measure their relative distributions from the centre of the cluster. These parameters are used to quantify the difference in cumulative radial distributions between populations of main-sequence stars, blue stragglers and giants. We find that segregation is more enhanced in clusters with short relaxation times that are likely to be hosting an IMBH. Formation rates of blue stragglers are equally related to the cluster's relaxation time. An increased number of blue stragglers are found in heavily segregated ($A^+ > 0.05$) clusters with relaxation times ($\lesssim 1$ Gyr) having significant central surface brightness. Longer relaxation times and large half-mass radii are associated with clusters forming a BHS, with central surface brightness $< 10^4 L_{\odot} \text{pc}^{-2}$.

Clusters hosting IMBHs with large initial binary fractions (95 %) have a retained median binary fraction of $\approx 12\%$ in the innermost 0.05 parsecs that decreases in a power-law $\sim (r/r_{\text{hl}})^{-0.132}$ outwards, while BHS models have a slightly increased binary fractions in their cores of $\approx 14\%$ with a shallower slope of $\sim (r/r_{\text{hl}})^{-0.013}$. For clusters with initial binary fractions of 10 %, core binary fractions are still higher for BHS models, but have a faster depletion outwards compared to models hosting an IMBH. We conclude that clusters with initially short relaxation times are typically heavily segregated and contain IMBHs with fewer, but harder, binaries in their cores, contrary to systems with many BHs. Since clusters neither hosting a BHS nor an IMBH might also have short relaxation times and strong segregation, low binary fractions and large central surface brightness values can become a further indication for the presence of an IMBH.

Using segregation values for 50 known GCs in the Milky way, we predict numbers of BHs and masses of IMBHs by correlating the simulated numbers and masses of BHs with observed segregation. Comparable estimates with recently published works are produced, in particular, for NGC 3201, where we find an estimate of 64_{-45}^{+158} BHs retained in the cluster. We also note that 47 Tuc is best explained hosting an IMBH in our parameter space. We stress that the dynamics of BHs affect segregation on a more substantial grade than initial concentration and that short relaxation times and extensive segregation can be sufficient enough for ruling out the presence of a BHS, but further information about core binary fractions and central surface brightness is needed to identify clusters harbouring an IMBH.

Popular summary: Black hole dynamics in stellar clusters

Since the beginning of time, humankind has been fascinated by the night sky illuminated by distant stars. Even with the naked eye, one can see that stars are often grouped together in clusters. These dense environments can be the birthplace of many mysterious and exotic astrophysical objects in our Universe.

Star clusters are collections of stars born at the same time and are bound together by the influence of gravity. This attractive force acts over long distances and affects everything with energy or mass. In less crowded locations like our solar neighbourhood, stars are unlikely to gravitationally interact with each other. However, in more dense environments, like star clusters, where hundreds to millions of stars can be packed in very small volumes, stars can gravitationally interact. These gravitational encounters drive the dynamical evolution of dense star clusters. Early in the life of a star cluster, its most massive stars (that could be up to a few tens of the mass of our Sun) evolve first and end their lives to form black holes; these are objects so compact that not even light can escape their gravitational pull. This project sheds light on how the presence of black holes in star clusters can influence their long-term evolution and affect the observable properties of the cluster and its constituent stars.

In dense environments like star clusters, massive objects experience friction against the background of abundant lower mass stars and rapidly sink to the cluster's centre. In these dense centres, frequent gravitational encounters between stars allow them to exchange energy. These interactions can also result in collisions, where exotic stars can form due to the coalescence of multiple stellar objects. Since black holes are the most massive objects in a cluster, they will sink to the centre first and can interact to form systems of multiple black holes. If these are numerous enough, they can form a subsystem of black holes. Dynamical interactions between black holes can lead to the formation of binary systems containing two black holes on tight orbits around their common centre of mass. These can coalesce under the influence of gravity and the emission of gravitational waves. The latter produces ripples in space-time which have been observed by the LIGO/VIRGO ground-based gravitational wave detectors. In the densest star clusters, mergers between black holes can lead to the formation of an intermediate-mass black hole (IMBH) which is hundreds to thousands of times the mass of the Sun.

This project aims at finding differences in observable signatures of simulated star clusters depending on if the centre of the cluster hosts either a subsystem of black holes or an intermediate-mass black hole. Comparable to stars generating radiative energy through nuclear reactions in their cores, black holes in the core of a cluster exchange energy with lighter components that prevent the cluster from collapsing under its own gravity. If black holes are numerous, they energise bright components on wider orbits and increase the cluster's brightness in the outskirts. Conversely, their absence allows luminous stars to migrate to the cluster's centre. Thus, observational properties of clusters varies depending on their central objects.

We use computer simulations of hundreds of star cluster models with different initial sizes and densities to look for signatures of the presence of black holes or IMBHs. Since stars distribute differently under their influence, we can find the difference between the distributions of heavy as opposed to lighter stars and measure how *segregated* a cluster is. We investigate how these differences depend on the number of black holes in the clusters. We find that systems hosting IMBHs have a higher fraction of brighter stars in their cores. The presence of an IMBH also depletes the number of binaries in the cluster centre. By investigating the relationship between the number of black holes retained and the mass of these more massive black holes depending on their segregation, we predict the numbers and masses of black holes in observed clusters. Seeing that our current techniques still limit direct observations of black holes, these simulations can help resolve the signatures for the presence of some of the most exotic objects in the Universe.

Contents

Acknowledgements	i
Summary	iii
1 Stellar Clusters and Black Holes	1
1.1 Background	1
1.2 Globular clusters	1
1.2.1 Evolution and stability	3
1.2.2 Instability, core collapse and reversing core collapse	5
1.2.3 Black Hole Subsystems and Intermediate-Mass Black Holes	6
1.2.4 The role of BHS and IMBHs in clusters	8
1.2.5 Aim and physical importance	8
2 Numerical Tools and Algorithms	10
2.1 The MOCCA Code	10
2.1.1 Test Survey 2 - Multiple populations	11
2.1.2 MOCCA-SURVEY Database I	11
2.1.3 Problematic models	13
2.2 Data extraction and methods	14
2.2.1 The COCOA code - cluster projections	14
2.2.2 Initial setup - global properties	16
2.2.3 Comparison with observed data	16
2.2.4 Mass segregation	17
2.2.5 Segregation in stellar exotica	20
2.2.6 Prediction of BHS numbers and IMBH masses	21
3 Results	22
3.1 Global Properties	22
3.2 Observational Signatures	26
3.3 Mass Segregation	26
3.3.1 Segregation in stellar exotica	30
3.3.2 Summarizing segregation in different populations	34
3.4 Binary properties	36
3.4.1 Binary fraction distributions	36
3.4.2 Dynamical properties of binaries	38
3.5 Predicting BHs numbers and masses in observed GCs	40
3.5.1 47 Tuc (NGC 104)	42
3.5.2 NGC 3201	43
3.5.3 NGC 5466	44
3.5.4 NGC 6093	45
3.5.5 NGC 6535	45

3.5.6	NGC 6624	45
4	Discussion and conclusions	46
4.1	Discussion of the results	46
4.1.1	Observed data	46
4.1.2	Initial concentrations	47
4.1.3	Dynamical age as a probe for IMBHs	47
4.1.4	The choice of stellar populations	48
4.1.5	Comparing predictions between A^+ and Δ_{r50}	49
4.2	Uncertainties and future prospects	51
4.2.1	The MOCCA Code	51
4.2.2	Dynamical formation of CVs and BBH	51
4.2.3	Observed data	52
4.2.4	Future prospects and improvements	53
4.3	Conclusions	55
	Bibliography	57
5	Appendices	63
5.1	Influence radii and luminous binaries	63
5.2	Radial distributions	64
5.3	Observational signatures	65
5.4	Numbers and masses of BHs and IMBHs for Δ_{r50}	67

Acknowledgements

First and foremost, I want to express my deepest gratitude to my supervisor, Abbas Askar, for his guidance throughout the project and for his insight and expertise in the field. The project could not have been completed without you. I am furthermore grateful to my examiner and reviewer Ross Church and Diane Feuillet, for their valuable suggestions concerning the project. I would also like to assert my thankfulness to my fiance, Maja Frick, for cheering me up during the most stressful periods of the project. Special thanks to my friends, John Nilsson, Thomas Olausson, Lucas Knuthsson, Ashar Kamal, Daniel Magdalinski and Elin Sandvik for the late study evenings and discussions. Finally, I am very grateful to my family, which has always been there for me and given me the moral support needed to complete this project.

Summary

Stellar clusters host a variety of different populations of stars, binaries and exotic objects. Dynamical interactions in dense stellar systems, such as **globular clusters (GCs)** and **nuclear star clusters (NSCs)**, provide pathways for the formation of stellar exotica, such as **binary black holes (BBH)**, X-ray binaries, **blue stragglers (BSS)** and gravitational wave sources (Askar et al. 2017; Kremer et al. 2019b; Abbott et al. 2020). The most massive GCs can contain up to millions of stars and have high central densities of 10^5 to $10^6 M_{\odot} \text{pc}^{-3}$. Accordingly, gravitational encounters between stars can frequently occur in their cores and drive the dynamical state and structural evolution of the cluster (Davies 2013). In contrast, in less dense environments like our solar neighbourhood, close gravitational encounters are less likely to occur. The stellar richness of GCs makes them ideal laboratories for exploring the evolution of self-gravitating systems and investigating how the formation of stellar exotica can shape the dynamical evolution of a stellar cluster and its observable properties.

Several dynamical signatures have been used to understand the observable properties of stellar clusters by comparing them with simulations. Askar et al. (2017) have cross-matched simulated clusters with the observed GC of NGC 6535, revealing insights into the existence of **intermediate-mass black holes (IMBHs)**. Other studies correlate segregation of observable objects to the dynamical state of the cluster (Alessandrini et al. 2016; Weatherford et al. 2018; Kremer et al. 2019b; Weatherford et al. 2020). Many of these studies point out the importance of **black holes (BHs)** inside GCs and how their presence can strongly influence observable properties of the cluster.

The retention of BHs in stellar clusters has implications for the evolution and dynamics of the cluster and its components. Initial parameters influence the cluster’s evolution, yielding various possible outcomes in the formation and retention of BHs, exotic binaries, and potential sources of gravitational waves. Prior studies have indicated few retained BHs in GCs over time, partly due to primordial binaries segregating to the cluster’s core where they rapidly eject in dynamical interactions (e.g., Kulkarni et al. 1993). However, recent theoretical studies have revealed that under the right conditions, dynamical processes in massive star clusters can lead to the long-term retention of compact stellar remnants (e.g., Breen and Heggie 2013; Morscher et al. 2015). Several recent observational studies have also identified stellar-mass BH candidates in GCs (e.g., Strader et al. 2012; Bahramian et al. 2017; Giesers et al. 2018).

Simulating these dense systems requires studying dynamical interactions between millions of bodies, which via direct N -body methods is computationally costly. However, codes such as the MOCCA Code (Hypki and Giersz 2013), or the CMC code (Pattabiraman et al. 2013) allow us to study these systems with a Monte Carlo approach that lowers computational cost while still maintaining a high degree of accuracy. In this project, we are using stellar cluster models simulated with the MOCCA code, and primarily the MOCCA-Survey Database II (Maliszewski et al. 2021, hereafter MSD II), to examine how the distribution of observable stellar populations and exotica evolves in clusters in the presence or absence of dark remnants. We investigate

how the presence of IMBHs or a **subsystem of stellar-mass black holes (BHS)** shapes the dynamical evolution of a stellar cluster and its observable properties.

Clusters hosting a substantial BHS in the centre tend to have a lower central surface brightness and extended half-light and core radii. Interactions between BHs and lighter stellar components result in the dynamical heating of stars. Thus, one of the main aims of this project is to investigate the influence of retained BHs on the segregation and distribution of particular observable stars. We analyse snapshots from hundreds of simulated GC models to find observable properties that can diagnose the observational state of the cluster and determine whether it hosts dark remnants. We quantify the effects of dynamics in the presence of an IMBH or a BHS by looking at the segregation of main-sequence stars, giants, binaries, stellar exotica and compact objects. We aim at identifying apparent differences in segregation between clusters harbouring a BHS or an IMBH by correlating cumulative radial distributions of objects to the cluster's dynamical state.

By analysing simulated models with varying initial parameters, we intend to find differences in the distributions of binary populations depending on the central properties of the cluster and compare with published results (e.g., Aros et al. 2021). The results from our simulated models are cross-matched and compared with observations from Milky Way GCs (e.g., Harris 1996; Harris 2010; Bahramian et al. 2017; Baumgardt et al. 2020; Kremer et al. 2020). In this work, we determine observable properties from the simulated data from developed and automated analysis scripts. The results will also be used to make predictions on the retention of BHs in observed GCs and estimating masses of potential IMBHs. Data from previous MOCCA surveys are incorporated to increase the parameter space of our studies.

The structure of Chapter 1 is as follows: Section 1.1 gives a brief background to various stellar clusters, Section 1.2 introduces GCs, where their stability and evolution is explained in Section 1.2.1. Section 1.2.2 introduces the mechanisms for how these clusters can evolve towards core collapse, followed by how the dynamics of binaries inside the core can act against it. In Section 1.2.3.1, we introduce formation channels for BHS and the retention of BHs before analysing the formation channels of IMBHs in Section 1.2.3.2. We describe the connection of relaxation timescales to dynamical ages of clusters and introduce some useful nomenclature for the reader in Section 1.2.3.3. This subsection ends with a short summary of the role of BHS and IMBHs inside GCs in Section 1.2.4 before presenting the main aims and physical importance of the thesis in Section 1.2.5.

Abbreviations: Globular Clusters (GCs), Black Hole (BH), Binary Black Hole (BBH), Blue Straggler Star (BSS), Intermediate-mass Black Hole (IMBH), Stellar-mass Black Hole Subsystem (BHS), MOCCA-Database Survey II (MSD II), MOCCA-Database Survey I (MSD I), Supernova (SN), Milky Way (MW)

Chapter 1

Stellar Clusters and Black Holes

1.1 Background

Stellar clusters are self-gravitating systems of stars. They mainly form through the fragmentation of dense and cold molecular clouds. Generally, stars in clusters have similar internal properties, chemical compositions and are comparable in age. Depending on, e.g., the morphology, birth process, and the specific system's internal structure, we can characterise different clusters in various categories. These vary in sizes from a few pc in the smallest stellar associations to tens of pc in the largest. For instance, nuclear star clusters (NSCs) found at the centre of many galaxies can have densities up to $10^7 \text{ M}_\odot \text{ pc}^{-3}$ and contain up to billions of stars, while smaller clusters, such as open clusters only contain a few tens to thousands of stars.

Familiar constellations in the night sky discovered centuries ago are now confirmed to be various stellar clusters. The Pleiades and the brightest star in Taurus are examples of open clusters. These are collections of typically young stars located close to the disk inside our galaxy. The study of stellar clusters dates back to Messier (1784), where the famous astronomer Charles Messier released his catalogue of observed stellar components, including about 60 detected clusters (Karttunen et al. 2003).

Many rich stellar systems, such as GCs, are perfect laboratories for studying stellar dynamics and evolution. Investigating stellar clusters involves a sea of opportunities to explore the various physical phenomena of cluster evolution and the formation of observable exotic objects through gravitational dynamics. In this thesis, we will mainly focus on how the dynamical evolution of GCs and the retention of BHs in their cores correlate with observable structural parameters of the clusters.

1.2 Globular clusters

GCs are some of the oldest observed components in our Universe to date. They are spherically distributed in our galaxy (Fig. 1.1), with the oldest clusters in the Milky Way's halo. GCs contain up to $\sim 10^7$ stars and are usually 10 to 13 billion years old. These are characterized by a majority of low metallicity, population II stars, (but can vary between $[\text{Fe}/\text{H}] \approx -2.5$ dex to $[\text{Fe}/\text{H}] > 0.5$ dex, Kissler 2019a) in spherical distribution with central densities of $\approx 10^5 \text{ stars pc}^{-3}$, where most of the mass crowds the innermost few parsecs (Karttunen et al. 2003). Their densities are several orders of magnitude larger than the solar neighbourhood, which has a number density of $\approx 0.1 \text{ stars pc}^{-3}$. Dynamical interactions drive the evolution of the cluster, and its long term survival depends on its internal structure and how bound the stellar components are to the

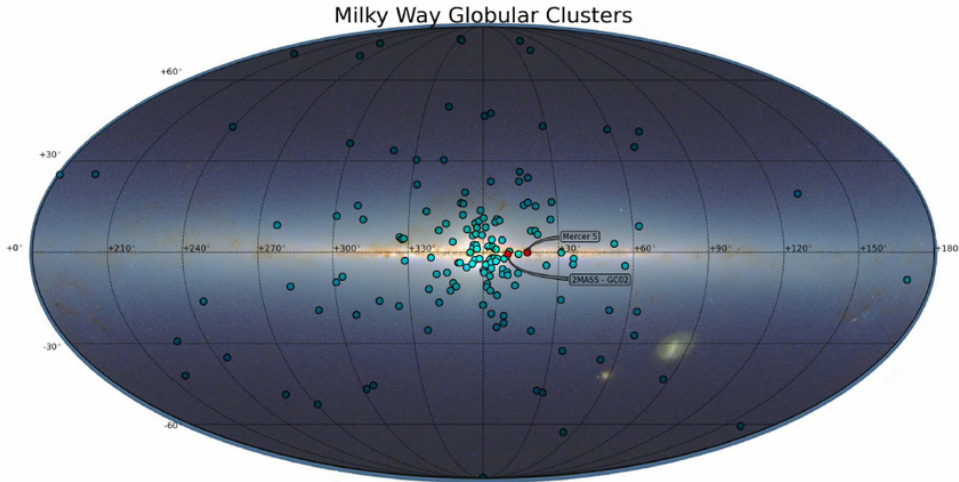


Figure 1.1: An illustration of the spatial distribution of GCs present in the Milky Way Galaxy (Fig. 1 in Peñaloza et al. 2015). To this date, between 150 - 200 GCs have been found in our Galaxy (Harris 1996; Chaisson et al. 2008; Baumgardt et al. 2020). The indicated clusters in red are Mercer 5 (rightmost dot) and 2MASS-GC02 (leftmost dot).

system. Almost all galaxies host a significant number of clusters and the specific frequency of GCs scales with the host galaxy mass (Harris et al. 2013).

GCs are collisional systems, and hence their dynamical evolution is dependent on two-body interactions and not only on the gravitational field. This means that the granularity of the gravitational field can change the overall cluster equilibrium on relaxation time scales (Mapelli 2017a). If a system is relaxed, stars in the system have undergone enough stellar encounters that the orbits of the stars significantly differ from the orbits they would have had in a smooth gravitational field. In other words, they have “forgotten” their initial states (Binney and Tremaine 2011).

A cluster’s relaxation timescale is related to its crossing timescale t_{cr} , which is the time for an object to cross a cluster radially without any encounters. We relate the crossing time to a characteristic cluster radius R and the velocity dispersion σ (e.g., Benacquista and Downing 2013) via

$$t_{\text{cr}} = \frac{R}{\sigma}. \quad (1.1)$$

This quantity relates to the relaxation time through



$$t_{\text{rlx}} \simeq \frac{0.1Nt_{\text{cr}}}{\ln(N)}, \quad (1.2)$$

where N denotes the number of objects in the cluster. GCs have typical half-mass relaxation times that range from 0.1 - 1 Gyr. Relaxation times in the core can be even shorter. A system is defined as collisional if the relaxation time scale is shorter than the age of the cluster τ . To describe the evolution of the cluster, we need to consider timescales longer than the relaxation timescales¹.

Structurally, GCs consist of a self-gravitating core and a sparse outer halo. Their stellar populations embody similar iron contents and are thus chemically homogeneous (with exceptions

¹Since for $\tau < t_{\text{rlx}}$, we have a collisionless system.

Table 1.1: A table that characterizes the demographics of open clusters and GCs. The crossing times and relaxation times are estimated via equations (1.1) and (1.2). Note that these values are estimates and can alter significantly since measurements of, e.g., the velocity dispersions or half-mass radii of clusters are often uncertain and vary between different clusters.

Properties	Open Cluster	Globular Clusters
		
Mass	100 - 1000 M_{\odot}	$10^4 - 10^6 M_{\odot}$
Radii	1 - few pc	10 - 30 pc
Central density	$\leq 10^3 M_{\odot} \text{pc}^{-3}$	$\geq 10^5 M_{\odot} \text{pc}^{-3}$
Age	1 Myr - few Gyr	$\geq 5 - 10$ Gyr
t_{cr}	$\sim 2 \times 10^6$ yr	$\sim 1.5 \times 10^5$ yr
t_{rlx}	$\sim 2 \times 10^7$ yr	$\sim 1.5 \times 10^9$ yr

described in Section. 2.1.1). The array of stars populates the complete range of stellar types, providing their characteristic Colour-Magnitude (CM) diagram (shown in Fig. 1.2).

The sizes and masses of GCs determine their characteristics. Their states are commonly defined by the following distance scales

$$\left\{ \begin{array}{ll} r_{\text{h,m}} & \text{Radius containing half the mass of the cluster} \\ r_{\text{t}} & \text{Radius where the host Galaxy's gravitational field dominates the cluster's field} \\ r_{\text{c}} & \text{Radius where the density is half of the central value.} \\ r_{\text{c,obs}} & \text{Radius at which the surface brightness is equal to half the central value} \\ r_{\text{hl}} & \text{Radius within which half of the total cluster luminosity is contained} \end{array} \right.$$

Here, $r_{\text{h,m}}$ denotes the half-mass radius, r_{t} the tidal radius, r_{c} the core radius, $r_{\text{c,obs}}$ the observational core radius and r_{hl} the observational half-light radius (Benacquista and Downing 2013). The initial evolution of the half-mass radius is connected with the stellar evolution of stars in the cluster. It expands as massive stars lose mass due to stellar evolution. As the system's total mass reduces, the central potential weakens, which leads to the expansion of the halo until the galaxy's tidal field restricts the size. Dynamical expansion is more efficient for clusters with short t_{rlx} (Gieles 2012). Similarly, the inner core radii usually expand over time through stellar evolution unless the cluster undergoes core collapse. Energy deposits further accelerate both expansion mechanisms from hard binaries in the core that transfer their kinetic energy to the lighter components, counteracting collapse (Section. 1.2.2). For comparison, the demographics of GCs, as opposed to open clusters, is provided in Table. 1.1.

1.2.1 Evolution and stability

The birth properties of GCs sets how they will subsequently evolve. As GCs have different relaxation times, it is possible to look at their evolution in different dynamical states. Their fundamental evolution initiates as interacting bodies exchange energy, which alters velocities locally. Stars might *evaporate* from the cluster if their velocities are higher than the escape velocity of the cluster. Typical values of cluster escape velocities are on the order of a few tens of km s^{-1} (Kissler 2019b). The limit by which stars escape is given by

$$\frac{1}{2}v_{\text{e}}^2 = |\phi|, \quad (1.3)$$

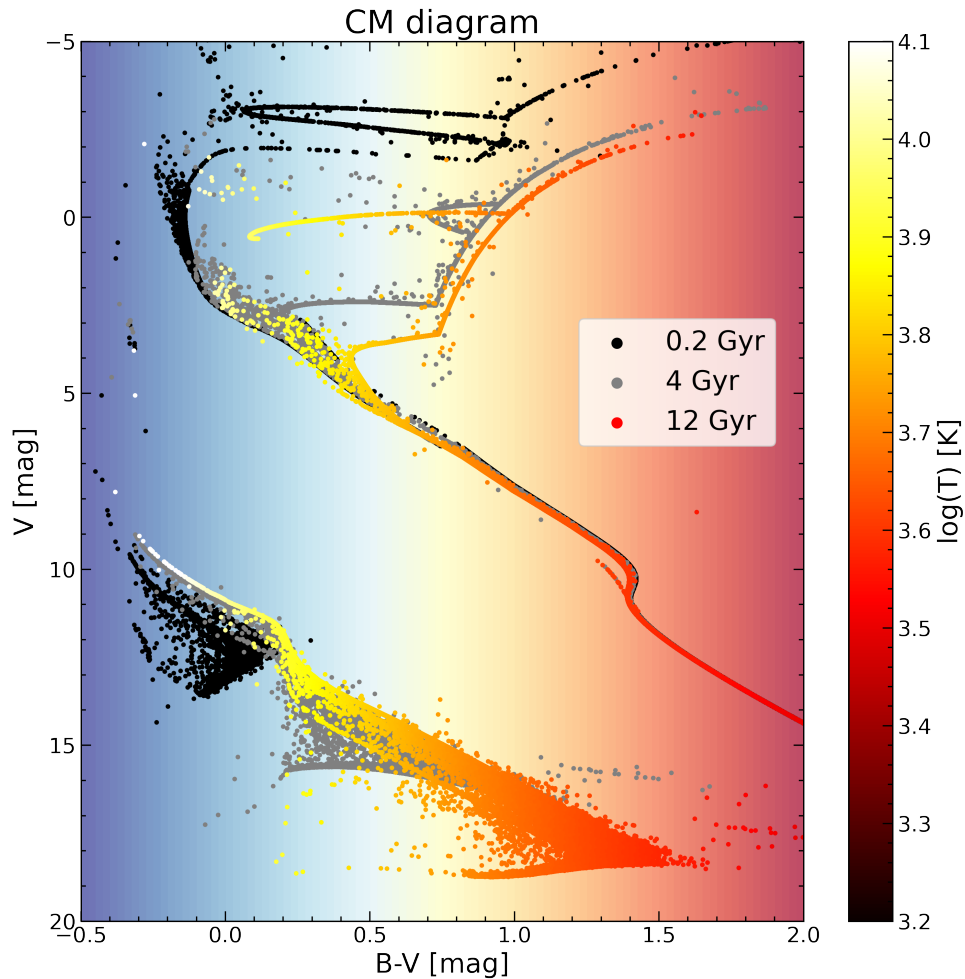


Figure 1.2: A colour-magnitude (CM) diagram of a typical cluster, constructed using snapshots from the MOCCA code. The figure illustrates stars (dots) at different stages of their evolution (similar metallicities) for three snapshot times: **0.2 Gyr** (denoted as black dots) represents the evolution early on with the characteristic turn-off at low magnitude values, portraying the cluster with very young stars; **4 Gyr** (grey dots), an intermediate stage in the cluster evolution; **12 Gyr**, indicated in colour-coded dots, with gradient representing the effective temperature of each star. The image’s background denotes the typical colour of stars at their position in the cluster. Worth noting is the comparison between the faintness of the WD (lower left dots in the figure) that becomes fainter and redder over time. The difference in the position of the MS turnoff between black and coloured dots represents the different turnoff age for each snapshot time.

where ϕ is the gravitational potential of the cluster, $\langle v_e \rangle^2 = 4\langle v_{\text{rms}} \rangle^2$ is the escape velocity and v_{rms} is the root-mean-square velocity (Mapelli 2017a).

Encounters between objects lead to gravitational deflections which drives the cluster to *relax* (see equation 1.2). Several scattering events accumulate and the cluster evolves towards *equipartition*, meaning that kinetic energy is shared equally between components (Davies 2013). Due to stellar evolution, the system loses mass through supernovae (SN) events or by stellar winds from massive stars. This expansion can help in delaying or halting core collapse (Section. 1.2.2). The rapid mass loss changes the cluster’s potential, and stars can go out of *virial equilibrium*. Consequentially, the kinetic energy of individual stars increases, boosting the evaporation rate,

meaning the total kinetic energy of the system decreases. The system expands as the potential becomes more shallow (Benacquista and Downing 2013). Two-body encounters between stars rapidly stabilize the system via *two-body relaxation*, where encounters between more massive components transfer energy to the lighter. Energy equipartition is a direct consequence of relaxation where energy should spread equally and is achieved when

$$m_i \langle v_i^2 \rangle = m_j \langle v_j^2 \rangle, \quad (1.4)$$

for two stars of dissimilar masses m_i and m_j and average velocities v_i and v_j (Mapelli 2017b).

1.2.2 Instability, core collapse and reversing core collapse

Fig. 1.3 illustrates the dynamical evolution and stability of a cluster. As two-body relaxation tries to equalize the kinetic energy in a cluster, massive stars typically transfer their energy to the lighter components in encounters, and consequentially sink to the centre. Their kinetic energy heats the lighter components into wider orbits at the cost of their own. This process is called *mass segregation* and occur on timescales $t_{\text{ms}} \sim (m_i/\langle m \rangle)t_{\text{rlx}}$, for the average stellar mass $\langle m \rangle$ and a certain stellar component mass m_i (Benacquista and Downing 2013). The rate of dynamical encounters increases in the core, and stars eject via close two- or three body interactions. Mass and kinetic energy is lost from the core, leading to a decrease in velocity dispersion and contraction. Similar to stars, GCs possess a negative heat capacity. As stars radiate energy, their core density increases and the rate of nuclear reaction increase. Equivalently, as GCs lose energy, their cores contract and becomes dynamically hotter (Mapelli 2017c).

The contraction again increases the kinetic energy in the core and also the rate of evaporation in the core. If the kinetic energy is not spread equally between the components in the cluster, massive stars continue to sink further and further into the centre. Continuous evaporation events increase the density of the core further, which drives the core to collapse (bottom right panel in Fig. 1.3). Such a process is defined as a *gravothermal instability* (Benacquista and Downing 2013). However, investigating both local and extragalactic clusters, there exist a variety of both collapsed and non-collapsed clusters, meaning there must be some process responsible for halting the collapse of the core.

The contracted core can lead to the dynamical formation of binaries (or primordial/initial binaries can have segregated here via dynamical friction from the abundant background lower mass stars). As multiple bodies interact dynamically, internal energy from the binary systems can be injected into stars and excite them to wider orbits, which increases their kinetic energy. As a result, the system expands, producing a shallower potential and fewer two-body interactions to drive the core towards collapse. Recall from Section. 1.2.1 that stellar feedback from SN or stellar winds results in mass loss leading to cluster expansion.

The injection of energy to the core typically occurs as intruder bodies increase their kinetic energy at the cost of the binary orbit, either through a *fly-by* interaction, where it steals the binary's internal energy and decreases its semi-major axis (hardening), or by *exchange*, where a heavy intruder can replace the lighter component inside the binary. Both cases inject energy into the cluster's core and halt the collapse. In contrast, the intruder can also transfer its kinetic energy to the binary, leading to binary softening and dissolution which can contribute towards core collapse (Davies 2013; Mapelli 2017b).

Dynamical interactions among retained BHs and BBHs can similarly sustain the core from collapsing. The injection of energy into the core from BHs is crucial in the long term survival of the cluster. We will now explain the formation of BHS and IMBHs in more detail and elucidate how they aid in counteracting core collapse.

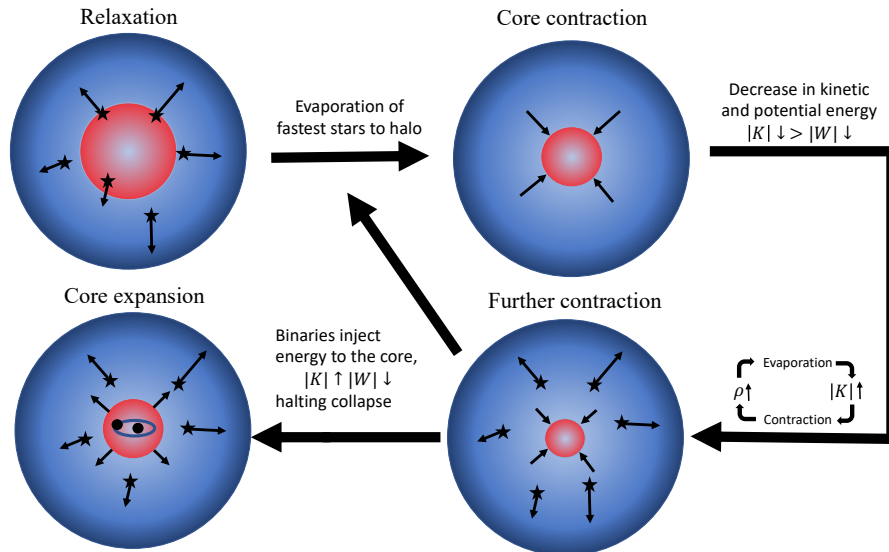


Figure 1.3: A schematic diagram displaying the processes that govern the core collapse and halting of core collapse in GCs. The figure illustrates the relaxation process (top left) where stars evaporate, resulting in core contraction (top right). The core can further contract (bottom right), which onsets core collapse by increased evaporation. However, the creation of BBH in the centre help energizing the core, which can halt the core from collapsing (bottom left).

1.2.3 Black Hole Subsystems and Intermediate-Mass Black Holes

1.2.3.1 Formation of stellar-mass black holes and a black hole subsystem

The formation and retention of BHs in GCs is still uncertain and depends on many different factors, such as the dynamical evolution of the cluster, the kick velocity BHs acquire when they form, and the initial mass function of the cluster. Already after a few to tens of Myr, a substantial number of BHs are likely to form from the evolution of massive stars ($\gtrsim 20 M_{\odot}$). Their retention is strongly governed by the natal kicks received from the progenitor supernova, which typically is set by the fallback mass onto the BH, asymmetry in its mass ejecta, and ejections in dynamical encounters (Kremer et al. 2019a). The natal kicks will either eject BHs if their kicks exceed the escape velocity of the cluster; otherwise, they will be retained (Askar et al. 2019a). BHs forming through direct collapse or having significant fallback accretion² might have reduced natal kicks (Belczynski et al. 2010). Contrarily, if BHs receive the same birth kick as neutron stars (NS) (typically $200 - 1000 \text{ km s}^{-1}$; Hobbs et al. 2005), very few BHs will be retained in the cluster following their formation.

Previous analytical studies theorized about few retained BHs in GCs (e.g., Kulkarni et al. 1993), where primordial BHs would quickly form a BHS at the cluster centre. Several dynamical encounters inside the BHS would result in rapid ejections of BHs, yielding short half-mass relaxation times and inducing core collapse. More recent theoretical and numerical studies have revealed prescriptions that dynamical processes in GCs can lead to the long-term retention of a substantial population of stellar-mass BHs (e.g., Breen and Heggie 2013; Morscher et al. 2015). X-ray and radio observations and radial velocity measurements have observationally identified several BH candidates in GCs (Strader et al. 2012; Bahramian et al. 2017; Giesers et al. 2018), while numerical simulations show up to 1000 retained BH candidates at Hubble time for large initial populations ($\approx 10^6$ stars, Askar et al. 2019a; Wang et al. 2016).

²A low-metallicity (compared to solar) environment increases the likelihood of a direct collapse because stellar winds are more quenched, leading to larger progenitor masses and stronger accretion onto the formed BH

In simulations, BHs settle to the centre of the cluster on a dynamical friction timescale $t_f \sim 0.1 t_{\text{rh,m}} \approx 10 - 100$ Myr, where $t_{\text{rh,m}}$ is the cluster’s half-mass relaxation time. If there is a substantial number of BHs in the segregation process, they can form a self-gravitating BHS in the centre (Kulkarni et al. 1993). The large number density of BHs in the system makes the core dynamically active, inducing the development of BBHs. Some of these BBHs might be ejected or disrupted through three-body processes (in a process defined as *binary burning*, see Sec. 1.2.4) or inject energy to the core at the cost of their orbits. Via the same arguments presented in Section. 1.2.2, the cluster will either evolve towards collapse or stabilize through three-body interactions, depending on the amount of energy injected into the core. The evolution of the BHS is strongly connected to the cluster’s overall relaxation time and hence, the dynamical interactions within the system (Breen and Hoggie 2013).

1.2.3.2 Intermediate-Mass Black Holes

IMBHs are BHs in the mass range of $10^2 - 10^5 M_\odot$. Before the first discovery of a 66 and 85 M_\odot BH merger by the LIGO/VIRGO/KAGRA collaboration in 2019 (Abbott et al. 2020), these objects were theorized and uncertain. Only stellar-mass BHs of masses, $M_{\text{BH}} \approx 5 - 30 M_\odot$ generated from core collapse of massive stars and, $M_{\text{BH}} \approx 10^6 - 10^9 M_\odot$ BHs, found in the centres of galaxies had been discovered (Miller and Colbert 2004). In simulated dense stellar environments, hard BBHs can, however, merge via the emission of gravitational waves (GW), generating a BH in the intermediate-mass range. Two main formation channels of IMBHs are now considered in more detail.

In clusters with dense cores, massive stars can accumulate mass at the cluster centre. Very massive stars can form through *runaway collisions of stars* (Portegies Zwart et al. 2004). In low metallicity environments, these stars could potentially directly collapse to form IMBHs (Mapelli 2016; Di Carlo et al. 2021). Additionally, mergers between stellar-mass BHs and massive stars could also result in the formation of an IMBH (Giersz et al. 2015).

Another formation channel is by *repeated merger events* of BHs (Miller and Hamilton 2002). As external stars make a fly-by close to a BBH, the binary can transfer energy to the single star and become harder (Section. 1.2.2). The binary can then coalesce via the emission of GWs. The remnant merger can now exchange into other binaries and repeat this process to accumulate mass, as long as the BHs are not ejected out of the cluster (Mapelli 2017c). This is one of the main formation channels for IMBHs inside MOCCA, and typically requires core densities of $\approx 10^6 - 10^7 M_\odot \text{pc}^{-3}$ and short relaxation timescales.

IMBHs have so far only been detected indirectly via the detection of radiated GWs (Abbott et al. 2020). Typically, the search for IMBHs in GCs comes from kinematic observations close to cluster centres or electromagnetic radiation from accretion onto the IMBHs. Common signatures are an increased velocity dispersion for stars in the vicinity of the IMBH and, therefore, large line-of-sight (LOS) velocities and mass to light ratios³. However, the presence of other bright and heavy objects makes these observations difficult and direct observational evidence is still limited (Askar et al. 2017).

1.2.3.3 Black Holes and Dynamical Age

The dynamics of BHs follow closely the theory presented in Section. 1.2.2, where dynamical interactions are dominant in dense clusters with short relaxation time scales. Multiple body processes are common in GCs and can dynamically produce or eject new bodies via binary-single interactions or binary-binary interactions (see, e.g., Hoggie 1975 for details). We refer to

³In some simulated models, the IMBH can make up for a significant fraction of cluster mass, up to ≈ 50 % (Askar et al. 2017)

a cluster as *dynamically old* if the cluster’s half-mass relaxation time is short. A dynamically old system has developed a dynamically hotter core in a shorter time scale than a cluster with longer relaxation time and thus has had more time for dynamical interactions to shape observable cluster properties. Conversely, *dynamically young* clusters are usually extended and less dense, favouring retention of a BHS. (Breen and Heggie 2013; Arca Sedda et al. 2018, see Fig. 3.2). In terms of how the distribution of stellar populations is affected by the cluster’s dynamical age, we expect, for instance, a larger segregation of more massive stellar populations in dynamically older systems and a higher probability for IMBHs to form. The shorter relaxation timescales in these dense cores increases the rate of interactions and the probability for runaway mergers.

Throughout this project, we will use the dynamical state of the cluster in context to its dynamical age. Sizes of BHSs are determined by the *influence radius* that describes the point in a cluster where half of the mass is represented by BHs, while the other half is in other stellar components. Dynamically old systems generally possess smaller influence radii since dynamical interactions have depleted most of their central BHs, minimizing heating and allowing components to distribute further into the core.

1.2.4 The role of BHS and IMBHs in clusters

We begin with emphasizing the role of binary burning and stellar-mass BHs in GCs. The onset of binary burning will generate energy, where BBHs can put single BHs on wider orbits and also deposit energy into the bulk of the GC. Their energy injection avoids cluster collapse (Chatterjee et al. 2013). More retained BHs induces a larger gap between the BHs at the centre and the lighter components, from the injection of energy by the central BBHs. This process is called *BH heating*. Massive stars are consequently more strongly influenced since they orbit closer to the central BHs (Kremer et al. 2019b). IMBHs form in GCs that are initially very dense and have a high velocity dispersion. Once an IMBH forms, it will quickly settle in the cluster’s centre, generating a deep potential that favours dynamical interaction of objects close to the centre. This implies a higher ejection rate of BBHs in the centre. Such cluster have shorter relaxation times and are dynamically older.

The lack of a substantial BHS in the core allows other heavy components to segregate closer to the cluster’s centre, typically increasing the central surface brightness. Contrarily, frequent dynamical interactions among stars and BHs in a cluster with a BHS will put brighter components on extended orbits. This causes global parameters such as the core radius, half-light radius and Lagrangian radius to increase. We indicate this significance in Fig. 1.4, which clearly displays an increased half-light radius in the top BHS model compared to the lower IMBH model. The initially denser core in the IMBH model forms a dynamically older system with brighter components on shallower orbits.

1.2.5 Aim and physical importance

The main aim of this project is to quantify the effects of observable stellar populations in simulated GCs in the presence of a BHS or an IMBH in the cluster’s centre. Clusters hosting a substantial BHS in the centre tend to have lower central surface brightness and extended half-light and core radii. Interactions between BHs and lighter stellar components result in the dynamical heating of stars (Arca Sedda et al. 2018), naturally exciting the lighter stars to wider orbits.

We investigate the influence of retained BHs on the segregation and distribution of particular observable stars, such as BSS, bright binary systems and giants. This involves analysing snapshots from hundreds of simulated GC models from the MOCCA code (Hypki and Giersz 2013) to find observable properties that can diagnose the observational state of the cluster and determine

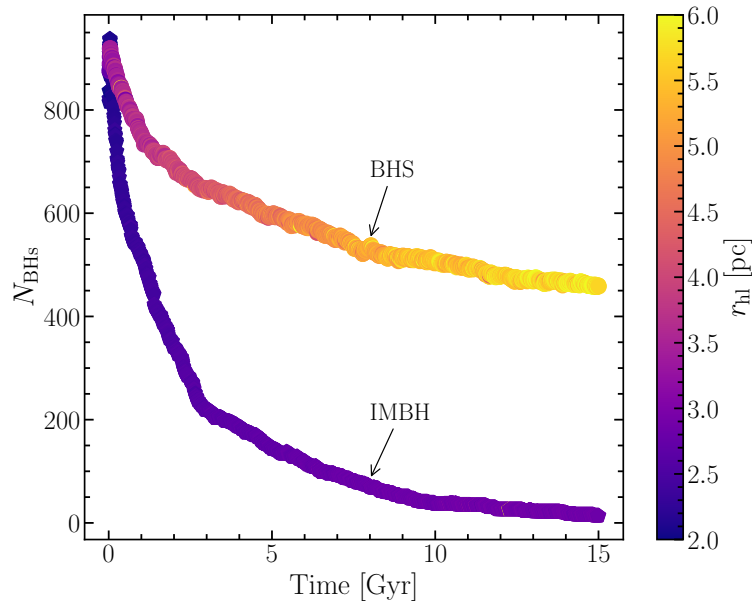


Figure 1.4: The depletion of BHs over time for two systems with similar initial parameters, but different half-mass radii ($r_{\text{hm}} = 4.0$ for BHS and $r_{\text{hm}} = 1.2$ for IMBH system), colour coded by the evolution of the half-light radius using results from the MOCCA code.

whether it hosts dark remnants. We quantify the effects of dynamics in the presence of an IMBH or a BHS by looking at the segregation of main-sequence stars, giants, binaries, stellar exotica and compact objects. For this purpose, we examine the relative cumulative radial distribution of these observable objects. Due to the strong gravitational potential of the IMBH, we expect more substantial segregation quantitatively in IMBH cluster models compared to models hosting a substantial BHS, with fewer stellar-mass BHs to counteract the segregation.

We additionally investigate separations in binary populations depending on the central dynamical state of the clusters and find connections between how core binary fractions, relaxation times, and mass segregation can help distinguish clusters harbouring few BHs or an IMBH. The goal is to use these quantities, together with the central surface brightness of clusters, to predict the numbers and masses of BHs and IMBHs in observed GCs and compare them with recently published results. Connecting the cluster dynamical state with the presence or absence of BHs and conjunct this further with binary fractions and GC properties can help give insights into the observable signatures of these crowded systems.

Chapter 2

Numerical Tools and Algorithms

In this chapter, we briefly introduce the background details of the MOCCA code, which was used to simulate the GC models analyzed in this thesis. In Section.2.1, we highlight new features in MSD II and explain how scripts are developed around these simulation outputs, together with some details about the previous MOCCA survey. The theory and methods are introduced in Section.2.2 with details about projecting simulated data in Section.2.2.1 and determining global properties in Section.2.2.2. A comparison between MSD II models and observed data is made in Section.2.2.3 and details about mass segregation for MS populations and stellar exotica are presented in sections 2.2.4 and 2.2.5. Binary properties are presented in Section.2.2.5.1. Finally, the methods for predicting the numbers and masses of BHs and IMBHs in observed GCs depending on their observed segregation can be seen in Section.2.2.6.

2.1 The MOCCA Code

The MOCCA¹ code developed by Hypki and Giersz (2013) is an improved package from previous Monte Carlo based cluster simulations (Giersz 1998; Giersz 2001; Giersz 2006; Giersz et al. 2008), to simulate the characteristics and evolution of real-sized star clusters. MOCCA takes into account all the important physical processes that drive the dynamical evolution of a cluster. It simulates the long term dynamical evolution of spherically symmetric clusters using the Monte Carlo method from Hénon (1971). It incorporates single and binary evolution of stars using an updated implementation of the prescriptions provided by the SSE and BSE population synthesis codes (Hurley et al. 2002). For computing the outcome of close binary-single and binary-binary encounters, MOCCA employs the direct N-body code for scattering experiments, called the *fewbody* code (Fregeau et al. 2004). The current MOCCA version does not have support for triples or higher hierarchical systems.

MOCCA evolves stellar clusters with various initial parameters (see Section.2.1.2.2) beyond the Hubble time, where the code outputs simulation snapshots at different times. These snapshots contain information about the position, velocity and stellar/binary evolution status of each object in the cluster. Monte Carlo methods allow for fast evolution of systems containing many bodies with high precision and detailed analysis for all of the clusters' components. The Monte Carlo method resolves cluster evolution on timescales that is a fraction of a cluster's relaxation time (c.f equation 1.2). A realistic stellar cluster can be evolved within a few CPU-days to weeks on a single-processor computer using MOCCA.

¹stands for MOnTe Carlo Cluster simulAtor

2.1.1 Test Survey 2 - Multiple populations

MSD II (Maliszewski et al. 2021) is a collection of over 250 numerical simulations with varying initial conditions and is a follow-up to the first survey, MOCCA-Survey Database I (hereafter, MSD I), in which nearly 2000 star cluster models were simulated (Askar et al. 2017). Compared to previous versions, the new survey is able to trace the dynamical evolution of multiple populations and, to some degree, their stellar evolution (Hypki et al. in prep.). For decades, it was thought that GCs contained simple co-eval populations of stars with similar composition. Recent discoveries have however shown that most of the GCs detected seem to include multiple stellar populations, such as a lower and upper main-sequence or sub-giant branches (Paust et al. 2010). The main purpose for incorporating this effect in MOCCA is to investigate the dynamical mixing between two populations systems with large central densities, up to, $\rho_c \sim 10^7 M_\odot \text{pc}^{-3}$ (Maliszewski et al. 2021).

The retention of BHs in the cluster is strongly dependent on the natal kicks that they receive at birth. If the natal kick velocity (expected to arise due to asymmetries in the supernova explosion (Janka 2013)) is larger than the escape velocity of the cluster, the BH will be ejected upon formation. In the MSD II models analyzed in this thesis, the natal kicks received by NS and BHs are drawn using a Maxwellian distribution with a velocity dispersion of $\sigma = 265 \text{ km s}^{-1}$. This distribution is derived from the observed proper motions of NS in our Galaxy (Hobbs et al. 2005). In the case of BHs, this kick is scaled according to the final BH mass using a momentum conserving formulation. Therefore, BH natal kicks are determined by their final mass. In MSD II models, the evolution of BH progenitors was carried out using metallicity dependent stellar wind prescriptions (Puls et al. 2008; Belczynski et al. 2010), and final BH masses are determined using the delayed SN prescriptions (Fryer et al. 2012). These prescriptions allow for the formation of BHs with masses of up to $45 M_\odot$ from stellar evolution. Therefore, a significant fraction of BHs with these masses receives natal kicks that are less than the escape speed of the cluster.

2.1.2 MOCCA-SURVEY Database I

Cluster models from MSD I have been used in determining various evolution aspects of GCs, from finding merger rates of BBH (Askar et al. 2017), accreting white dwarf binaries (Belloni et al. 2016) to investigating binary populations as a sign for IMBHs (Aros et al. 2021). Since the MSD II is not directly built to recreate the characteristics of real MW GCs², we incorporate data from MSD I when doing direct comparisons with observed data. Similar procedures as for MSD II can be made for the first survey, using similar methods. The MSD I data has over 2000 simulated GCs spanning a wider range of initial parameters where the present-day properties of these models agree well with most of the observed GCs in our Galaxy (Askar et al. 2017). MSD I also contains models where the BHs get similar kick to NS (Hobbs et al. 2005) and the retention fraction of BHs in these models can be as low as 1%. The maximum mass of a BH produced through stellar evolution in MSD I models is about $30 M_\odot$.

In terms of initial conditions, there is a wider range of initial number of objects, varying King model parameter (single population) of $W_0 = 3.0, 6.0, 9.0$ (Peterson and King 1975), varying metallicities, initial binary fractions and choice of natal kicks. A summary of the initial conditions of MSD I models can be found in Table. 1 in Askar et al. (2017).

²although it is able to reasonably reproduce some of their observed properties

Table 2.1: A table indicating the different types of stellar populations that is distinguishable in the MOCCA code. For further details about the definitions and acronyms, see Hurley et al. (2002).

Main-Sequence	Hertzsprung gap	Giants	Core He burning	Stripped stars	White Dwarfs	Compact objects
0 = $M \leq 0.7 M_{\odot}$	2 = HG	3 = FGB	4 = CHeB	7 = HeMS	10 = HeWD	13 = NS
1 = $M \geq 0.7 M_{\odot}$		5 = EAGB		8 = HeHG	11 = CoWD	14 = BH
		6 = TPAGB		9 = HeGB	12 = ONeWD	15 = MR

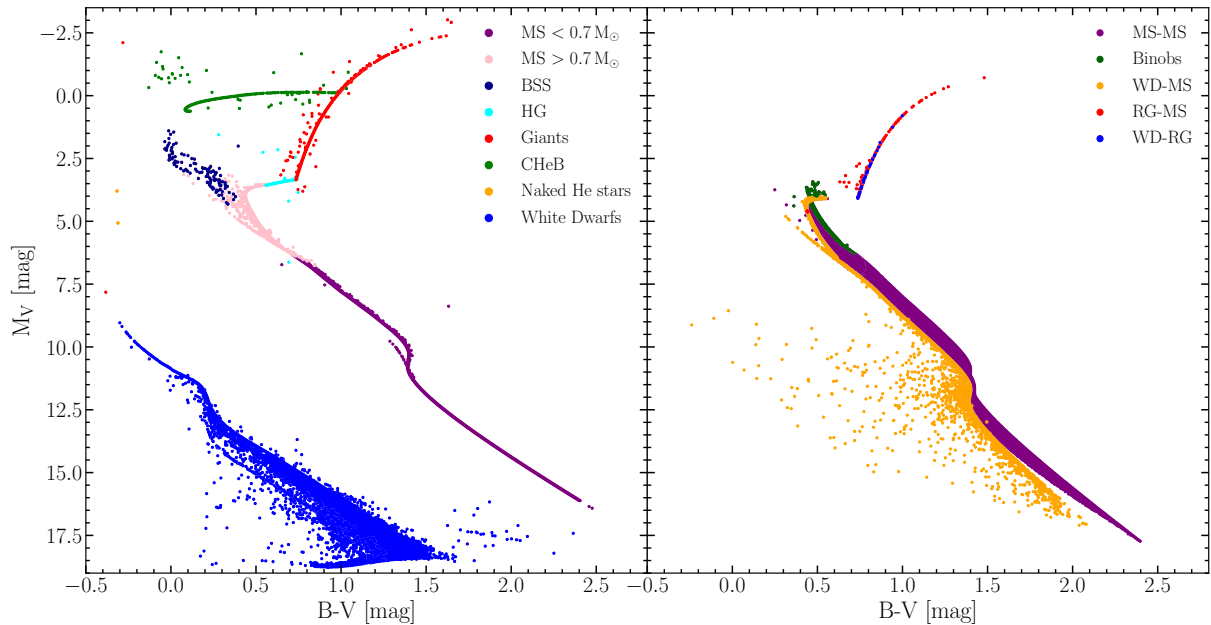


Figure 2.1: Colour-magnitude diagrams for single stellar populations in the left panel and binary populations on the right, plotted from a 12 Gyr snapshot using the MOCCA code. Compact objects, such as NS and BHs have been discarded in the figure due to their faint magnitudes. The “Binobs” are bright MS binaries with individual binary masses above $0.5 M_{\odot}$ while also their mass ratio, $M_2/M_1 > 0.5$, for binary component masses $M_{1,2}$ where $M_2 > M_1$. Each stellar population can further be subdivided according to Table 2.1.

2.1.2.1 Stellar types

In Fig. 2.1, a CM-diagram is produced from the output of a 12 Gyr snapshot, using the MSD II. The figure shows a schematic of the various stellar types available in the code, where the different types are indicated in different colours. These types are divided further into subcategories according to a typical stellar scheme, where the stellar populations are determined in branches of main-sequence stars, giants, horizontal branch, stripped stars, white dwarfs and compact objects. From these, we can also define the BSS. These are bluer and brighter than a typical main-sequence star at the MS turnoff and commonly formed in MS mass accretion events or collisions (Leigh et al. 2007). A detailed description of every stellar type is given in e.g., Hurley et al. (2002), with a summary provided in Table 2.1.

2.1.2.2 Initial parameters

The MSD II allow us to evolve over 250 GCs with various initial parameters. These include variations in the initial binary fractions, number of objects, initial tidal radius among others. A description of the initial parameters can be seen in Table 2.2. The initial conditions are generated from the `Mcluster` code (Kamlah et al. 2021) with options to vary e.g., the specific

Table 2.2: Initial parameters for cluster evolution in the MSD II models. The majority of models have initial binary fractions $f_b = 0.95$, while some include $f_b = 0, 0.1, 0.12, 0.146, 0.63$. N stands for the number of objects, however, the number of stars varies depending on the binary fraction considered; $N_{\text{tot}} = 2f_b N + N(1 - f_b)$. The IMF is two-segmented and given by Kroupa (2001). The eccentricity distribution for models where $f_b \neq 0.95$ is thermal and the semi-major axis distribution is uniform in $\log(a)$, in the interval $2(R_1 + R_2)$ and 100 AU. Otherwise, the majority of models follows binary properties of (Kroupa 1995). In each of the clusters, the metallicity is $Z = 0.05 Z_\odot$, W_0 is the King (1966) model concentration parameter. The `mup` parameter determines the upper limit of the mass function and is set to either 50 or $150 M_\odot$ with the lower mass limit as $0.08 M_\odot$. The concentration parameter `conc_pop` describes the half-mass radius fraction, $r_{\text{h,mcl},2}/r_{\text{h,mcl},1}$, between a population i and the first population. The two values in the columns for `conc_pop`, N , `mup` and `W0` relate to the properties of the first and second population of stars in the initial model.

Initial choice of parameters in MSD II					
N	W0	mup	rbar	rh_mcl	conc_pop
$2 \times 10^5, 4 \times 10^5$	6.0, 8.0	150.0, 50.0	60, 120	0.6, 1.2, 2.0, 4.0, 6.0	0.1, 0.2, 0.5, 1.0, 1.5
$4 \times 10^5, 4 \times 10^5$	6.0, 8.0	150.0, 50.0	60, 120	0.6, 1.2, 2.0, 4.0, 6.0	0.1, 0.5, 1.0, 1.5
$4 \times 10^5, 6 \times 10^5$	6.0, 8.0	150.0, 50.0	60, 120	0.6, 1.2, 2.0, 4.0, 6.0	0.1, 0.2, 0.5, 1.0, 1.5

initial conditions for two populations individually. The numbers `N`, concentration parameter `W0` and mass limits `mup` can be separately determined for the populations. Some models exclude stellar evolution and are flagged as such (see Section. 2.1.3). Integration timesteps are calculated based on the first 50 Myr mass loss and semi-major axes are defined up to 100 AU initially, with a lower boundary condition that restrict immediate mergers at start of the simulation. The `conc_pop` parameter, which sets the initial concentration of the two populations is easiest understood by noting that a value of 0.5 means that the second population (generation) stars is twice as densely concentrated compared to the first. Parameters such as the `rbar` (tidal radius) and `rh_mcl` (initial half-mass radius) determine the initial structure of the cluster.

2.1.3 Problematic models

MSD II is an updated test survey for the development of the MOCCA code (Hypki et al. in prep.). Maliszewski et al. (2021) investigated the IMBH escape rate among the various models included in the survey. They found that in a fraction of these clusters, there were escaping or “disappearing” IMBHs with typically large masses. Additionally, there were cases of *illegal mergers*, where binaries were allowed to merge and grow to form IMBH, despite their semi-major axes being $> 10^3 R_\odot$. Such binaries would not merge within the Hubble time. We choose to avoid these models in most of the analysis conducted in this thesis, but indicate the places where they are included.

Models with escaping IMBHs can alter the evolution of the mass segregation in our MSD II models since their disappearance could alter the potential of the cluster and also the ejection and disruption rates of binaries. However, since in most of the models in MSD II, the IMBH masses are not dominant in terms of the total cluster mass (median IMBH- to cluster mass ratio is $\approx 0.18\%$), this change is taken as negligible in cases where the problematic models are included. Most illegal mergers and escaping IMBHs have been found to occur in the first few hundred of Myrs in the cluster evolution and thus, we do not expect the present day properties to be strongly affected by these effects in the problematic models. This is because the clusters have had sufficient time to adjust to these changes. Updated versions of the MOCCA code have identified and removed these issues and a subset of these new models have been included in our simulations. Note that MSD I does not contain these problematic models.

2.2 Data extraction and methods

Each evolved GC available in the MSD II (and, to some extent, from MSD I) is used for our analysis. For every simulation output, we extract snapshots of, e.g., radial positions, kinematics, and brightness profiles of individual components at fixed points in time. We analyse the properties of various stellar populations in snapshots of either 100 Myr, 1 Gyr, 10 Gyr or 12 Gyr. To extract the data for the results, we write scripts in `awk` and pipe these through Python's `subprocess` package. A typical output file consists of ≈ 280 lines (each standing for an individual cluster), with a certain number of columns for each desired quantity extracted.

2.2.1 The COCOA code - cluster projections

In this thesis, we make use of the recently developed `COCOA`³ code that provides mock observations from simulated snapshots as input (Askar et al. 2018c). This is used when calculating half-light radii, central densities and central surface brightness in our models. We use the radial positions in our simulations and run it through `COCOA` to find the projections of stars' positions onto the sky. The radial positions of stars are projected from spherical to Cartesian coordinates according to

$$r_{\text{px}} = r \sin \theta \cos \phi, \quad r_{\text{py}} = r \sin \theta \sin \phi, \quad r_{\text{pz}} = r \cos \theta, \quad (2.1)$$

where r is the position vector of a star, θ is the polar angle and ϕ is the azimuth angle. These angles are randomly generated in the intervals, $\phi \in [0, 2\pi]$ and $\cos \theta \in [-1, 1]$. The projected cluster-centric distances are extracted simply via $r_{\text{xy}} = \sqrt{r_{\text{px}}^2 + r_{\text{py}}^2}$.

2.2.1.1 V-band luminosities and magnitudes

For a proper treatment of binary systems, we need to find their combined magnitudes and luminosities. The simulation snapshots contain individual V, B and U band magnitudes for each star. For all binaries in the snapshot, we computed their combined magnitude in the V band using

$$M_{\text{tot}} = -2.5 \log_{10} (10^{-0.4M_1} + 10^{-0.4M_2}), \quad (2.2)$$

where M_{tot} is the combined absolute V-band magnitude of a binary system and M_1 and M_2 are the individual absolute magnitudes of each binary component respectively. A similar procedure is made for the B and U band magnitudes. Furthermore, knowing the absolute magnitudes of each object, we can calculate their V-band luminosities in solar units using the following equation

$$L_{\text{v}} = 2.5119 \cdot 10^{4.83 - M_{\text{tot}}} \quad (2.3)$$

and put as a separate column inside the snapshot file. The relation between the absolute magnitude and solar luminosity is given by

$$M = 4.83 - 2.5 \log_{10}(L_{\odot}), \quad (2.4)$$

where 4.83 is the absolute V-band magnitude of the sun and L_{\odot} is the solar luminosity.

³Stands for Cluster simulatiOn Comparison with ObservAtions

Table 2.3: A table showing properties for four models which we analyse in detail in the results section. The four models have initial parameters; $n = 400\,000$, $200\,000$, $w_0 = 6.0$, 6.0 , $\mu_{\text{up}} = 150.0$, 150.0 , $r_{\text{bar}} = 60.0$, $\text{conc_pop} = 0.1$, except for the $r_{\text{hm,init}} = 0.6$ model which has $\text{conc_pop} = 0.5$. The values are extracted from 12 Gyr snapshot models. Note that $M_{\text{BH,max}}$ stands for the most massive BH (either single or in a binary) at 12 Gyr and $t_{\text{hm,rlx}}$ is the 12 Gyr half-mass relaxation time, calculated based on Spitzer (1987) as $t_{\text{hm,rlx}} = 0.138(\sqrt{M_c}r_{\text{hl}}^{3/2})/(\langle m \rangle\sqrt{G}\ln(\Lambda))$, for the cluster mass M_c , coulomb logarithm Λ and gravitational constant G .

Four distinct clusters						
$r_{\text{hm,init}}$ [pc]	N_{BHs}	$M_{\text{BH,max}}$ [M_{\odot}]	r_{hl} [pc]	$r_{\text{c,obs}}$ [pc]	$t_{\text{hm,rlx}}$ [Gyr]	Central property
0.6	24	692	1.67	0.85	1.7	IMBH
1.2	27	5142	2.83	0.95	3.2	IMBH
4.0	489	58	5.67	3.45	5.6	BHS
6.0	388	64	5.68	4.0	4.8	BHS

Table 2.4: Two special cases of clusters, having initial half-mass radii of 1.2 and 4.0 pc respectively, with initial conditions set to form a substantial BHS and an IMBH. For the $r_{\text{hm,init}} = 1.2$ model, the initial conditions are set to $n = 400\,000$, $600\,000$, $w_0 = 9.0$, 9.0 , $\mu_{\text{up}} = 150.0$, 150.0 , $r_{\text{bar}} = 120.0$, $\text{conc_pop} = 0.1$ and the $r_{\text{hm,init}} = 4.0$ model to $n = 400\,000$, $600\,000$, $w_0 = 6.0$, 6.0 , $\mu_{\text{up}} = 150.0$, 150.0 , $r_{\text{bar}} = 120.0$, $\text{conc_pop} = 0.1$.

Two special cases						
$r_{\text{hm,init}}$ [pc]	N_{BHs}	$M_{\text{BH,max}}$ [M_{\odot}]	r_{hl} [pc]	$r_{\text{c,obs}}$ [pc]	$t_{\text{hm,rlx}}$ [Gyr]	Central property
1.2	37	4500	5.03	0.95	5.0	IMBH
4.0	779	38	12.8	5.6	11.5	BHS

2.2.1.2 Half-light radius, central densities and central surface brightness

The half-light radii in clusters, r_{hl} , are determined based on the cluster-centric radius, r_{xy} , and the combined luminosity, L_{v} , seen in equations (2.1) and (2.3). To calculate this quantity, the stellar luminosities are sorted in increasing radii and cumulatively added up to the radii where $L_{\text{cumulative}} = L_{\text{v,tot}}/2$, thus where the cumulative sum of luminosities is equal to half of the clusters' total. The position where this is satisfied is set as our projected half-light radius.

Central densities are calculated by summing up the masses of stars (excluding BHs) inside a radial limit, $r_{\text{lim}} = 0.2$ pc, and determined as, $\rho_{\text{c}} = M_{\text{tot}}/r_{\text{lim}}^3$, in units of $M_{\odot} \text{pc}^{-3}$. If the radial limit is chosen to be too small, the presence of an IMBH can significantly increase the central density value. Here M_{tot} is the sum of masses for single and binary stars. Similarly, the central surface brightness is extracted by summing up the combined luminosities inside a radial limit of $r_{\text{lim}} = 0.02$ pc and calculated as, $\Sigma_{\text{c}} = L_{\text{v,tot}}/r_{\text{lim}}^2$, in units of $L_{\odot} \text{pc}^{-2}$. The limit was used because the observed data for central surface brightness has typical spatial resolution of around 1 arcseconds and distances to most of the clusters range between four and ten kpc (Harris 2010). This corresponds to ~ 0.02 to 0.04 pc distance from the centre of the cluster. Using this limit yields comparable values with the observed data (see Fig. 3.21).

2.2.2 Initial setup - global properties

We extract distinctive global properties for four clusters to determine differences in observable parameters depending on the number of retained BHs in the centre of clusters and if the cluster model either harbour an IMBH or a central BHS. In three of these cases, we vary only the initial half-mass radius and, in one case, also the concentration parameter. We present their 12 Gyr properties in Table. 2.3. Two additional clusters are presented in Table. 2.4 which are designed to retain a large BHS and a massive IMBH whilst also having a large sample of initial objects.

From the snapshots, the initial half-mass radius ($r_{\text{hm,init}}$), number of BHs (N_{BHs}), mass of the most massive BH ($M_{\text{BH,max}}$), half-light radius (r_{hl}) and core radius (r_{c}) are extracted. These six clusters work as a basis for the global analysis of our results. Note that the number of BHs, N_{BHs} , includes singles, BBH and BHs in binary systems.

We subsequently observe how the dynamical state of a cluster influence global properties over time by extracting data from the available `system.dat` file inside the MSD II. This file contains information on how spatial, dynamical and global quantities of cluster models evolve up to the Hubble time. The Lagrangian radii are determined as a function of time, for two clusters harbouring a substantial BHS of 591 BHs, while the other contains an IMBH with only 9 BHs present. The Lagrangian radii are extracted directly from the simulation outputs, but can equally be produced from finding the position of which a certain amount of mass is enclosed in a cluster, using the snapshots. The two clusters have similar initial half-mass radii of $r_{\text{hm,initial}} = 0.6 \text{ pc}$ and are analysed as a function of time to see the difference in cluster expansions. We additionally extract the clusters' core radii and number of retained BHs as a function of time for the models presented in Table. 2.3 (similar to Fig. 2 in Kremer et al. 2019b). These results are presented in Figs. 3.1 and 3.2.

2.2.2.1 Cluster snapshots

Cluster morphologies are analysed by extracting the central surface brightness profiles available in the `profile.dat` file inside the MSD II as a function of radius for the two clusters in Table. 2.3 that retains only 26 BHs with a $5142 M_{\odot}$ IMBH and the other model which retains 489 BHs. Similarly, x and y positions are projected using COCOA from the snapshots, and central densities are calculated as described in Section. 2.2.1.2.

The half-light and core radius follow the distribution of bright stars in the cluster. The influence radius probes the size of the central BHs, and the 50 % binary radii is a proper indication of the dynamical heating of BHs since their distribution will change under their influence. The influence radius is calculated with two methods, depending on whether the cluster hosts an IMBH or not. For a BHS model (or for models with few BHs and no IMBH), this radius is calculated by cumulatively summing the mass of the BHs until half of the cluster mass is in BHs and the other half is in stars. For IMBHs, the influence radius is the point in a cluster enclosing the radius of 2 IMBH masses. Thus, according to Sedda et al. (2019), $M_{\text{GC}}(r_{\text{inf}}) = 2M_{\text{IMBH}}$, where M_{GC} and M_{IMBH} is the cluster and IMBH mass respectively and r_{inf} is the IMBH influence radius. The 50 % binary radius is calculated simply as the radius containing 50 % of binaries.

Cluster morphologies with projected positions are shown in Fig. 3.3 in addition to a zoom-in inside the half-light radius of these two clusters in Fig. 3.4.

2.2.3 Comparison with observed data

New and improved observations over the Milky Way (MW) GCs have given new insight about their spatial and kinematic properties (Harris 1996, Harris 2010, Baumgardt et al. 2020). By utilising the available snapshots from the MSD II, we perform cross-correlations over a few

quantities (Section. 2.2.1.2) and compare them with observed data. We transform the observed core- and half-light radius in Harris (2010) from arcseconds to pc, and extract the same data from Baumgardt et al. (2020). Their data is overplotted over the half-light radius of each model in the MSD II simulations as a function of observational core radius. Similarly, central surface brightnesses are extracted from the catalogues, plotted against the observational core radius, and compared with the same quantities from MSD II at 12 Gyr. In the Harris (2010) data, this quantity is given in V-magnitudes per squared arcseconds. Apparent magnitude are transformed to absolute V-magnitudes using the distance modulus, $M = m_v - 5 \log_{10}(R_{\odot}) + 5$, where m_v is the V-band apparent magnitude in mags/arcseconds and R_{\odot} is the distance from the Sun in pc. We convert this to central luminosity, L_c , via $\Sigma_c = 2.51186^{4.83-M}$. Finally, to find units of $L_{\odot} \text{pc}^{-2}$, we utilize that, $\Sigma_c = L_c(180 \times 3600/\pi/R_{\odot})^2$. Similarly, we find the central surface brightness in Baumgardt et al. (2020) via $\Sigma_c = 10^{\sigma_c}/(M/L)$, where σ_c is the mass surface density in units $M_{\odot} \text{pc}^{-2}$. The correlation between observed and simulated quantities is presented in Section. 3.2.

2.2.4 Mass segregation

To investigate the dynamical effects on GCs depending on their central properties, we examine the mass segregation of stellar populations in the absence or presence of an IMBH or a substantial BHS. We begin our analysis by considering three populations of main sequence stars, similar to Weatherford et al. (2020), with positions in a CM-diagram displayed in Fig. 2.2. The populations are determined as fractions of the turn-off luminosity of the specific cluster considered. This quantification is favoured over considering average masses since stellar luminosities is what is actually measured observationally in clusters. Furthermore, these populations are typically well defined in observed HR-diagrams and are substantial in numbers to reduce statistical inconsistencies (Weatherford et al. 2020).

We investigate the influence of the presence of compact objects in the centre of the cluster on the distribution of different stellar objects by finding the cumulative number of objects inside a cluster as a function of their 2D cluster-centric radii, r_{xy} . The stellar populations considered in more detail consist of main-sequence stars, giants, white dwarfs, NSs, BHs and bright MS-MS binaries, a few magnitudes below turn-off. Recall that the latter is defined as binaries where the fraction of the binary components' masses are larger than 0.5 while also one of the components' mass must be larger than $0.5 M_{\odot}$.

For a consequential analysis, we consider the clusters in Table. 2.4. To observe the evaporation of BHs over time, we indicate the 50 % number line of BHs while also indicating the half-light and core radius. The cumulative distributions are taken at 100 Myr, 1 Gyr and 10 Gyr snapshots. A comparison can be made to the almost analogous Fig. 4 in Kremer et al. (2020), with our result presented in Fig. 3.7.

2.2.4.1 Quantifying mass segregation - A^+ and Δ_{r50}

We compare three MS populations of various luminosity ranges - and hence average masses - populating 1/125, 1/25 and 1/5 times the turn-off luminosity, L_{TO} . For the cluster models, we compare their normalized radial cumulative distributions between the three populations. The resulting CDFs of the populations are determined as a function of the logarithmic cluster-centric radii, $\log_{10}(r_{xy}/r_{hl})$, of each star, normalized to the half-light radius. In accordance to Alessandrini et al. (2016), we use the A^+ parameter to determine the segregation between two populations in the cluster, but instead normalized to the half-light radius of clusters. We define this quantity as the difference in area between the two populations' radial distributions, $\phi(r)$, and the logarithm of the normalized cluster-centric radius r_{xy} in the $\phi(r) - \log_{10}(r_{xy}/r_{hl})$ plane

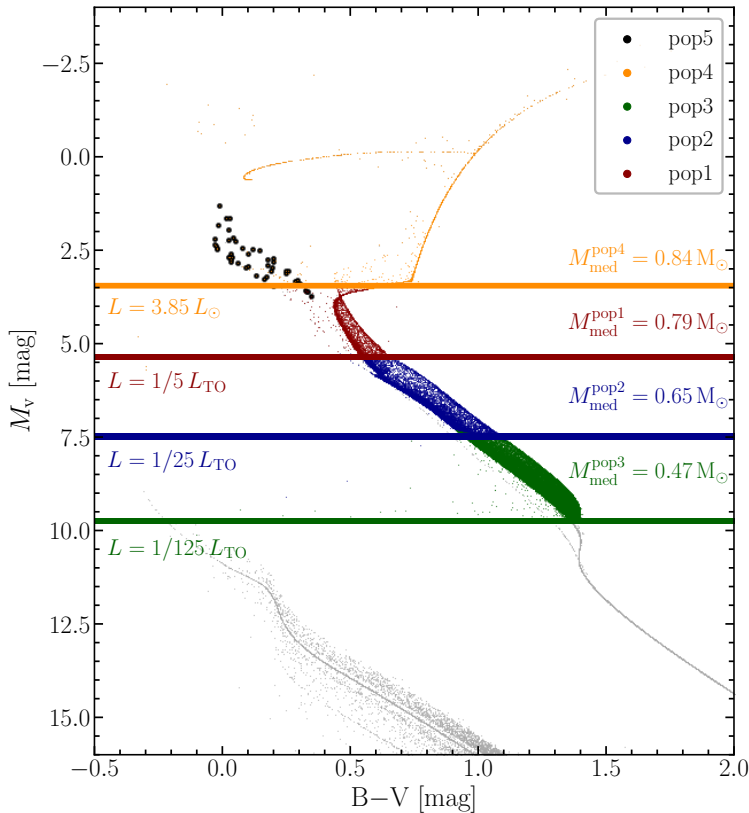


Figure 2.2: Colour-magnitude diagram outlining three various MS-populations as fractions of the turn-off luminosity of a cluster. The median masses are indicated for each populations. For the binaries, we assign the combined magnitudes using equation (2.2).

(see Fig. 2.3). We write this according to Weatherford et al. (2018) as

$$A_{ij}^+ = \int_{r_{\min}}^{r_{\max}} \left[\phi_j \left(\frac{r}{r_{\text{hl}}} \right) - \phi_i \left(\frac{r}{r_{\text{hl}}} \right) \right] \frac{dr}{r_{\text{hl}}} = \frac{A_j - A_i}{r_{\text{hl}}}. \quad (2.5)$$

Here, i and j denotes two stellar populations, where the average mass of j is larger than i and $r_{\min, \max}$ is the minimum and maximum radii of choice. The three populations initially considered are illustrated in the CM-diagram in Fig. 2.2, called **pop1** for the heaviest, **pop2** for the middle and **pop3** for the lightest MS population. The two heavier populations consist of giants as **pop4** and BSS as **pop5**.

The radial limits for mass segregation is based on the same limits as in Weatherford et al. (2020), where $r_{\text{lim}} = [0.52, 3.48] \times r_{\text{hl}}$ for the observed clusters. The limits are set by the field of view (FOV) available for the clusters in the ACS-Survey (Sarajedini et al. 2007). Segregation data is available for observed stars in the lower limit, $r_{\text{lim}}/r_{\text{hl}} = 0.52$. Since we predict data based on the available segregation limits, only stars within this radius are considered when quantifying segregation, thus, where $r_{\max}/r_{\text{hl}} < 0.52$. Note that when using this definition, A^+ becomes dimensionless.

Similarly, we adopt an additional definition to quantify the effect of mass segregation. We consider the difference between the median values of the populations CDFs called the Δ_{r50} parameter (see Fig. 2.3). The quantity is determined through

$$\Delta_{r50}^{ij} = \frac{r_{50,i} - r_{50,j}}{r_{\text{hl}}}. \quad (2.6)$$

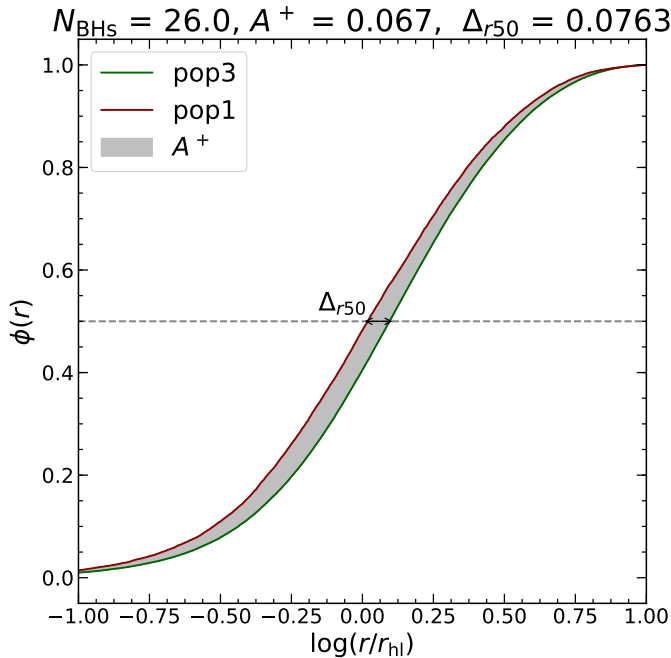


Figure 2.3: The segregation between the heavy and light MS populations defined in Fig. 2.2. The Δ_{r50} parameter is indicated as the difference in median values between the two populations as stated in equation (2.6). We also indicate the A^+ parameter in shaded grey, denoting the difference in area between the two populations. $\phi(r)$ denotes the normalized cumulative frequency of objects.

We denote the populations considered by a subscript of their population name. Hence, a subscript 12 would be measuring the mass segregation between populations **pop1** (turnoff MS stars) and **pop2** (MS stars with median masses of $M = 0.65 M_{\odot}$) as defined in Fig. 2.3. An illustration of these parameters is provided in Fig. 2.3, where the shaded grey area indicates the A^+ parameter and Δ_{r50} is the difference in $\log(r/r_{hl})$ at the 50 per cent value. These two parameters are additionally quantified for giants and BSS and compared to the lightest reference MS population.

The segregation data from the MSD II is compared to observed data (Sarajedini et al. 2007), which is available in Table. 1 for the Δ_{r50}^{13} parameter, and Table. A1 for the A_{31}^+ parameter in Weatherford et al. (2020). We perform a similar analysis as to Weatherford et al. (2020) by computing the number fraction of BHs to the total number of stars in our simulated clusters as a function of the segregation parameters. BHs are calculated as the total number of BHs, including both singles and binaries. The relation between the number fraction of BHs in our simulated clusters and the segregation parameters is fitted through a power-law in the log-log plane on the form; $\log_{10}(N_{\text{BHs}}/N_{\text{cluster}}) = \alpha \log_{10}(S) + \beta$, where S is either A_{31}^+ or Δ_{r50}^{13} , N_{BHs} is the number of BHs and N_{cluster} is the total number of stars in the cluster. The calculated relations are indicated in equations (3.1) and (3.2).

Our predicted number fractions are compared to the ones derived by Weatherford et al. (2020), where their BH fraction predictions are based on simulated results from the CMC Cluster Catalogue (Kremer et al. 2020). A summary over their initial parameters and models is in detailed explained in Section. 2 of Weatherford et al. (2020), which can be compared to our simulated models (Section. 2.1). Note that their runs are restricted to clusters with lower concentration ($W_0 = 5$) and lower initial binary fractions $f_b = 0.05$. Similar to our models, BH natal kicks are based on Belczynski et al. (2002) and Fryer et al. (2012) prescriptions. A comparison between the number fractions of BHs as a function of the A_{31}^+ and Δ_{r50}^{31} parameter, with models from

MSD II can be seen in Fig. 3.8.

We additionally extract the central surface brightness and half-mass relaxation times in Harris (2010) and Baumgardt et al. (2020) and plot these against the A^+ parameter for the populations $i = 3$ and $j = 1$ in equation (2.5), using both MSD I and MSD II models. These parameters are favoured over the number fractions of BHs since we do not rely on simulated models but rather on observed quantities. Additionally, the models are filtered depending on their central state (whether they contain an IMBH or a BHS) and compared with the observed data. The details are presented in Fig. 3.9.

2.2.5 Segregation in stellar exotica

The segregation is also determined for some stellar exotica including BSS, BBHs and NS-MS binaries. BSS are extracted by considering MS stars (`index = 1` in Table. 2.1) with masses up to 2% above the MS turnoff mass. Their cumulative radial distributions are investigated in snapshots of 0.1, 1 and 10 Gyr for the two clusters in Table. 2.4.

Through the simulation outputs, their formation paths are extracted by finding the number of dynamically formed BSS in collisions, single-binary or binary-binary interactions, which is available in the `system.dat` file. Their half-mass relaxation times at 10 Gyr are extracted to connect their formation rates to the clusters' dynamical ages. As for the MS populations, their central surface brightness are analysed as a function of the A_{53}^+ parameter, but now for each available model in the MSD I. Segregation and brightness differences between clusters are distinguished by filtering the clusters depending on their central BH properties. The details and results for these analyses are presented in Section. 3.3.1.

To find any sign of unimodality or bimodality in BSS populations, we apply the definition from Hypki and Giersz (2017). This is defined as the count of BSS and HB stars in logarithmic radial bins of the cluster, thus

$$R_{\text{BSS}}(r_{\text{xy}}) = \frac{N_{\text{BSS}}(r_{\text{xy}})/N_{\text{BSS,tot}}}{N_{\text{HB}}(r_{\text{xy}})/N_{\text{HB,tot}}}, \quad (2.7)$$

where $N_{\text{BSS}}(r_{\text{xy}})$ and $N_{\text{BSS,tot}}$ is the number of BSS in each radial bin and the total number of BSS in all bins respectively. Similar definitions stands for the horizontal branch stars. The bins are fine-tuned in order to find any signs of bi- or unimodality and is investigated for each cluster in Tables. 2.3 and 2.4. More details concerning these distributions can be found in Section. 3.3.1 and two examples are shown in Fig. 3.13.

Finally, to signify segregation differences between more combinations of populations, we perform a Kernel Density Estimation of their distributions. This procedure is available through the `sns` package in python and fits several Gaussians to the generated PDF of the various A^+ distributions. The models are split into BHS and IMBH models and we perform this exercise for each model in the MSD II, as well as the MSD I models. The distributions are presented in Figs. 3.14 and 3.15.

2.2.5.1 Binary distributions

The interaction rates among binaries seem to be directly governed by the dynamical age of a cluster. Recently, Aros et al. (2021) investigated the binary fractions inside clusters harbouring IMBHs and BHS, using results from the MSD I, with initial binary fractions filtered to $f_b = 0.1$. We perform a similar analysis on the MSD I and MSD II, filtered to initial binary fractions of $f_b = 0.1$ and $f_b = 0.95$ respectively. The binary fractions are extracted inside the core radius and plotted against the binary fraction between one and two half-light radii for the models at 12 Gyr, to compare how a varying initial binary fraction alters the binary fraction distributions

of evolved clusters. Subsequently, the clusters are divided into concentric bins between 0.05 to $2r_{\text{hl}}$ in each cluster, and the median value in each bin is extracted. Each model is filtered to whether they harbour a BHS or an IMBH, and a power-law is fitted through the median values.

For the clusters presented in Table. 2.4, the semi-major axis distributions of binaries are obtained from the simulated snapshots and compared between the models as probability density functions. The comparisons and figures concerning binary properties are presented in Section. 3.4.

2.2.5.2 Potential X-ray sources

Binaries can either be dynamically or primordially formed. MOCCA can trace any dynamical interactions in binary systems as the cluster evolves. Mass transferring events between two stars can generate enough X-rays to be observationally significant. We investigate the distribution of mass transferring white-dwarf main-sequence (WD-MS) binaries by calculating their Lagrangian radii. We also find different cluster models' percentages of dynamically, as opposed to, primordially formed WD-MS binaries. Lagrangian radii are extracted by cumulatively adding the mass of stars up to the point where it represents 10, 50, 70 and 98 % of the cluster's mass. Their distributions are compared to the radial distributions of main-sequence turnoff stars (MS_{TO}), with masses of 95 - 105 % to that of the clusters' turnoff mass at 12 Gyr. The comparison can be seen in Fig. 3.20.

2.2.6 Prediction of BHS numbers and IMBH masses

The relation between the number of BHs retained and their segregation parameters are extracted using power-law fits. Taking all the models that were analyzed from MSD I and MSD II, a power-law is fitted to the number of BHs and the masses of BHs for IMBH models as a function of A_{31}^+ . The fitting is performed by utilizing `numpy`'s `polyfit` package onto the log-log plane of these parameters, with the power-law equation on the form αx^β . This results in a linear fit; $\log_{10}(X) = \alpha \log_{10}(A_{31}^+) + \beta$, where X is either the number of BHs or the maximum BH mass for the cluster measured. Uncertainties for these relations are determined by the covariance matrix of the fit, using `polyfit`'s least square method. For the 50 available segregation parameters in Weatherford et al. (2020), the relations are used to predict the number of BHs and IMBH masses inside observed GCs in the MW, by applying the derived relations to observed segregation data. IMBH masses are only predicted for clusters that are more segregated than $A_{31}^+ \gtrsim 0.05$ while the numbers of BHs are predicted for all observed clusters. The upper and lower limits of uncertainty are given by the fitting error, $\sqrt{\text{diag}(\mathbf{E})}$, where \mathbf{E} is the covariance matrix generated from the least-square method package, together with uncertainties in the observed A^+ values. To reduce scatter around the plot and infer its uncertainty, a running mean through the numbers and masses of BHs and IMBHs is performed by binning them in A_{31}^+ . The variance in each bin is added towards the uncertainty for the final prediction. The predictions are presented in Section. 3.5.

Chapter 3

Results

The following chapter presents the main results of the thesis and some discussion around them. In Section. 3.1, we start by discussing the morphology and global properties of evolved cluster models. Subsequently, MSD II data is compared with observed cluster properties in Section. 3.2 before delving into the effect of mass segregation for various clusters in Section. 3.3. After that, we shed light on binary properties inside the clusters in Section. 3.4. Finally, the chapter is concluded by predicting the numbers and masses of BHs and IMBHs in observed GCs, based on their amount of segregation (Section. 3.5).

3.1 Global Properties

Our analysis begins by comparing two clusters, one cluster harbouring a substantial BHS and another hosting an IMBH. The two systems begin with similar initial parameters, having 6×10^5 objects, half-mass radii of 0.6 pc, masses of $3.2 \times 10^5 M_\odot$ and $3.5 \times 10^5 M_\odot$ for the IMBH and BHS model respectively, with initial central densities of, $\approx 6 \times 10^6 M_\odot \text{pc}^{-3}$. The BHS model has a larger initial tidal radius of 120 pc, while the IMBH model has $r_t = 60$ pc. We expect the dynamical heating of BHs in the BHS model to put lighter stars on wider orbits and extend the cluster's half-light radius and reduce its central surface brightness. Contrarily, the shorter relaxation time in the IMBH model and the lack of heating from BHs in its centre allow heavier components to sink closer to the cluster's core which increases the central surface brightness.

The Lagrangian radii of these clusters are depicted as a function of time in Fig. 3.1. The quantity indicates the position in which a certain percentage of the cluster mass is contained. The figure illustrates that the two clusters' mass loss, mainly through stellar evolution, yields expansion over time. However, the distribution of mass in the BHS model is evidently extended compared to the IMBH model (meaning, if we take a constant mass value for both clusters, the Lagrangian radius is larger for this given value), mainly due to two-body relaxation processes and the dynamical heating by the BHS. We find that in some initially sparse clusters (typically with $r_{\text{hm,initial}} > 4.0$ pc and low tidal radius $r_t < 120$ pc), clusters can dissolve if there is a substantial number of BHs retained in the core (Giersz et al. 2019).

Fig. 3.2 displays the four various clusters in Table. 2.3, which vary in initial half-mass radii. The initial half-mass radius probes how initially tidally filling- or underfilling a cluster is, and as introduced in Section. 1.2.2, the core radius is strongly dependent on BH burning processes, and hence, the number of retained BHs in the cluster. The extended models ($r_{\text{h,m}} > 1.2$ pc) both include a substantial BHS while the denser clusters contain IMBHs. The top panel in Fig. 3.2 indicates a clear difference in observational core radius between the models. In the dense models,

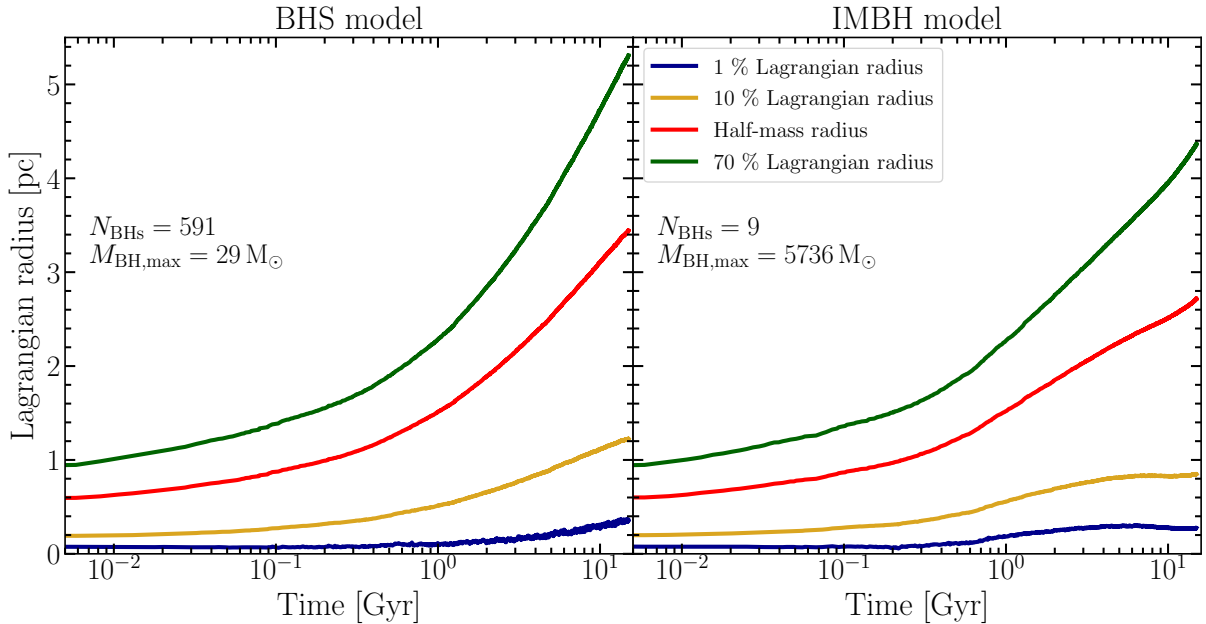


Figure 3.1: Comparison between two clusters simulated using the MOCCA code with evolving Lagrangian radii over time. This describes the radius in a cluster at which a certain mass percentage is enclosed. The number of BHs, N_{BHs} and maximum BH mass, $M_{\text{BH,max}}$ is given for the clusters at 12 Gyr.

the fewer stellar-mass BHs will reduce the effect of heating, allowing for other stellar components to sink further into the core, which reduces the overall core radius. Evidently, the BHS models retain the expansion of the core radius over time due to continuous BH heating, while the IMBH models converge towards lower values early on.

Clusters that are initially centrally dense are likely to form an IMBH. Dynamical interactions are more frequent in such clusters and many stellar-mass BHs can get ejected from the system due to two/three body encounters. These encounters can also result in BHs merging with the IMBH. The short relaxation times of these systems make the core dynamically older, meaning a more dynamically active core and a longer time for BH evaporation. This is reflected in the bottom panel of Fig. 3.2, showing the retention of BHs over time, where models with smaller core radii, and thus denser cores, retain fewer BHs. In the presence of a BHS, the longer relaxation timescales favour the long-term retention of BHs. We conclude that the initial half-mass radius correlates strongly with the rate BHs evaporate, thus, how quick BHs deplete over a certain time period (Breen and Heggie 2013). Faster depletion is seen for clusters with short relaxation times and denser cores (green and red lines in the bottom panel of Fig. 3.2).

From the four models in Fig. 3.2, we consider two cases. The simulated cluster with initial $r_{\text{hm}} = 1.2$ only retains 27 BHs, including BBHs, while the $r_{\text{hm}} = 4.0$ system retains 489 BHs at 12 Gyr. The IMBH model hosts a central BH with mass $M_{\text{BH,max}} \approx 5140 M_{\odot}$, part of a binary system, while the most massive BH in the BHS model is of $\approx 58 M_{\odot}$. In Fig. 3.3, the xy -projected positions of objects at 12 Gyr for the two cluster models is displayed. The top panels in the figure indicates the surface brightness as a function of the projected 2D radius. Four interesting radii are displayed to indicate the effect of dynamical heating of BHs; the half-light-, influence- and core radii are shown as projected circles in green, yellow and pink, respectively. The orange circle shows the position in the cluster containing 50 per cent of bright MS-MS binaries that are favourable in observations, $f_{\text{rb},50}$ (c.f Section. 1.2.3.3). Recall that this is not all binaries, but rather only the ones a few magnitudes below the turnoff in the CM diagram.

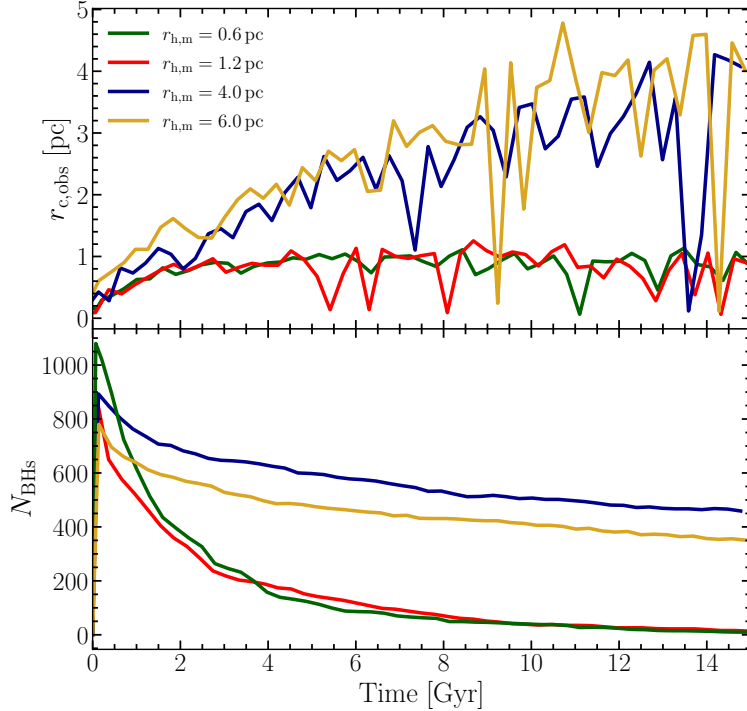


Figure 3.2: The evolution of the core radius of the four clusters presented in Table 2.3. These clusters start with similar initial parameters except for half-mass radius which is varied. Since the observational core radius depends on the central surface brightness, the presence of bright giants close to the centre can cause these values to fluctuate. The bottom panel relates this to the number of BHs retained in the cluster over time. Note that the slope of lines in the bottom panel indicates the rate at which BHs deplete in the various clusters.

The two models show apparent differences. We expect the dynamical heating in the BHS model to make the cluster morphology more sparse. Oppositely, a large central IMBH would allow brighter components closer to the core, increasing the central surface brightness. Each radius is extended in the BHS model due to the BH heating. Despite the many BHs crowding the innermost parts, the influence radius is also extended since the other components’ orbits that make up for the mass in the clusters are wider. The more BHs in the subsystem, the larger the influence radius and the BHS size. Additionally, the bright binaries and other bright stars in the IMBH model that crowd the cluster’s core decrease the influence radius and increase the central density and surface brightness values. Here, these values reach, $\rho_c \approx 10^4 M_\odot \text{pc}^{-3}$ and $\Sigma_c \approx 9 \times 10^5 L_\odot \text{pc}^{-2}$ respectively. We hence see an increase in the surface brightness close to the core, compared to the BHS model, which possesses $\rho_c \approx 10^3 M_\odot \text{pc}^{-3}$ with $\Sigma \approx 4 \times 10^5 L_\odot \text{pc}^{-2}$.

Figure 3.4 is a zoom-in inside the half-light radius of the clusters, also stating the number of bright MS-MS binaries and the number of BHs present inside the half-light radius. Despite seeing more retained luminous binaries inside the half-light radius for the IMBH model, the binary fraction is smaller ($f_b = 0.015$ for the IMBH model and $f_b = 0.02$ for the BHS). The dense cluster is dynamically older which increases the rate of ejected, disrupted and merged binaries over time. Contrarily, the presence of many BHs can lead to substantial heating of luminous binaries, which can cause them to eject or break up. In this case, however, the denser model is dominant in decreasing the binary fraction in the core.

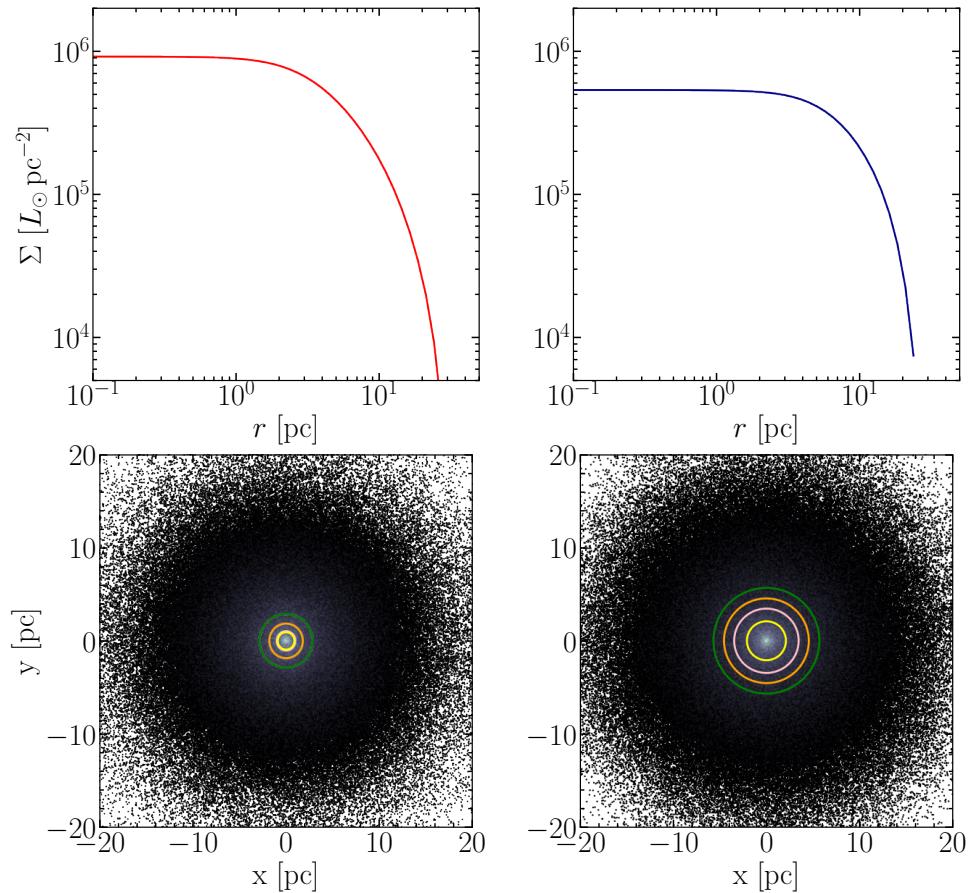


Figure 3.3: The surface brightness as a function of radius for an IMBH model (top left) and a BHS model (top right) at 12 Gyr snapshots. Bottom panels show xy -projections of objects. We indicate the half-light, core, influence and 50 % binary radius in green, pink, yellow and orange circles, respectively.

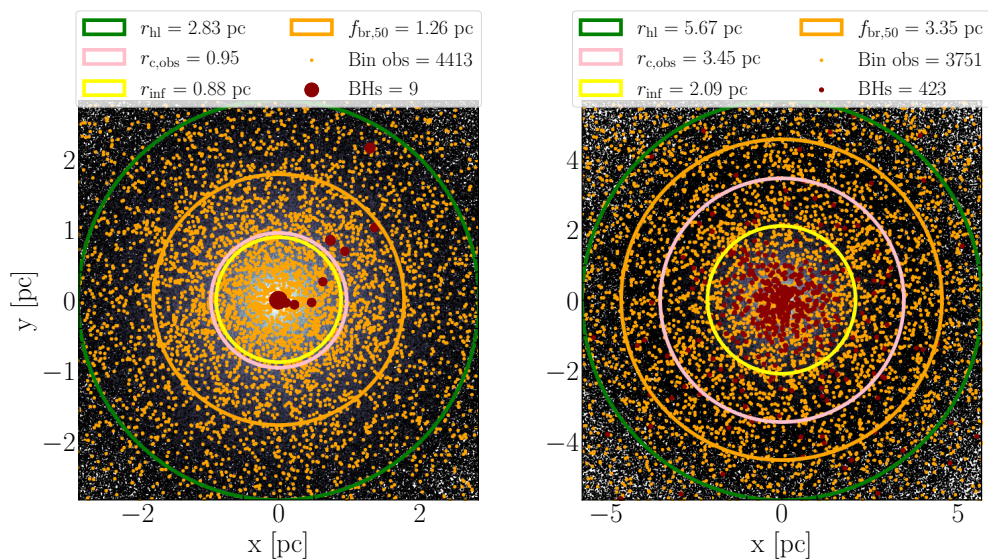


Figure 3.4: A zoom-in inside the half-light radius of the two clusters in Fig. 3.3, showing BHs as red dots and bright binaries in orange dots. The legend indicates their numbers inside the cluster’s half-light radius. The left panel shows the retention of an IMBH of $5140 M_{\odot}$ (denoted by the larger red dot in the centre), while the right column indicates a BHS system with 489 BHs. Note that the half-light radii of the two models are different and hence the axis limits of the plots have been adjusted accordingly.

3.2 Observational Signatures

To qualitatively analyse observational signatures in the simulated cluster models, we compare some global parameters in our models with observed GCs in the MW, using catalogued data from Harris (2010) and Baumgardt et al. (2020). Fig. 3.5 demonstrates the difference in half-light radius as a function of core radius for the simulated clusters in MSD II compared to observed values. The third dimension, indicated as the colour gradient, displays the number of retained BHs in MSD II models in logarithmic units. A linear fit through the data shows the relation between the half-light and core radius to be $r_{\text{hl}} \approx 1.3r_{\text{c,obs}} + 0.9$, where models retaining fewer BHs have generally smaller core and half-light radii. It is noteworthy to point out that observational core radii obtained from Harris (2010) are not taken directly from the core, but derived from a region around it, causing these values to generally be a bit extended. Additionally, Baumgardt et al. (2020) values are not purely observational, but derived from a suite of N -body models, which can cause slight biases in the scattered data.

Note the difference in the observed as opposed to the simulated clusters. The r_{hl} are collectively smaller compared to observed data, and only a few of the simulated clusters are fully representative of an observed cluster, in particular, for the IMBH models. Thus, the results derived from these models should be applied with caution when comparing to observed clusters. Tighter relations are, however, found when comparing other properties. Fig. 3.6 shows the central surface brightness at 12 Gyr as a function the clusters' core radii. By overplotting data from Harris (2010) and Baumgardt et al. (2020), we see an overlap between the observed data and our simulated clusters, with marginally larger values in general for the simulated clusters. As expected, the central surface brightness is a decreasing function of increasing number of BHs, where typically sparse clusters with longer relaxation times retain more BHs. For further references, we direct the reader to Appendix A, where we compare the total mass, escape velocities and core-to half light radii fractions of clusters.

3.3 Mass Segregation

We correlate the effect of mass segregation on various populations by directly observing how the cumulative number of certain stellar populations distribute as a function of their 2D projected radius. The stellar populations are chosen following Kremer et al. (2020) and also include bright MS-MS binaries (denoted Obs binaries in the figure). In Fig. 3.7 we illustrate this by showing the two clusters, with initial parameters presented in Table. 2.4, for three different timestamps; 0.1, 1 and 10 Gyr snapshots. Two vertical lines showing the observational core radius (in dashed green) and observational half-light radius (in dashed grey) have also been indicated. The horizontal purple dotted line indicates the 50 per cent number of BHs in the figure. Note that the easiest way to analyse this figure is by observing the panels that are in columns; this shows the clusters at the same timestamps, but with varying initial half-mass radius. Hence, from the top down, we go from a dynamically older to a dynamically younger system. Observing the image from left to right instead indicates the initial concentration of the populations at that specific timestamp. Note, however, that in each of the snapshots, the turnoff mass changes and hence, only images investigated column-wise indicates the same stellar populations.

At the 100 Myr time stamp, the initially denser model with lower half-mass relaxation time have heavier populations, such as the WDs and NS, distributed closer to the core. This trend continues in each of the timestamps considered. In the IMBH models, we generally see more segregation in each population (except for the BHs themselves), mainly due to the minor heating from the few BHs present in the core and the deep potential that the IMBH generates. The lack of BHs mainly arises from dynamical interactions in the dense, dynamically active core and

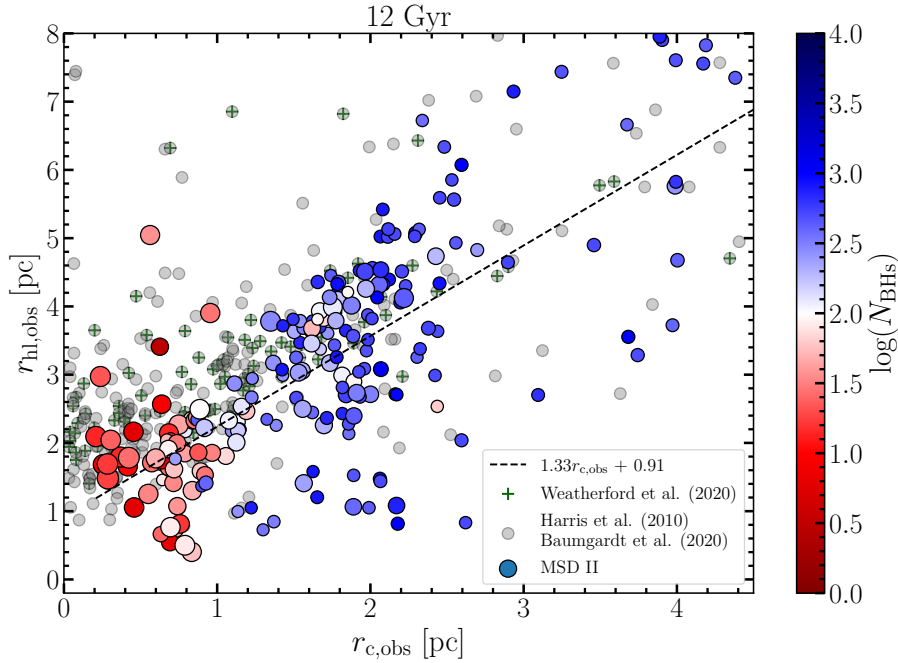


Figure 3.5: The observational half-light radii as a function of the observational core radii for simulated clusters (coloured circles), and values obtained for Galactic GCs from Harris (2010) and Baumgardt et al. (2020) (grey and crossed circles). The colourmap states the logarithm of the number of BHs retained in the cluster at 12 Gyr, and the size of the MOCCA points shows the mass of the most massive BH. Green crosses indicate the clusters with available segregation parameters (Weatherford et al. 2020), which are the clusters used in subsequent sections. Note that the core radius from Baumgardt et al. (2020) is not purely observational but rather derived from their suite of N -body models. The models are matched with the observed surface brightness and velocity dispersion profiles of GCs to estimate, e.g., masses, core radius and other properties.

mergers with the central IMBH. The retention of many BHs in the models generally increases the core and half-light radius. We clearly see increased half-light and core radii in the BHS models compared to the IMBH models, which is expected from BH heating. This is in accordance with Fig. 3.3.

Before quantifying the effect of mass segregation between various stellar populations, we make a comparison between the Δ_{r50} and A_{31}^+ parameter. Fig. 3.8 shows the number of BHs relative to the number of objects retained inside the clusters in the MSD II, as a function of the two segregation parameters defined in equations (2.5) and (2.6). We indicate the central dynamical state for each cluster; dark blue triangles indicate points where $N_{\text{BHs}} > 50$ and $M_{\text{BH,max}} < 100 M_{\odot}$; green squares where $N_{\text{BHs}} > 50$ and $M_{\text{BH,max}} > 100 M_{\odot}$; orange hexagons where $N_{\text{BHs}} < 50$ and $M_{\text{BH,max}} < 100 M_{\odot}$; and red circles where $N_{\text{BHs}} < 50$ and $M_{\text{BH,max}} > 100 M_{\odot}$. A power-law is fitted onto the logarithmic axes and is thus of the form $\log_{10}\left(\frac{N_{\text{BHs}}}{N_{\text{cluster}}}\right) = \alpha \log_{10}(S) + \beta$, where $S = A_{31}^+$ or $S = \Delta_{r50}^{13}$ respectively for the left and right panel and N_{cluster} denotes the number of stars in the cluster. Indicated is also data taken from Weatherford et al. (2020) in black diamonds showing their simulated number of BHs as a fraction of the total number of objects in their simulations on the vertical axis, and the A_{31}^+ parameter on the horizontal axis. This is compared to the same quantities in MSD II. Note that the models used to compute BH fractions have different initial parameters in MSD II and Weatherford et al. (2020) as explained in Section 2.2.4.1. The errors for the catalogue values are scaled to the logarithmic axes using $\text{err} = 0.1 \log_{10}(\sigma/S)$, where σ is the measured uncertainties.

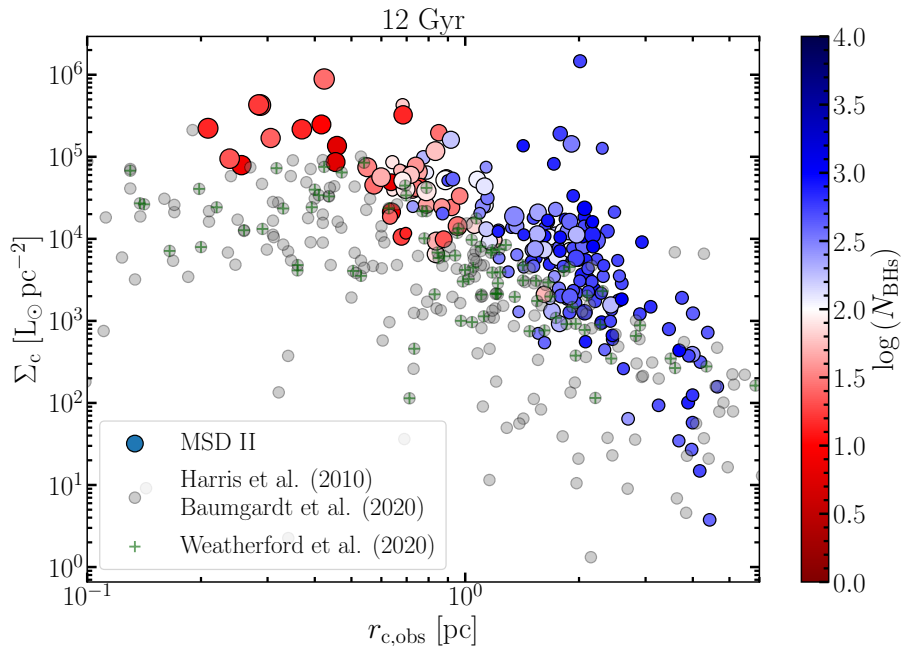


Figure 3.6: Analogous to Fig. 3.5 but showing the central surface brightness of each cluster as a function of the observational core radius.

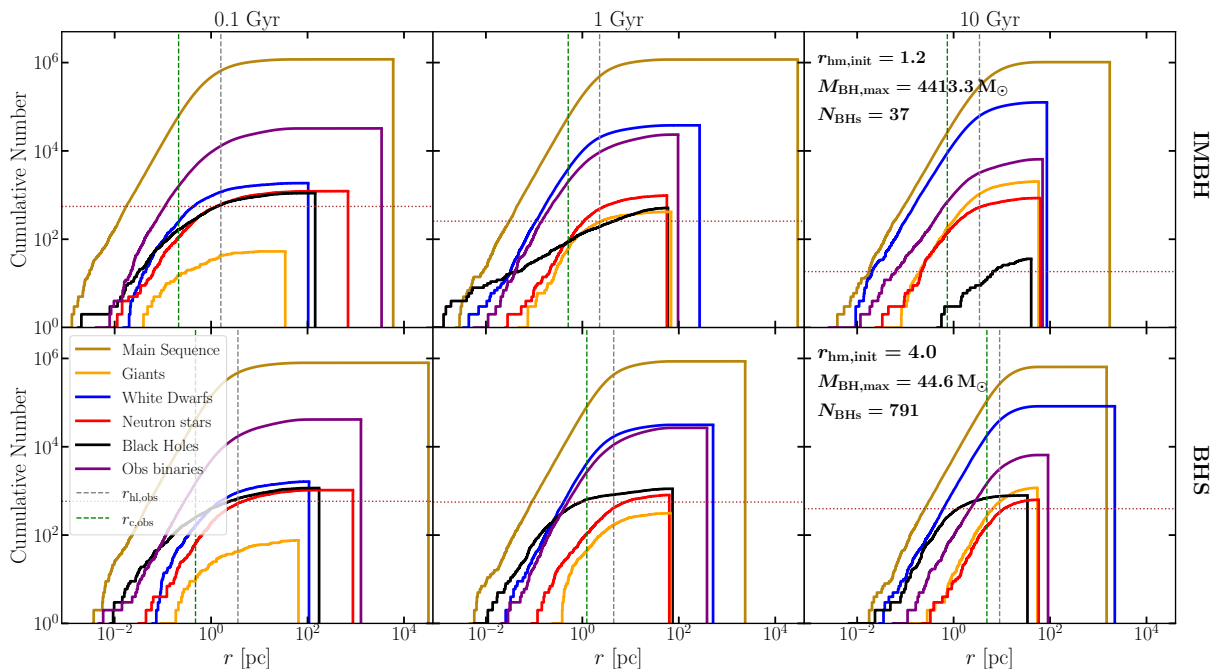


Figure 3.7: Cumulative number of various stellar objects as a function of their projected cluster-centric position in the cluster for the models in Table 2.4. Denoted as vertical lines are the half-light radius in dashed grey and the observational core radius in dashed dark green. A horizontal purple dotted line, denoting the 50 per cent of the value of number of BHs is provided, to signify how the number of BHs deplete over the clusters' evolution, starting from 0.1 Gyr on the left hand panels; 1 Gyr in the middle and 10 Gyr on the right hand side panels.

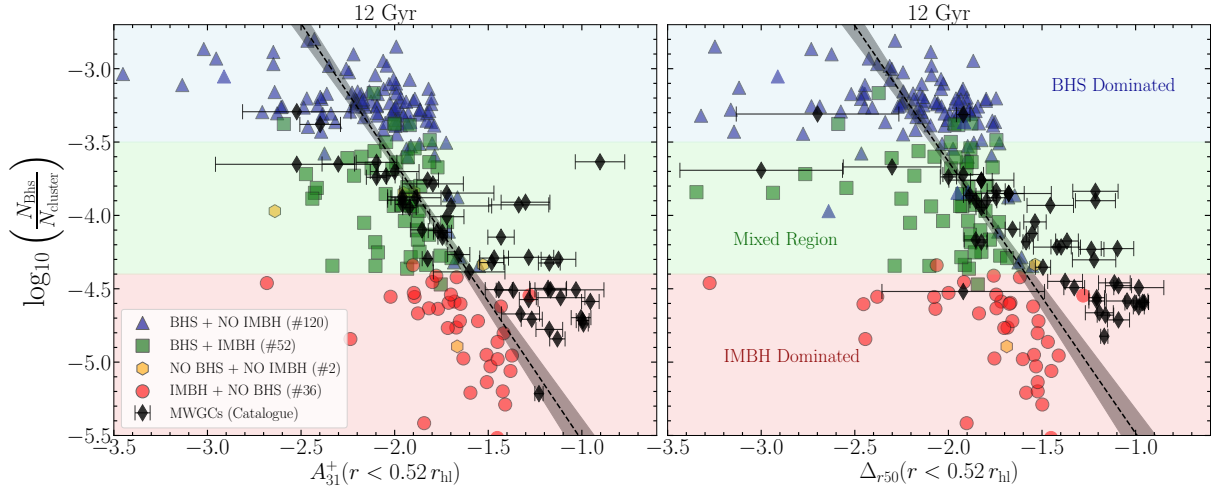


Figure 3.8: BHs retained in the MOCCA code as a fraction of the number of stars in the cluster. Black points are similar data derived from models in Weatherford et al. (2020), with errorbars taken as the $1\text{-}\sigma$ Gaussian-shaped uncertainties (see Weatherford et al. (2020) for details). The figure indicates the difference in segregation for the A_{31}^+ parameter (left panel) and the Δ_{r50} (right panel). The two power-laws are fitted to our simulated models in the MSD II. The extracted relations are denoted in equations (3.1) and (3.2).

Equivalently to Weatherford et al. (2020), we find both segregation parameters to be quite similar for our range of clusters, with fits following

$$\log_{10}\left(\frac{N_{\text{BHs}}}{N_{\text{cluster}}}\right) = (-1.89 \pm 0.17) \log_{10}(A_{31}^+) - (7.43 \pm 0.32) \quad (3.1)$$

$$\log_{10}\left(\frac{N_{\text{BHs}}}{N_{\text{cluster}}}\right) = (-1.85 \pm 0.18) \log_{10}(\Delta_{r50}^{13}) - (7.34 \pm 0.34). \quad (3.2)$$

We find that the A^+ parameter is more robust in our models, in terms of returning realistic values (non-negative values) and that this parameter has more frequently been used in previous studies (e.g., Alessandrini et al. 2016; Wu and Zhao 2021). Thus, the A^+ parameter is used for the bulk of our results.

By applying the method of Alessandrini et al. (2016) for calculating the A^+ parameter using equation (2.5), we compare 50 observed MW GCs with segregation values taken from Weatherford et al. (2020) with our simulated data. In Fig. 3.9 we show the logarithmic central surface brightness, $\log_{10}(\Sigma_c)$, as a function of the A_{31}^+ parameter at 12 Gyr snapshots, with Σ_c values obtained from Harris (2010) and Baumgardt et al. (2020). The segregation parameters are measured between populations `pop3` and `pop1` (turn-off MS stars and lightest MS stars, c.f. Fig. 2.3). Indicated for each simulation is also the specific model’s central state, either harboring a BHS, a BHS and an IMBH, only an IMBH or non of these properties. To match the most segregated clusters in the observed data, values from the MSD I are included. The right panel indicates the same quantities, but instead relate to the half-mass relaxation times at 12 Gyr for each of the clusters considered.

Firstly, we note larger segregation values ($A_{31}^+ > 0.04$) for the models with larger central surface brightness ($\Sigma_c > 10^{4.5} L_{\odot} \text{pc}^{-2}$) compared to the BHS models. These IMBH models have shorter half-mass relaxation times, are dynamically older, and generally retain fewer BHs which decreases the affect of BH heating. Models with a lower Σ_c value retain more BHs, which implies stronger dynamical heating from the BHs that quenches the relative difference in their distribution. In

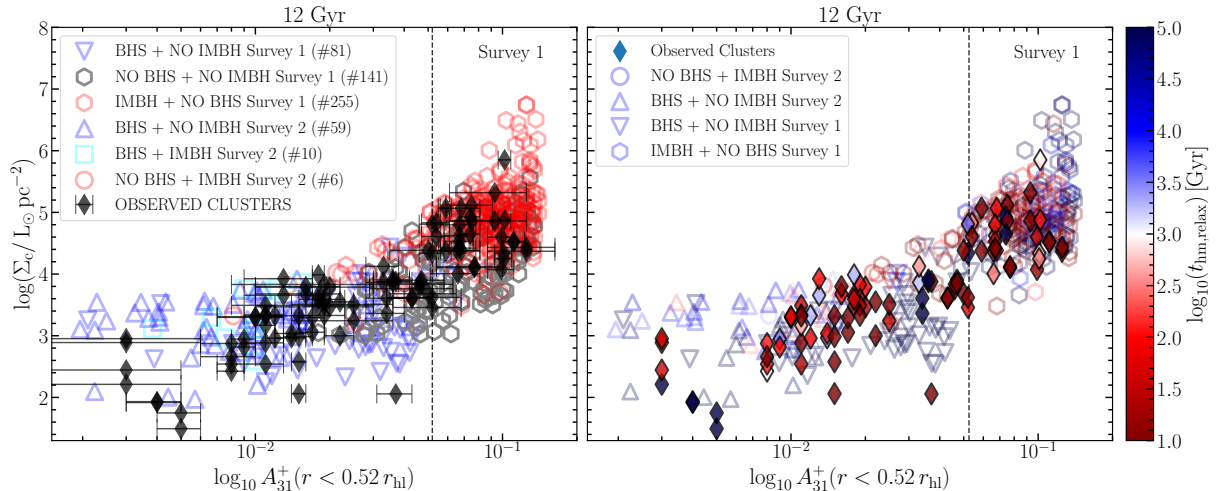


Figure 3.9: Central surface brightness as a function of A_{31}^+ , coloured after the central state of the cluster (left) and the same quantities but colour coded with the half-mass relaxation times of clusters at 12 Gyr for MOCCA and observed data (right). The vertical lines indicate the segregation value for the most segregated cluster from MSD II. Beyond this point, only MSD I clusters are present.

accordance with Wu and Zhao (2021), models with a larger core-to half mass ratio (in our case, core- to half-light radii) are less segregated (this represents the models in the bottom right quadrant in Fig. 3.5).

We find, in general, smaller segregation values in the MSD II models compared to observed clusters. In the MSD II simulations, we only sample a few of the observed clusters present in the MW (see Section. 3.2) whilst also only having segregation data from 50 of the observed MW GCs. Generally, the models in MSD II have implemented updated prescriptions for the evolution of massive stars that lead to the formation of stellar-mass BHs with masses up to $45 M_{\odot}$. A significant fraction of these BHs are retained in the cluster and their presence leads to lower segregation values. We find the connection that models with shorter half-mass relaxation times are generally more segregated. Furthermore, the MSD I data also includes models without IMBHs or BHS. These clusters can have quite large half-mass relaxation times (> 3 Gyr) while still being substantially segregated (comparable to IMBH models). Hence, the cluster’s dynamical age is a strong signature of large segregation in cases where we have a massive central BH, however, the absence of BHs in the cluster also produces heavily segregated clusters since the effect of BH heating is suppressed.

3.3.1 Segregation in stellar exotica

Figure 3.10 displays the cumulative number distribution of the two clusters in Table. 2.4. The figure indicates the distributions of BBHs, NS-MS binaries and BSS. Firstly, notice the higher formation rate of BSS in the IMBH system compared to the BHS. Since the formation channels of BSS are either via mergers or collisions, the dynamically older system’s increased rate of encounters allows for a higher probability of their formation paths. BSS are typically perfect candidates for measuring mass segregation from a few points of view; they are bright, which means their detectability is increased; they are heavier than regular MS stars, which means more substantial segregation; and finally, their formation paths typically occur close to the cores in GCs which makes their numbers a good proxy for the dynamical age of the cluster. Several candidates have also been observationally confirmed in GCs (see, e.g., Piotto et al. 2004).

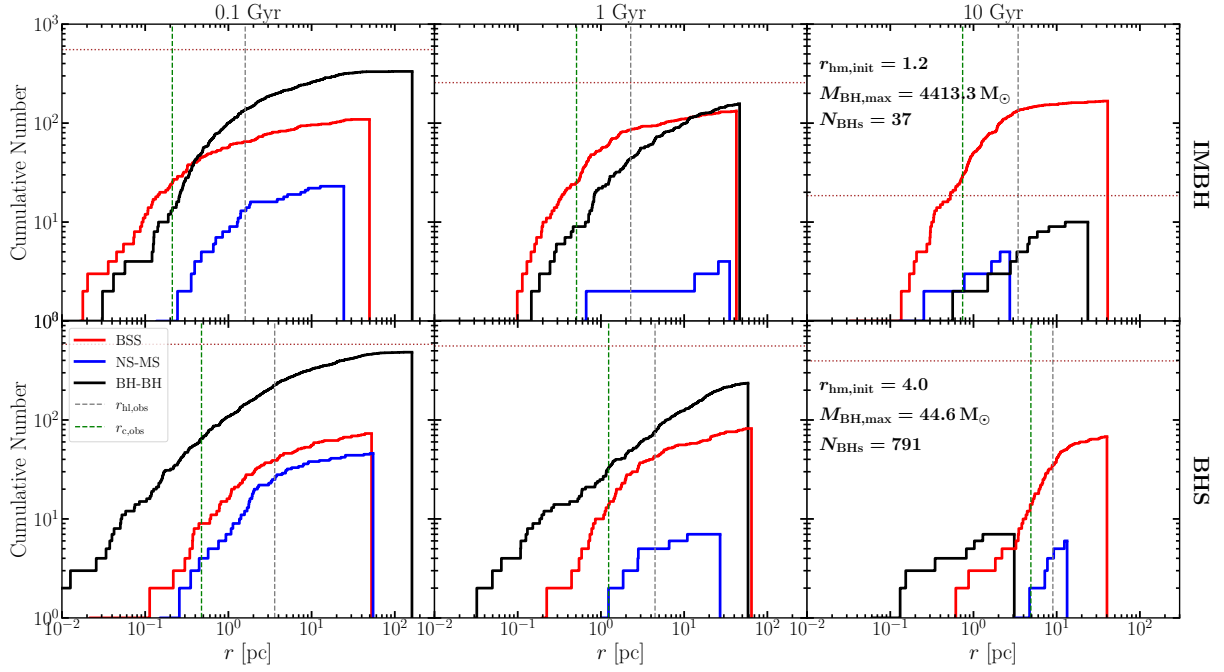


Figure 3.10: Analogous to Fig. 3.7, but instead indicating three populations of stellar exotica, showing BSS in red, NS-MS in blue and BBH in black solid lines.

The top right panel in Fig. 3.10 displays more prominent segregation for BSS compared to the bottom right panel. This is mainly since the dense core allow these to crowd the most inner regions, and that the short relaxation times allow for more collisions and/or accretion events in the core, which increases their formation rates. In the BHS model, we find fewer BSS and more minor segregation. The many BHs can dynamically interact with these systems and disrupt their progenitor binaries. Inside the half-light radius, we find about twice as many BSS in the IMBH model compared to the BHS model at 10 Gyr. The innermost BSS in the dense model has a cluster-centric position of \sim six times as small as in the BHS model.

The NS-MS follow the same generalities as the BSS in terms of segregation. The lack of BH burning allows them to segregate to shorter orbits. In general, the NS-MS binaries are clearly heated to the cluster’s outskirts in the BHS model, where they distribute almost entirely outside the core. Instead, some BBHs distribute closer to the core and are most likely part of the BHS itself. BBHs have increased formation rates in the dense cores of IMBH models but also have a higher chance of being disrupted or being ejected from the core. A higher fraction stellar-mass BHs in the IMBH models are found in BBHs as compared to the BHS model. Over time, we notice a quick depletion of BBHs in these models where binaries (or components within) will either merge with the large central IMBH or get ejected. Similarly, since NS distribute closer to the core, they can find a MS partner in an exchange encounter to form a binary system

The dynamical formation processes for BSS are shown as a function of time in Fig. 3.11, where we include BSS formed in collisions, binary-single and binary-binary interactions. The number of BHs, the most massive BH and the half-mass relaxation time at 10 Gyr are also shown. In support to Fig. 3.10, we find a much larger formation rate over time for the dense model with short relaxation time, further supporting the argument that dynamically old clusters indeed show stronger segregation and higher formation of BSS.

A quantitative analysis over the segregation of BSS is made in Fig. 3.12. The figure is similar to the left panel in Fig. 3.9, but instead indicating the segregation parameter A_{53}^+ between pop5

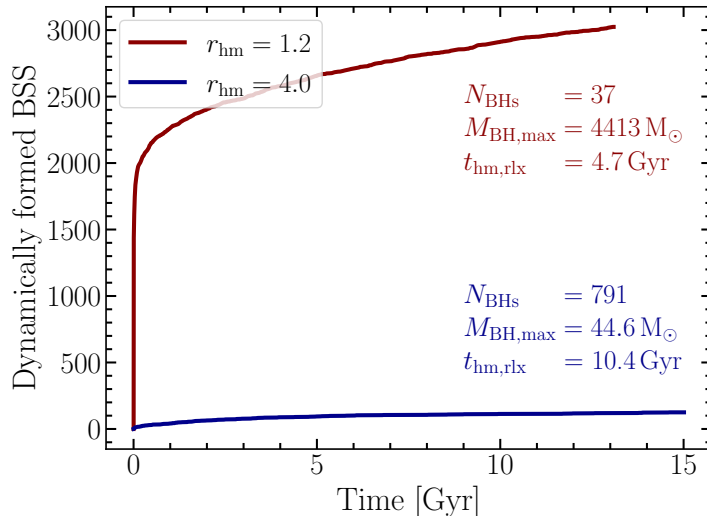


Figure 3.11: Number of dynamically formed BSS as a function of time for the two clusters presented in Table. 2.4. The formation pathways included are 2-body collisions and mergers during binary-single + binary-binary interactions. The text indicates 10 Gyr values for the number of BHs (N_{BHs}), mass of the most massive BH ($M_{\text{BH,max}}$) and the half-mass relaxation time ($t_{\text{hm,rlx}}$) of the clusters.

(BSS) and `pop3` (MS stars with median mass $M < 0.47 M_{\odot}$). The figure indicates IMBH models in red and non-IMBH models in blue, determined through the mass of the most massive BH at 12 Gyr. Indicated are also some boundary models; the green squares depict models with small IMBHs, while the triangles show models harbouring a BHS. Note that this data is taken from MSD I for better statistics over BSS segregation. With this larger sample of models, there is a clear cutoff in the central surface brightness between the models with massive and low-mass BHs. The limit is indicated in the figure as a horizontal line at $\Sigma_{\text{c}} = 10^{4.4} L_{\odot} \text{pc}^{-2}$.

IMBH dominated models are in general shifted to the right on the segregation axis, with segregation values up to $A_{51}^{+} \approx 0.6$ (a little more than one order of magnitude larger compared to the most segregated A_{31}^{+} cluster in MSD II), while the models with few BHs are more mixed. Pure BHS models (orange triangles) display a shift to the left on the segregation axis. The orange triangles that still lie beyond $A_{51}^{+} \approx 5.5 \times 10^{-2}$ have BH masses close to $100 M_{\odot}$ and retain close to 50 BHs. The shift to the right on the segregation axis for IMBH models suggests a strong correlation between the dynamical age of the cluster and the more heavily segregated BSS.

Despite finding signatures that the majority of BSS form close to clusters’ cores, there are suggestions for BSS bimodalities in GCs (Ferraro et al. 2012; Hypki and Giersz 2017). Recent observational studies have revealed evidence of clusters showing a bimodality in their BSS distributions (see caption in Fig. 10 in Hypki and Giersz (2017) for a list taken from Harris (1996)). Ferraro et al. (2012) suggest that BSS bimodality in clusters typically occur for clusters with large relaxation times where dynamical friction has not had time to affect the most remote BSS, implying a peak of BSS in the outskirts of the cluster. In dynamically older systems, dynamical friction has “reached” this point, and a peak only in the innermost parts should be created.

Hypki and Giersz (2017) show using the MSD I, however, that the bimodality is a transient feature that cyclically shifts between unimodal and bimodal distributions independent of the dynamical age of the clusters. The bimodality is additionally very dependent on the bin sizes of choice and can shift over only a few 100 Myr in time. They also note that the presence of an IMBH should not affect the BSS populations at large radii.

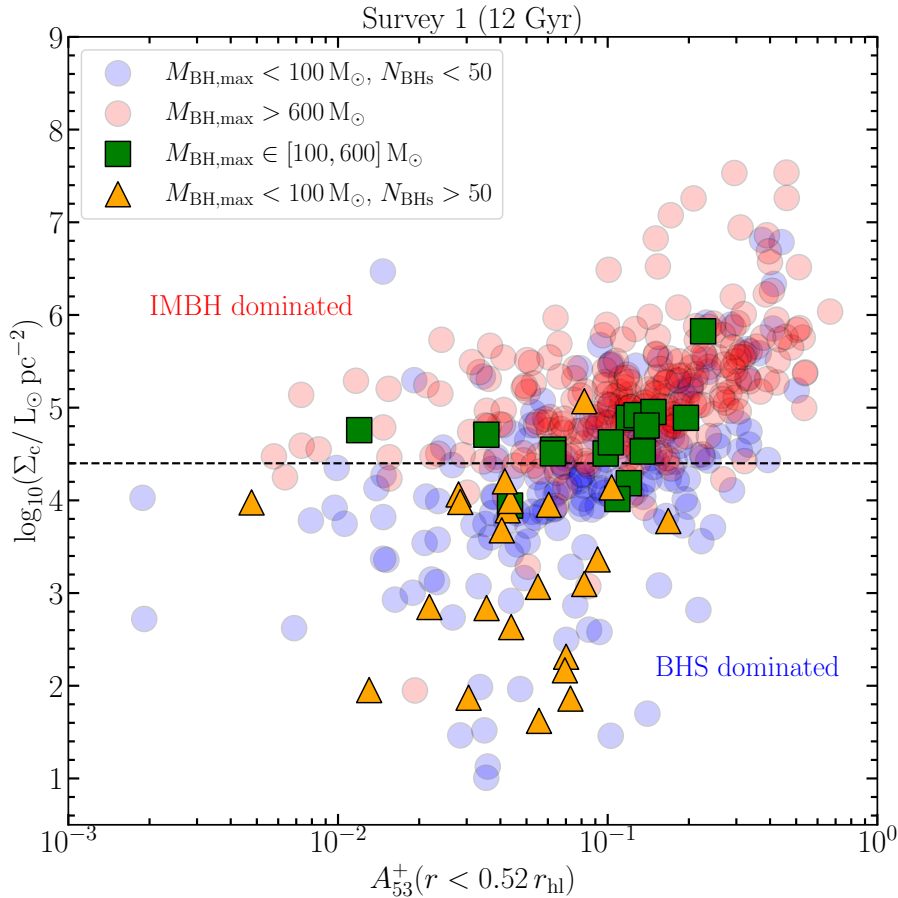


Figure 3.12: Central surface brightness of clusters using the MSD I as a function of A_{53}^+ , calculated between `pop5` (BSS) and `pop3` (lightest MS population). We indicate the cut between IMBH and BHS dominated models at $\Sigma_c = 10^{4.4} L_\odot \text{pc}^{-2}$. The yellow and green triangles and squares show boundary models; the yellow ones where there clearly is a BHS without an IMBH present and the green squares; models with a small mass IMBH. The blue and red models are filtered depending on the mass of the most massive BH.

We perform a similar analysis on our two clusters in Table 2.3, with $r_{\text{hm,init}} = 1.2, 4.0 \text{ pc}$ and the clusters in Table 2.4, using equation (2.7). Both models in Table 2.3 show bimodal distributions, with stronger bimodal signatures for the model retaining an IMBH. These findings are in disagreement with Ferraro et al. (2012) who suggested that BSS distribution in dynamically old systems should not be bimodal. Our results are in agreement with Hypki and Giersz (2017) who found that bimodal distributions can be found in both types of clusters. A further explanation we provide is that in this specific timestep investigated (12 Gyr), BSS that have been earlier close to the core might have been ejected out of the core and have not yet segregated inwards. Following Hypki and Giersz (2017), we also stress the uncertainty in choosing the sizes of our bins. Tuning this number can significantly change the signatures of bimodalities. Note also that in the IMBH model, the increase in BSS frequency occurs only inside the width of one bin. Few BSS or HB stars in a bin can generate fluctuations in the BSS/HB-values. In the models, there are typically a few BSS and a few tens of HB stars in each radial bin considered. We did not find the presence of any significant bimodality in the other clusters from Table 2.3, although the $r_{\text{hm}} = 1.2$ model in Table 2.4 instead shows a unimodal distribution of BSS (one can argue for a small unimodality in the $r_{\text{hm}} = 4.0$ as well), with a large peak close to the core.

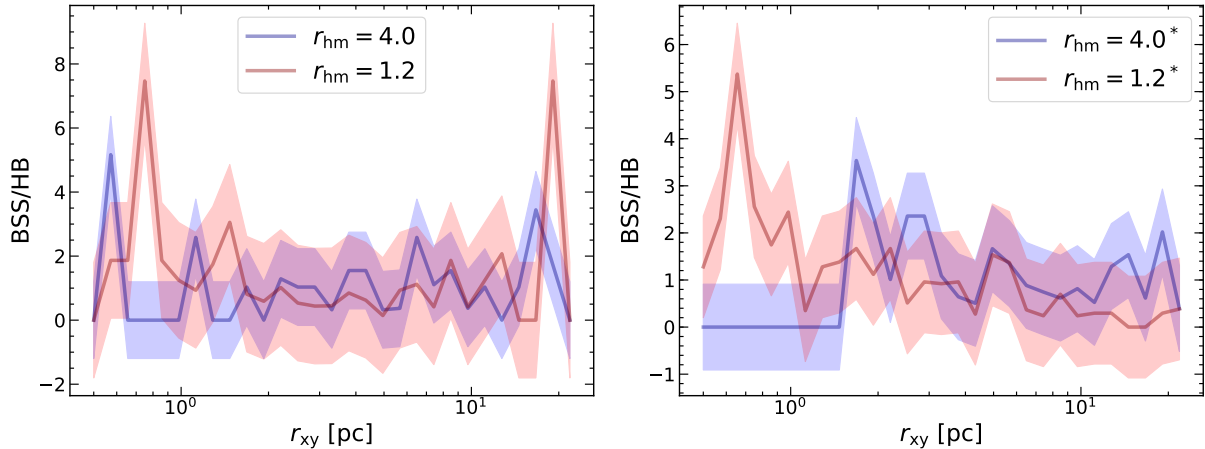


Figure 3.13: Bimodal (left) and unimodal (right) frequencies of BSS in four various clusters. The BSS frequencies on the vertical axis is normalized to the number of horizontal branch stars (c.f. equation 2.7). The left panel consider two models from Table. 2.3 which shows a bimodal distribution, in particular, for the IMBH model in red; while the right panel instead shows a unimodality in BSS frequencies for the cluster models in Table. 2.4 (denoted with asterisks). In these models, the number and sizes of bins are 30 bins on a logarithmic scale between 0.5 and 22 pc.

3.3.2 Summarizing segregation in different populations

In Fig. 3.14, we compare the distributions of segregation between more combinations of populations. Recall that we denote the populations considered by a subscript of their population name (where subscript 32 would be measuring the mass segregation between populations pop3 (lightest MS stars) and pop2 (MS stars with median masses of $M = 0.65 M_{\odot}$) as defined in Fig. 2.3). Each distribution shows a kernel density estimation (KDE) of the PDFs for the populations in each cluster at 12 Gyr, with vertical lines through the peaks of the IMBH distributions. Indicated are also arrows for each distribution where the length of the arrow probes the segregation difference between the peak of the IMBH and corresponding BHS model.

The figure highlight some distinct signatures; firstly, A_{31}^+ and A_{53}^+ possess the largest values of segregation in the IMBH models, contrary to the BHS for the combinations of both main sequence stars and heavier objects. The larger values are expected since the populations' mass difference is more substantial. In the MSD II models, the IMBH clusters are more segregated independent of the populations used, with the smallest (peak value) difference for A_{21}^+ . Here the peak of the distribution is similar between the systems; however, the most segregated cluster in the IMBH is twice as segregated as the corresponding BHS model. The BSS models in the right panel show no significant peak in their distribution which is why the MSD I data is used in Fig. 3.12. The explanation for this is that while BSS typically form close to the core, they can also form further out in the cluster (c.f. Fig. 2.7). Since they are not that numerous, their orbits can be more extended in general compared to the lighter MS populations and yield negative values.

We conclude that larger mass difference between populations yields more substantial segregation, while smaller mass differences generate more mixed systems. Combined with Figs. 3.10, 3.11 and 3.12, this highlights that dynamically older systems retain fewer BHs, form more BSS, have increased central surface brightness and are more segregated. These signatures, combined with large central densities and short relaxation times are connected to the presence of IMBHs in our cluster models, and might give further insight into the presence of IMBHs in observed GCs.

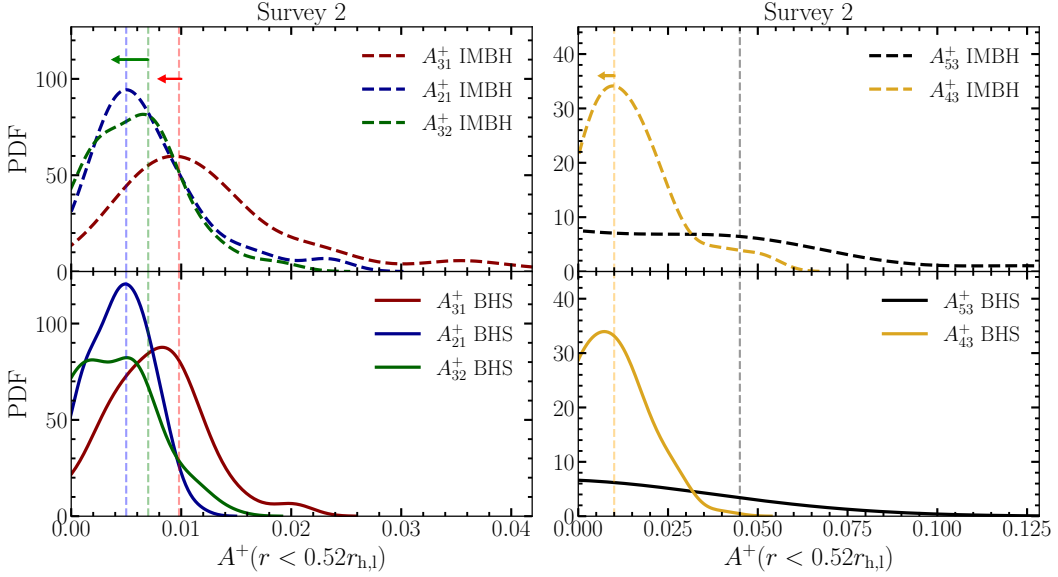


Figure 3.14: Distributions of the Δ_{r50} and A^+ parameters between main sequence populations *pop1*, *pop2* and *pop3* for IMBH models (top left) and BHS models (bottom left). Similar distributions are shown in the right panels in the right column, but for the heavier populations. Vertical lines indicate the peak of the IMBH distributions and the length of the arrows probe the segregation difference compared to the corresponding BHS peak. In this case, BHS models include all models with a maximum BH mass of less than $100 M_{\odot}$.

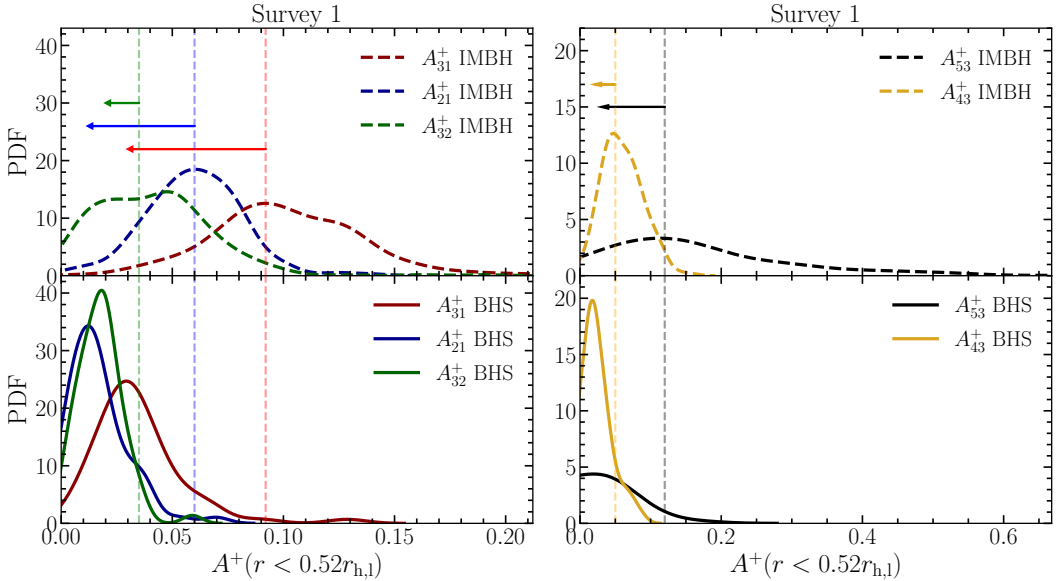


Figure 3.15: Similar to Fig. 3.14 but instead using only MSD I data. Since MSD I contains several models which neither host an IMBH nor a BHS, an extra condition that BHS models must include more than 50 BHs is set.

In Fig. 3.15, the same procedure is conducted, but for MSD I models. The larger sample of initial conditions for these clusters provides a larger spread in segregation, both for MS- and heavier populations. In general, the most segregated cluster have a factor of five larger segregation value (A_{31}^+) compared to MSD II. IMBH models show three distinct regions in the MS populations (top left panel), with smallest segregation between populations *pop3* and *pop2*. Indicated by the

arrows, the difference between BHS models and IMBH models is larger for MSD I than MSD II data. We find that models hosting IMBHs have a wider spread in segregation in general, as opposed to BHS models. Additionally, MSD I models are found to better match with the most segregated observed clusters, while MSD II models better represents systems that are more mixed.

3.4 Binary properties

In this subsection, we investigate the results of binary populations in our clusters. Ordinarily, we quantify BHS and IMBH models depending on their most massive BH and exclude problematic models.

3.4.1 Binary fraction distributions

The left panel of Fig. 3.17 shows the binary fraction inside the core radius of models at 12 Gyr as a function of the binary fraction between one and two half-light radii. We restrict ourselves to initial binary fractions of 95 % since this is the range with the largest subsample of models in MSD II. The figure can be directly compared to Fig. 7 in Aros et al. (2021), where the same procedure is performed, but using models with initial binary fraction of 10 % from MSD I (reproduced in the right panel). We find a clearly defined region of IMBH models having lower binary fractions and more extensive segregation, denoted as red circles to the left of the equal fraction line. BHS models generally lie close to the equal binary fraction line in both the surveys. Models in the MSD II can retain hundreds of BHs. While most crowd the innermost cores, they are also present further out in the cluster (see e.g., Fig. 3.7 and Fig. 5.2). The large influence radius of a BHS energizes the cluster to work *against* mass segregation (Aros et al. 2021 and references therein) which increases the binary fractions outside the half-light radii of clusters.

Dynamical recoil from gravitational encounters can also result in the migration of binaries from the core to the outer parts (or halo) of the cluster. In terms of total binary fractions, IMBH models have decreased values of the overall binary fractions due to the large central densities and shorter relaxation times, increasing disruption, ejections and merging events. The BHS models do not have such dense cores, and the disruption rates become lower, at least for the harder binaries.

We find the difference of initializing the simulations with a low, as opposed to a high binary fraction, that the majority of binaries in the $f_b = 0.1$ case distribute closer to the core, with only a few models below the equal fraction line. The models with initially low binary fractions are typically harder since their distribution of semi-major axes is different (uniform in $\log(a)$ up to 100 AU for semi-major axis a , see Table. 2.2 and Fig. 3.16). The higher fraction of hard binaries allows them to survive for longer, and they can migrate closer to the cluster's cores. We note that in models without any IMBH or BHS in MSD I, many binaries are still retained due to the lack of encounters with BHs. Instead, in accordance with Leigh et al. (2015), we notice that a higher initial binary fraction is required to account for the observed binary fraction outside the half-light radius. In this case, the binaries are initially softer, with larger semi-major axis values (according to Kroupa (1995), see Table. 2.2 and Fig. 3.16). Also note that the MSD II simulations have updated fallback prescriptions (Fryer et al. 2012; Belczynski et al. 2016) that result in higher BH masses and an increased retention of stellar-mass BHs. The higher number of BHs in these models implies increased heating from the BHS that puts the binaries on wider orbits. A comparison figure between the initial semi-major axis distribution for the setups in MSD I, as opposed to MSD II is provided in Fig. 3.16. The softer initial binaries in MSD II are easier to disrupt which explains how the binary fraction can drastically drop from 95% down to

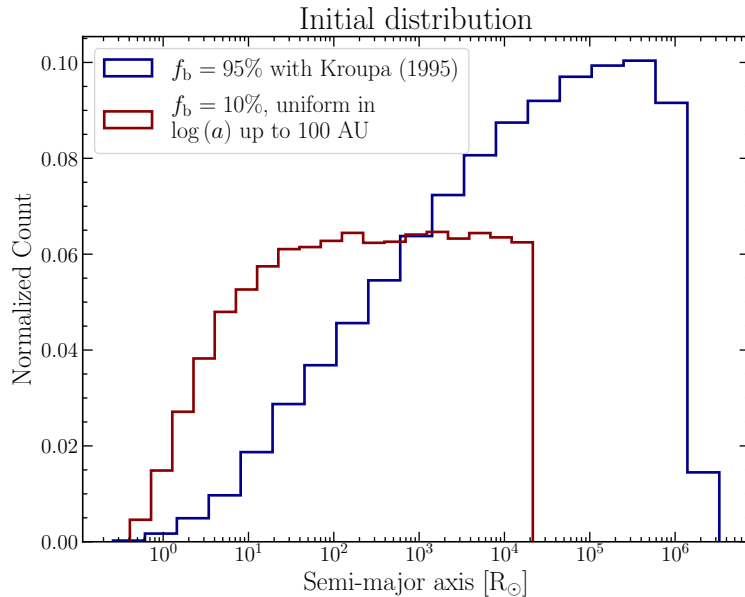


Figure 3.16: Initial distribution of semi-major axis for models with high (95 %, darkblue solid line) and low initial binary fractions (10 %, darkred line). The vertical axis is normalized such that the sum of counts over all bins is unity. Models with an initially low binary fraction follows a uniform distribution in $\log(a)$ whereas models with initial binary fraction of 95 % contain binaries that are significantly softer and extend out to large semi-major axis values (Kroupa 1995; Belloni et al. 2017).

$\approx 14\%$ over the cluster evolution, whereas the harder binaries in MSD I are harder to disrupt and survive for longer.

An exciting finding indicated in Fig. 3.17 is the presence of models hosting both an IMBH and a BHS. In the left panel of the figure, these are indicated as red squares. Despite these being slightly less segregated than the other BHS models (blue squares), they distribute further out than pure IMBH models. From the colour bar, it is clear that the masses of the IMBHs are not extremely high, but it still indicates that the presence of many BHs is the dominant factor in quenching mass segregation, whereas the IMBHs in these models have less of an effect. In cases where the IMBH would stand for the majority of mass in the cluster, or if the cluster would still possess a smaller influence radius, the segregation from IMBHs might dominate the dynamical heating of BHs. However, this has not been noticed in our models.

As will be shown later in Section. 3.4.2, the semi-major axis distribution of binaries are also typically different between IMBH and BHS models. Since the hardness of binaries is a main key in the probability of disruption, this can also be a factor for the creation of binaries that survives very close to the core.

Similar to Fig. 3.17, we see a depletion in binary fractions in IMBH models compared to BHS models in Fig. 3.18. The image shows the binary fraction distributions as a function of projected radius, normalized to the half-light radii of clusters. The left panels show models taken from the MSD II with initial binary fraction of $f_b = 0.95$ and the right panels model with $f_b = 0.1$ in MSD I models. The median binary fraction is extracted in each bin, with a power-law fitted through them. The figure can be compared to Fig. 6 in Aros et al. (2021). For the MSD II models, we find a general increase in binaries close to the core in IMBH models that quickly depletes going outwards as $f_b \sim (r/r_{hl})^{-0.132 \pm 0.007}$. BHS models follow a more uniform distribution throughout the cluster ($f_b \sim (r/r_{hl})^{-0.013 \pm 0.003}$) and have in general a higher fraction of retained

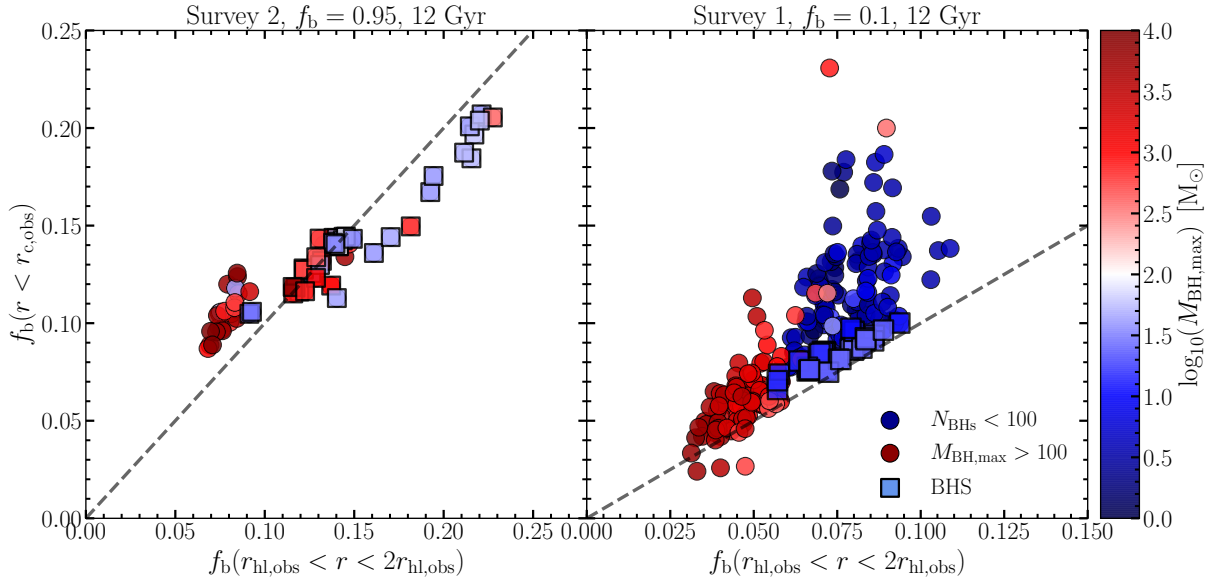


Figure 3.17: The binary fraction inside the observational core radius on the vertical axis vs the binary fraction between one and two half-light radii on the horizontal axis. Right panel; analogous to Fig. 7 in Aros et al. (2021), left panel; same quantities with initial binary fraction of $f_b = 0.95$. MSD II data is filtered to not include problematic models. We have included the lines where these quantities are equal. The points each represent one cluster where the colour gradient represents the mass of the most massive BH. We indicate clusters with over 100 BHs retained with filled squares.

binaries for $f_b = 0.95$. In MSD I, the power-law fit is now more shallow in the IMBH models than in the non-IMBH. The distributions here instead follows, $f_b \sim (r/r_{\text{hl}})^{-0.059 \pm 0.006}$ and $f_b \sim (r/r_{\text{hl}})^{-0.133 \pm 0.004}$ for the IMBH and non-IMBH models respectively. Worth noting is that the initial binary fractions in the cluster play an important role in distribution of binaries.

The increased core binary fraction for non-IMBH MSD I models in Fig. 3.18 is most likely explained by the models neither hosting a BHS nor an IMBH. In cases where there is a negligible amount of BHs, more binaries survive and can hence populate the innermost core without being disrupted. In contrast, an IMBH allows disruption of even the hardest binaries due to the high velocity dispersion close to the core, which decreases core binary fractions.

Models hosting more BHs are generally dynamically younger and retain more binaries in the core due to their longer relaxation times. As explained above, the presence of an IMBH reduces the binary fraction. However, it is evident from both Fig. 3.17 and 3.18 that models hosting none of these systems still can retain a substantial amount of binaries while also keeping them close to the core. These models do often have large segregation (seen in the left panel in Fig. 3.9), and can still maintain longer relaxation times (right panel). We provide further discussion around this in Section. 4.1.3.

3.4.2 Dynamical properties of binaries

In addition to Figs. 3.17 and 3.18, we give further arguments for the increased number of binaries very close to the core for IMBH models with initial binary fractions of $f_b = 0.95$. Fig. 3.19 displays the number of binaries as a function of their semi-major axes, in units of R_\odot at 12 Gyr. We indicate the semi-major axis distributions using the models in Table. 2.4. It is apparent that the IMBH cluster model retains a higher fraction of lower semi-major axis binaries.

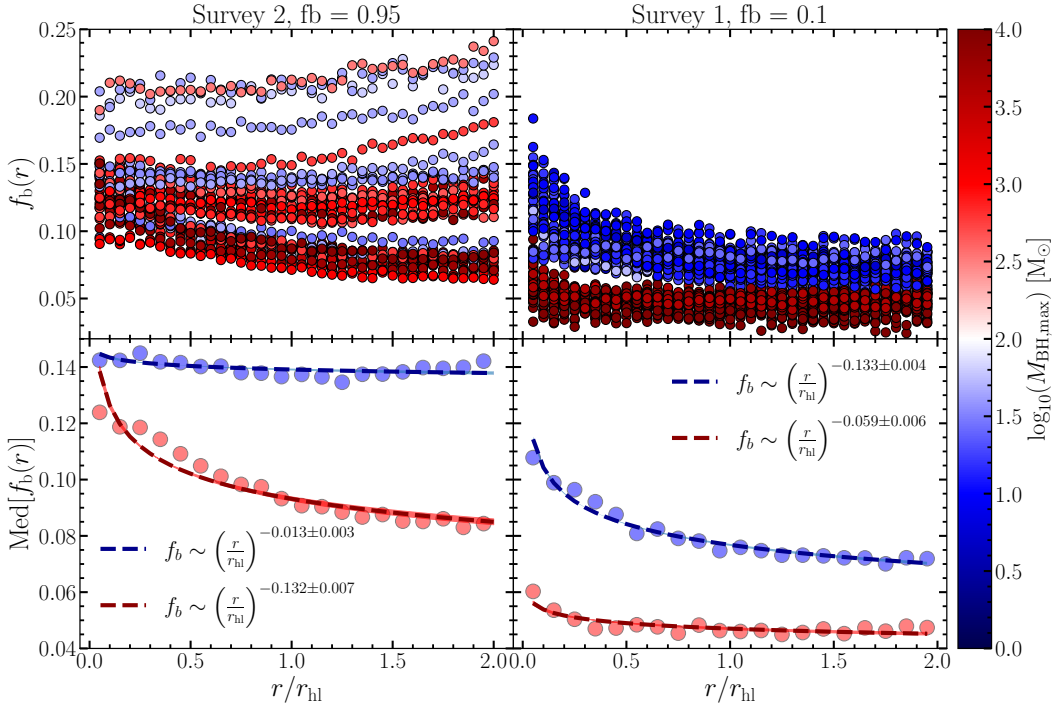


Figure 3.18: Binary fractions as a function of the normalized radius of clusters. Each row of points represents the binary fraction of a specific cluster in bins of the half-light radius of the cluster. Hence, a value of unity on the x-axis represents the clusters’ half-light radius. In the bottom panel, we indicate the median values between all models in each bin. A power-law is fitted through these median values with covariance error shown in shaded colours.

The fewer BHs allow for a more dynamically active and dense core, increasing the rate of close encounters between binaries, which generally makes them harder through Heggie-Hills law (Heggie 1975). Presumably, this should also increase the dynamically formed binaries in this model. The increased hardness of binaries increases their binding energy and reduces the chance of ionization or disruption events. Despite this, the shorter relaxation time of the IMBH model results in a more substantial depletion in the overall binary fraction.

In Fig. 3.20, we investigate potential observable X-ray sources (WD-MS binaries) as a function of their position inside various lagrangian radii; 10, 50, 70 and 98 % of the two clusters in Table. 2.4. The goal is to highlight their segregation differences and compare their formation channels. The number of WD-MS binaries are indicated in the legends inside the figures, with an additional mark of dynamically formed (as opposed to primordially formed) WD-MS in the clusters. Mass transfer events between WD-MS binaries form what is called *Cataclysmic Variables* (CVs) and are typically hard to detect in GCs due to the large stellar crowding. Although, recent studies have revealed some potential candidates inside GCs (e.g., ω Cen, NGC 6572, NGC 6397, 47 Tuc, see Belloni et al. 2019 and references therein), via e.g., *Hubble Space Telescope* and *Chandra X-ray observatory*. Belloni et al. (2019) find that in these clusters, the populations tend to be more segregated in more core collapsed clusters and comparable in distribution to main-sequence turnoff stars (MS_{TO}).

We find that the cluster with shorter relaxation time induces a larger number of potential CVs inside each considered radii. A dynamically older core implies a higher probability of developing hard and mass accreting binaries. Furthermore, we notice a larger fraction of dynamically formed WD-MS in the IMBH model and that their distribution is similar to that of the MS_{TO} , while

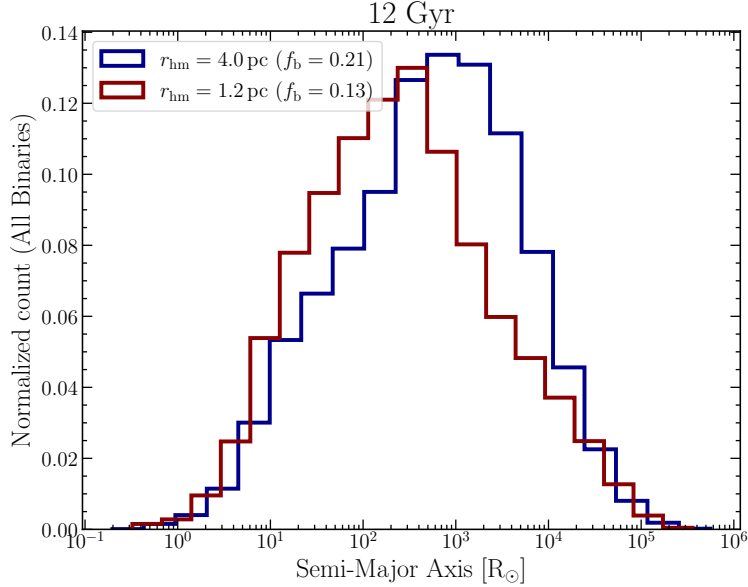


Figure 3.19: Histogram displaying the semi-major axis distribution for all binaries inside the cluster models in Table. 2.4. The binary fractions (f_b) and BHs retained (N_{BHs}) in each cluster are also indicated. The vertical axis is normalized such that the sum of counts for all bins is unity.

the MS_{TO} in the BHS distribute closer to the centre. Clearly, the segregation of these binaries should depend on the mass of the WD companion inside the binary pair and their dynamical interactions with the retained BHs. The segregation difference in these clusters is apparent, with 50 % of the WD-MS population contained inside 4 pc in the IMBH model, while 50 % of the population extends out to 10 pc in the BHS model (top right panel).

3.5 Predicting BHs numbers and masses in observed GCs

In Fig. 3.21 we indicate observed GCs, with segregation parameters taken from Weatherford et al. (2020) and central surface brightness values from Harris (2010) and Baumgardt et al. (2020). Six particular clusters of interest are marked with values from the latter catalogue. BH candidates have been spectroscopically observed inside NGC 3201 and 47 Tuc (Strader et al. 2012; Miller-Jones et al. 2015; Giesers et al. 2018) and are marked with an asterisk. Askar et al. (2018a) and Askar et al. (2019b) perform global fitting relations and machine learning to theoretically find evidence for a substantial number of retained BHs in NGC 3201 and NGC 5466, with 191^{+110}_{-63} BHs retained in the simulated NGC 5466. Similarly, there has been suggestion for the clusters NGC 6535 (Askar et al. 2017; Askar et al. 2018a), NGC 6624 (claimed by Perera et al. 2017, contradicted by Gieles et al. 2018), NGC 6093 (Göttgens et al. 2021) and NGC 6535 (Askar et al. 2017) to host IMBH candidates. Following, we describe the fitting relations found to predict the central properties of these clusters.

In Fig. 3.22, the number of BHs (left panel) and the masses of IMBHs (right panel for models having a BH with mass, $M > 100 M_{\odot}$) is shown as a function of the A_{31}^+ parameter. The lines in the figure indicate power-law fits on a linear form for the log-log axes; $\log_{10}(X) = \alpha \log_{10}(A_{31}^+) + \beta$ to the scattered data for non problematic models, including both MSD I and MSD II. Here, X is either the number of BHs retained or the estimated IMBH mass. The

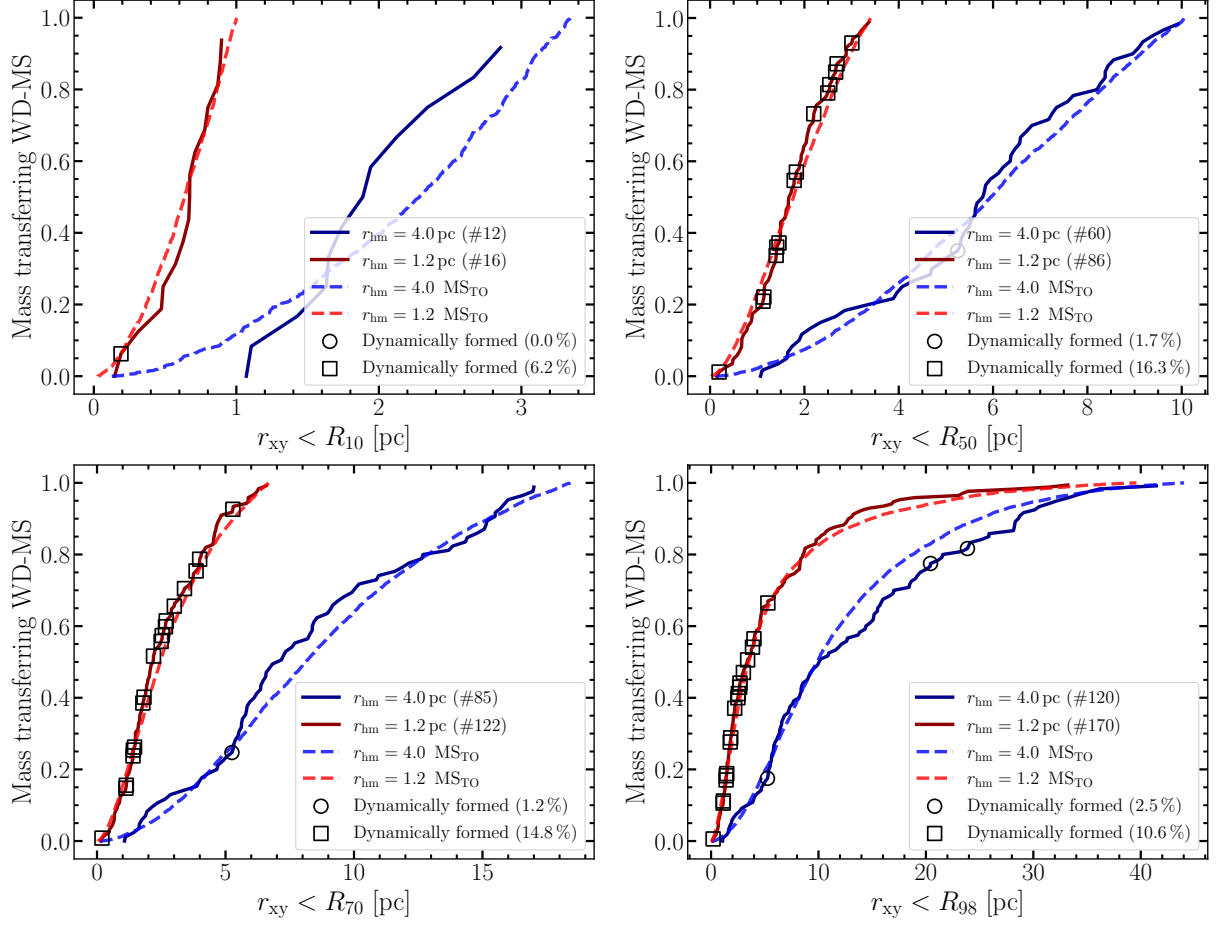


Figure 3.20: Cumulative radial frequencies of mass transferring WD-MS binaries and MS stars at turnoff mass (stars between 95 and 105 % of the turnoff mass). Each panel displays stars inside a particular Lagrangian radii, with percentage values indicated as R_p , where p is the percentage of use. Circles and squares indicate the position of binaries that have formed through dynamical interactions. Red (IMBH model) and blue (BHS model) lines indicate the two clusters from Table 2.4 with $r_{\text{hm}} = 1.2$ and $r_{\text{hm}} = 4.0$ pc respectively. The parenthesized numbers stand for the total amount of WD-MS binaries (top) and the percentage of binaries formed dynamically (bottom).

resulting fits follows

$$\log_{10}(N_{\text{BHs}}) = (-0.90 \pm 0.07) \log_{10}(A_{31}^+) + (0.08 \pm 0.14) \quad (3.3)$$

$$\log_{10}(M_{\text{IMBH}}) = (0.49 \pm 0.06) \log_{10}(A_{31}^+) + (4.27 \pm 0.12). \quad (3.4)$$

By plugging in observed segregation values into these relations, we extract the number of BHs in the 50 observed GCS and estimate the mass of a hypothetical IMBH in clusters having $A_{31}^+ \gtrsim 0.05$. The following subsections present our predictions for the six marked clusters in Fig. 3.21. Predicted values for each observed cluster is provided in Table 3.1. Note that errors are considered using the observed uncertainty in A_{31}^+ , but also, to account for the scatter around the fit, a running mean is performed in 40 logarithmic bins of A_{31}^+ . The variance in $\log_{10}(N_{\text{BHs}})$ and $\log_{10}(M_{\text{IMBH}})$ for each bin are combined with the least-square estimated error of the fit for the final predictions. Shaded areas and errorbars indicate this uncertainty around each mean value in Fig. 3.21, while the grey dashed lines display the uncertainty around the fitted line.

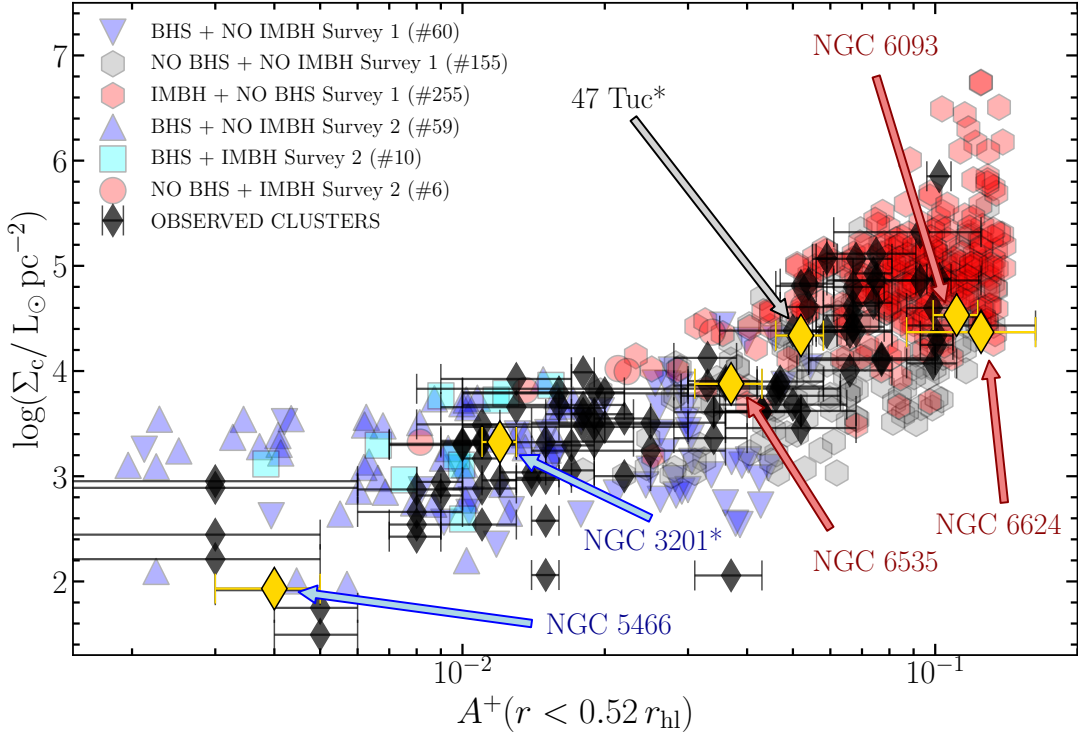


Figure 3.21: Similar to the left panel in Fig. 3.9. Six observed clusters are indicated in yellow diamonds; NGC 5466 and NGC 3201 (matching with BHS models), 47 Tuc and NGC 6535 (either harbouring an IMBH or very few BHs) and NGC 6093 and NGC 6624 (believed to harbour an IMBH). Simulated cluster models include data from both MSD I and MSD II.

3.5.1 47 Tuc (NGC 104)

The nearby cluster 47 Tuc (NGC 104) has been well analysed and several studies have speculated whether it contains an IMBH or a subsystem of stellar-mass BHs. In particular, it possesses a small core radius of $r_{c,obs} = 0.79$ pc compared to an extended half-light radius of $r_{hl,obs} = 3.61$ pc (Baumgardt et al. 2020) with significant mass segregation, which historically has been hard to reproduce in simulations (however, notable progress has been made recently in evolving an 47 Tuc like cluster, see e.g., Ye et al. 2021). A recent study by Kızıltan et al. (2017) suggest the retention of a $2300^{+1500}_{-850} M_{\odot}$ IMBH in the centre of 47 Tuc, probed from X-ray data and radio continuum emission (Grindlay et al. 2001; De Rijcke et al. 2006). Despite this, several subsequent studies reveal that the need of an IMBH may be redundant and can instead be explained with central stellar-mass BHs and binaries (Mann et al. 2019) or a small BHS of up to 200 BHs (Weatherford et al. 2020).

In simulations using the MSD II data, the closest model in terms of segregation and central surface brightness has a 12 Gyr central surface brightness of $\approx 4.1 \times 10^4 L_{\odot} \text{pc}^{-2}$, initial half-mass radius of $r_{hm,init} = 1.2$ pc and half-light and core radii of $r_{hl} = 5.0$ pc and $r_c = 0.56$ pc respectively. The cluster has a simulated maximum BH mass of $4500 M_{\odot}$ with 37 retained BHs at 12 Gyr. Concerning MSD I, the closest model retained only one BH, with a total mass of $\approx 19600 M_{\odot}$. We confirm that our results are more consistent with the presence of an IMBH in terms of the parameter spaced investigated, however, we stress that we are not able to completely resolve the core and half-light radius of this cluster, which further increase the uncertainty of our prediction. Employing the relation presented in Fig. 3.22, we find the estimated IMBH mass to be $M_{IMBH} = 4373^{+18652}_{-3542} M_{\odot}$.

Table 3.1: Observed cluster properties for 50 MW GCs. The predicted number of BHs in clusters is calculated using equation (3.3) and IMBH masses are estimated for models where $A_{31}^+ \gtrsim 0.05$, using equation (3.4). Upper and lower limits are calculated based on the uncertainties of the fit and the uncertainty in the observed segregation parameters. Clusters with an asterisk have known BH-candidates (e.g., Strader et al. 2012; Miller-Jones et al. 2015; Bahramian et al. 2017; Gieles et al. 2018; Shishkovsky et al. 2018). Columns six through nine shows the mass-to light ratio, half-light radius, total cluster luminosity and central surface brightness respectively, using data from Baumgardt et al. (2020).

Cluster Name	Number of black holes	IMBH mass [M_{\odot}]	A_{31}^+	$\pm 1\sigma$	M/L [$M_{\odot} L_{\odot}^{-1}$]	r_{hl} [pc]	L_{cluster} [$10^2 L_{\odot}$]	$\log_{10} \Sigma_c$ [$L_{\odot} \text{pc}^{-2}$]
NGC 104*	17^{+49}_{-12}	4373^{+18652}_{-3542}	0.052	0.006	1.96	3.64	45.6	4.34
NGC 288	92^{+127}_{-53}	0^{+0}_{-0}	0.008	0.001	2.16	5.83	4.32	2.43
NGC 1261	40^{+163}_{-32}	0^{+0}_{-0}	0.020	0.010	1.63	3.25	11.2	3.79
NGC 1851	10^{+23}_{-7}	5815^{+19960}_{-4503}	0.093	0.032	1.66	1.75	19.2	5.32
NGC 2298	37^{+88}_{-26}	0^{+0}_{-0}	0.022	0.003	1.91	2.4	2.92	3.55
NGC 2808	13^{+31}_{-9}	4951^{+17420}_{-3855}	0.067	0.009	1.51	2.45	57.2	4.62
NGC 3201*	64^{+158}_{-45}	0^{+0}_{-0}	0.012	0.001	2.16	3.8	7.41	3.32
NGC 4147	20^{+57}_{-15}	0^{+0}_{-0}	0.043	0.009	1.64	2.54	2.38	3.62
NGC 4590	56^{+183}_{-42}	0^{+0}_{-0}	0.014	0.002	1.8	4.43	6.78	2.97
NGC 4833	69^{+174}_{-49}	0^{+0}_{-0}	0.011	0.001	1.74	3.25	11.8	3.49
NGC 5024	25^{+67}_{-18}	0^{+0}_{-0}	0.034	0.006	1.77	6.43	25.7	3.36
NGC 5053	141^{+504}_{-110}	0^{+0}_{-0}	0.005	0.001	2.55	12.37	2.91	1.49
NGC 5272	23^{+63}_{-17}	0^{+0}_{-0}	0.036	0.006	1.61	3.39	25.2	3.87
NGC 5286	9^{+11}_{-5}	5995^{+12043}_{-4003}	0.099	0.012	1.48	2.37	23.9	4.59
NGC 5466	173^{+420}_{-122}	0^{+0}_{-0}	0.004	0.001	1.44	9.53	4.15	1.93
NGC 5904	25^{+62}_{-18}	0^{+0}_{-0}	0.033	0.005	1.81	3.51	21.8	3.86
NGC 5927	49^{+217}_{-40}	0^{+0}_{-0}	0.016	0.006	1.63	3.47	16.9	3.68
NGC 5986	42^{+187}_{-34}	0^{+0}_{-0}	0.019	0.011	1.9	2.77	17.6	3.83
NGC 6093	8^{+10}_{-4}	6341^{+12691}_{-4220}	0.111	0.012	2.08	1.76	16.3	4.53
NGC 6101	224^{+1597}_{-196}	0^{+0}_{-0}	0.003	0.002	2.56	9.56	6.96	2.21
NGC 6144	69^{+198}_{-51}	0^{+0}_{-0}	0.011	0.002	2.49	3.63	3.18	2.88
NGC 6171	52^{+171}_{-30}	0^{+0}_{-0}	0.015	0.002	2.22	2.86	3.38	3.32
NGC 6205	59^{+240}_{-46}	0^{+0}_{-0}	0.013	0.004	2.31	3.46	23.6	3.66
NGC 6218	69^{+198}_{-51}	0^{+0}_{-0}	0.011	0.002	1.92	2.83	5.58	3.34
NGC 6254*	44^{+106}_{-31}	0^{+0}_{-0}	0.018	0.002	1.86	2.97	11.0	3.65
NGC 6304	17^{+65}_{-13}	0^{+0}_{-0}	0.050	0.015	1.57	1.95	8.03	4.38
NGC 6341	13^{+36}_{-10}	4915^{+19433}_{-3923}	0.066	0.015	2.16	2.39	16.3	4.01
NGC 6352	47^{+149}_{-35}	0^{+0}_{-0}	0.017	0.002	2.21	2.88	2.93	3.06
NGC 6366	52^{+156}_{-39}	0^{+0}_{-0}	0.015	0.001	1.71	3.77	2.19	2.58
NGC 6397	15^{+34}_{-10}	4652^{+15674}_{-3587}	0.059	0.003	1.66	2.16	5.82	5.07
NGC 6535	23^{+62}_{-16}	0^{+0}_{-0}	0.037	0.006	2.64	2.67	0.83	3.88
NGC 6541	13^{+34}_{-9}	4988^{+18886}_{-3945}	0.068	0.013	1.75	2.29	16.7	5.07
NGC 6584	33^{+124}_{-26}	0^{+0}_{-0}	0.025	0.011	1.34	3.44	7.61	3.24
NGC 6624	7^{+10}_{-4}	6721^{+14784}_{-4620}	0.125	0.038	2.09	2.33	7.47	4.37
NGC 6637	19^{+76}_{-15}	0^{+0}_{-0}	0.046	0.017	1.72	2.41	9.01	3.76
NGC 6652	12^{+30}_{-8}	5301^{+20066}_{-4193}	0.077	0.023	1.8	1.47	2.67	4.10
NGC 6656*	44^{+97}_{-30}	0^{+0}_{-0}	0.018	0.001	2.05	3.15	23.2	3.99
NGC 6681	12^{+27}_{-8}	5233^{+17723}_{-4040}	0.075	0.016	1.84	2.14	6.30	5.12
NGC 6715	12^{+23}_{-8}	5199^{+15037}_{-3863}	0.074	0.007	2.1	3.58	84.8	4.92
NGC 6717	18^{+62}_{-14}	0^{+0}_{-0}	0.047	0.011	1.55	3.65	2.31	3.89
NGC 6723	75^{+206}_{-55}	0^{+0}_{-0}	0.010	0.003	2.01	3.55	8.81	3.29
NGC 6752	16^{+40}_{-11}	4455^{+16493}_{-3507}	0.054	0.007	2.34	2.87	11.8	4.83
NGC 6779	42^{+116}_{-36}	0^{+0}_{-0}	0.019	0.004	1.74	2.95	10.7	3.59
NGC 6809	83^{+172}_{-56}	0^{+0}_{-0}	0.009	0.001	2.06	4.58	9.37	2.95
NGC 6838	92^{+156}_{-58}	0^{+0}_{-0}	0.008	0.002	1.72	3.41	3.81	2.87
NGC 6934	17^{+63}_{-13}	4373^{+23535}_{-3688}	0.052	0.016	1.52	2.95	8.95	3.46
NGC 6981	224^{+2318}_{-204}	0^{+0}_{-0}	0.003	0.003	1.35	4.14	5.10	2.89
NGC 7078	9^{+10}_{-4}	6084^{+11144}_{-3935}	0.102	0.006	1.58	2.03	40.1	5.85
NGC 7089	9^{+10}_{-5}	6055^{+11433}_{-3958}	0.101	0.008	1.75	3.04	35.4	4.34
NGC 7099	13^{+33}_{-9}	4951^{+18098}_{-3888}	0.067	0.011	1.91	2.54	7.49	4.79

3.5.2 NGC 3201

NGC 3201 has been revealed to host a binary system containing a stellar-mass BH (Giesers et al. 2018), and has with recent theoretical evidence suggested the presence of a BHS (Askar et al. 2018a). In Kremer et al. (2019a), they found the number of retained BHs in NGC 3201 to be $N_{\text{BHs}} = 120^{+10}_{-10}$ in accordance with the prediction of Askar et al. (2018b) who found $N_{\text{BHs}} = 114^{+60}_{-35}$. In a subsequent paper from Giesers et al. (2019) they also find a quite high binary fraction close to the core of the cluster ($\approx 18\%$ from MUSE observations and $\approx 30\%$ from MOCCA mock observations), further highlighting the absence of an IMBH. Weatherford et al.

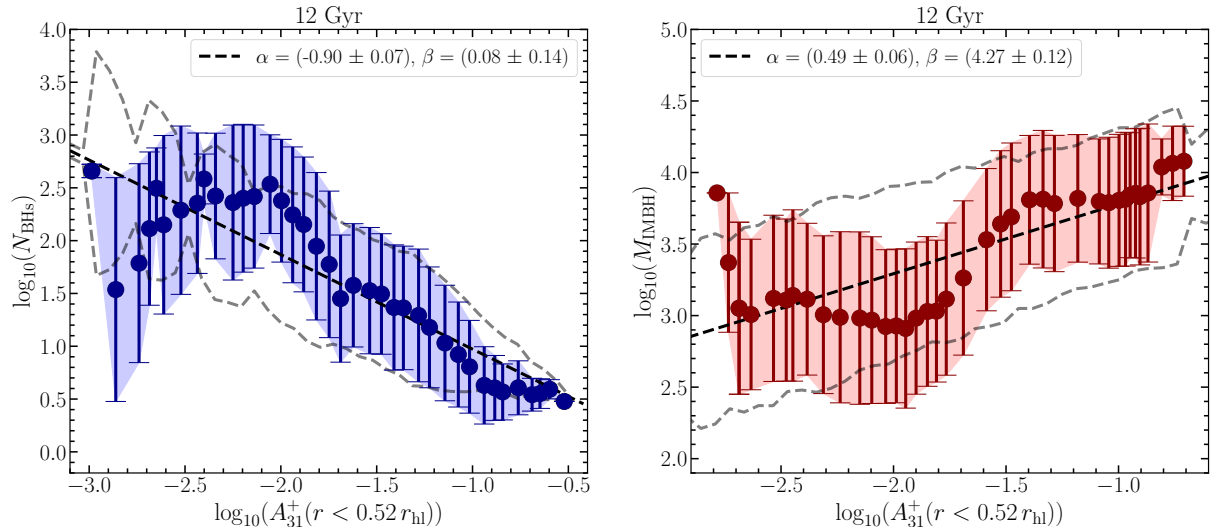


Figure 3.22: Left: the number of BHs as a function of the A^+ parameter for each model in MSD I and MSD II, right: the mass of the most massive BH in IMBH models. Two power laws have been fitted through the points, where shaded regions indicate the spread of points in the fit (the variance in each point). The errors for the best fit parameters are obtained using `numpy`'s `polyfit` package and calculate based on the given covariance matrix (c.f. Section 2.2.6). To account for scatter around the fit, a running mean has been made in 40 logarithmic bins in A_{31}^+ and the variance has been extracted inside each of these bins. The shaded areas show the combined uncertainty around each mean value for each bin while grey dashed lines indicate similar uncertainties but around the fit.

(2020) uses observed segregation as an approach for calculating the number of BHs retained, and find a lower limit of $N_{\text{BHs}} = 41_{-34}^{+40}$. By employing our relations on the number of BHs, we find the estimated number to be in better agreement with Weatherford et al. (2020) as $N_{\text{BHs}} = 64_{-45}^{+158}$, but with Askar et al. (2018b) and Kremer et al. (2019a) values contained inside our uncertainty.

3.5.3 NGC 5466

The cluster NGC 5466 is a relatively low-mass cluster of $\approx 6 \times 10^4 M_{\odot}$ with a mass to light ratio of $1.4 \pm 0.2 M_{\odot} L_{\odot}^{-1}$ (Baumgardt et al. 2020). Recent studies have revealed this cluster to show little segregation (Weatherford et al. 2020; Wu and Zhao 2021). In Askar et al. (2018a) and Weatherford et al. (2020), they find this cluster to host a substantial amount of BHs. Askar et al. (2018a), predict the number of BHs in the cluster to favour the presence of a BHS, not only from the estimated $N_{\text{BHs}} = 191_{-63}^{+110}$, but also from a total BHS mass of $M_{\text{BHS}} = 2512.2_{-703}^{+1165} M_{\odot}$. They highlight that the presence of a BHS could explain the low mass segregation found in the previous study conducted by Webb et al. (2017). There are additionally previous claims that the immense central mass could be explained by the presence of a massive IMBH (Lützgendorf et al. 2013), but was further shown possess a too small central surface brightness (Askar et al. 2018a). This is more in agreement with our results in Fig. 3.21. We find our closest cluster to have a total cluster mass of $2.9 \times 10^5 M_{\odot}$ with a central surface brightness of $\Sigma_c \approx 10^{2.0} L_{\odot} \text{pc}^{-2}$, with $A_{31}^+ = 0.0045$. The segregation value fits well with the observed value of $A_{31}^+ = 0.004$ and Baumgardt et al. (2020)'s central surface brightness, $\Sigma_c = 10^{1.93} L_{\odot} \text{pc}^{-2}$. Weatherford et al. (2020) also predict a large BH ratio in the cluster $(N_{\text{BHs}}/N_{\text{cluster}}) \times 10^5 = 41.7$. With our predictions, we find the number of BHs in the cluster to be $N_{\text{BHs}} = 173_{-122}^{+420}$, further supporting the presence of a BHS in the system.

3.5.4 NGC 6093

Another cluster hosting a substantial central surface brightness in addition to large segregation is NGC 6093, or M80. Recently, Göttgens et al. (2021) used observed spectra from MUSE to determine the clusters' central state and kinematic profiles. By applying the Jeans model (see e.g., Hénault-Brunet et al. 2019 for details over how central kinematics can help deducing global mass profiles), they obtain one solution without the need of an IMBH, while another suggests the retention of an IMBH with mass of $M_{\text{IMBH}} = 4600_{-1400}^{+1700}$. In accordance with the second solution, we find, using the IMBH mass relation in equation (3.4), an estimated IMBH mass of $M_{\text{IMBH}} = 6341_{-4220}^{+12691} M_{\odot}$. The initial half-mass relaxation time of our cluster model is ≈ 2 Gyr, but extends to around 13 Gyr at a snapshot of 12 Gyr, which in accordance with Fig. 3.9 could indicate the absence of both an IMBH and a BHS. However, we find a binary fraction inside the inner 0.05 half-light radius to be $f_b \approx 0.19$ with an initial binary fraction of 95 % (decreasing to ≈ 0.13 inside $f_b(0.8r_{\text{hl}} < r < 0.85r_{\text{hl}})$), which according to Fig. 3.18 is compatible with the possible presence of an IMBH.

3.5.5 NGC 6535

The cluster NGC 6535 has been suggested to host an IMBH candidate (Askar et al. 2017). They perform photometric mock observations using the COCOA code package (see Section. 2.2.1) to infer kinematic properties of the dark star cluster. Furthermore, they find close matches with photometric and kinematic properties with the presence of a simulated IMBH. We find the half-light radius of the closest cluster in MSD I to have a simulated half-light radius of 2.89 pc compared to Baumgardt et al. (2020) observed $r_{\text{hl}} = 2.67$ pc. From our criteria, this model seems to fit best with hosting no IMBH or a BHS. We find the number of BHs for this model to be $N_{\text{BHs}} = 23_{-16}^{+62}$. If an IMBH would be included, the fit in equation (3.4) estimates the mass, using the segregation from Weatherford et al. (2020) ($A_{31}^+ = 0.037$) to $M_{\text{IMBH}} = 3701_{-2959}^{+14744} M_{\odot}$ for NGC 6535.

3.5.6 NGC 6624

The nearest pulsar (PSR B182030A) of any known cluster is located inside NGC 6624. Recent studies indicate the presence of an IMBH with a predicted mass of $\approx 7500 M_{\odot}$ as a partner to its binary pulsar (Perera et al. 2017). More recent studies have, however, suggested that the cluster and its pulsar can be explained without the need of a central IMBH. Gieles et al. (2018) found dynamical models that properly recreate the mass functions and surface brightness of the cluster without the need of an IMBH. Askar et al. (2018b) predicts that there should be no BHS present in the system. The cluster has an observational core and half-light radius of 0.33 and 2.33 pc respectively, with a cluster mass of $1.5 \times 10^5 M_{\odot}$ and central density of $1.12 \times 10^5 M_{\odot} \text{pc}^{-3}$ (Baumgardt et al. 2020).

We find two cluster models in MSD I with properties close to those of NGC 6624. One with a simulated IMBH mass of $\approx 2100 M_{\odot}$ with a half-light radius of 4.2 pc, core radius of 0.26 pc and initial binary fraction of $f_b = 0.95$. The cluster mass is $\approx 2.7 \times 10^5 M_{\odot}$ with central density of $\approx 1.8 \times 10^4 M_{\odot} \text{pc}^{-3}$. The second cluster possess a lower initial binary fraction of $f_b = 0.1$ with a cluster mass of $\approx 3.1 \times 10^4 M_{\odot}$ and a central density at 12 Gyr of $\approx 3 \times 10^5 M_{\odot} \text{pc}^{-3}$. Interestingly, this cluster only hosts one stellar-mass BH of $3.8 M_{\odot}$ according to the simulations. By applying equation (3.4) to the closer first cluster model, we obtain an estimated BH mass of $M_{\text{IMBH}} = 6721_{-4620}^{+14784} M_{\odot}$, which stands for the cluster with largest IMBH mass and largest segregation in our models. The estimated number of BHs retained is $N_{\text{BHs}} = 7_{-4}^{+10}$. Further studies looking at the kinematics (e.g., velocity dispersion and proper motions) of the stars in the core may give further evidence about the absence or presence of an IMBH in this cluster.

Chapter 4

Discussion and conclusions

In this chapter, Section. 4.1 begins with providing a more detailed discussion to some of the results stated in chapter 3. The limitations and improvements are specified in regards to future prospects of the thesis in Section. 4.2. Finally, we conclude the thesis in the form of bullet points, providing the key takeaways of the project in Section. 4.3.

4.1 Discussion of the results

4.1.1 Observed data

The main results of this thesis are based on comparing simulated outcomes to observed data to reassure that the results we produce are reasonable for comparing with actual observations. In Fig. 3.5 we can reproduce the data for a majority of the observed clusters with models using MSD II, but with typically too small half-light radii for the IMBH models. Similarly, for the central surface brightness in Fig. 3.6, we find an overall shift towards larger values for the MSD II models. Note that segregation is based on the radial limit, $r_{\text{lim}} < 0.52r_{\text{hl}}$, meaning only stars within this radial limit are considered. While the limit is based on the observations from the ACS survey, increasing this limit yield larger segregation values in general (c.f. equation 2.5, where this would imply larger r_{max}). Throughout this work, we tested to increase the radial limit when measuring segregation and found a better match for the clusters hosting the largest segregation values using MSD II data. However, since the radial limit yields excellent matches when using MSD I data even inside this tight limit, the initial parameters of clusters seem to play a more important role in how segregated evolved clusters are compared to the exact limit used.

Furthermore, segregation data is only available for 50 observed clusters in the MW, meaning 2/3 are excluded. As observed in Fig. 3.5, unconsidered clusters have some points close to our models (uncrossed grey circles). More segregation values for the observed data would yield a better statistical significance for our predictions, with more numbers of models to compare. It is also noteworthy to point out that observed clusters vary in age (the segregation parameters are estimated for clusters with ages between 9-12 Gyr), where, in this thesis, we compare all of them to 12 Gyr snapshots. For clusters having short relaxation times, the dynamical evolution of the cluster should not change noticeably between 9-12 Gyr, although for clusters where initial relaxation times are longer, objects might still not be fully segregated at 9 Gyr in the observed clusters, but have been fully evolved in our simulations.

4.1.2 Initial concentrations

We performed (but did not show) a comparison between varying the initial concentration parameter between populations and its effect on cluster relaxation timescales and segregation. This was made by filtering clusters with different initial concentrations and plot their initial relaxation times as a function of A_{31}^+ . In particular, since a concentration of $c = 0.1$ means ten times as densely concentrated secondary populations as the first, the mass function is typically more bottom-heavy and low-mass stars in the outskirts are ejected by the tidal field. We find a slight bias that clusters in MSD II having a small concentration parameter ($c \leq 0.5$) possess long initial relaxation times, > 1 Gyr, but that they still generally cover the full range of segregation values. Models hosting concentration parameters $c > 0.5$ are almost entirely dominated by shorter relaxation times, having slightly larger segregation values.

As pointed out by Alessandrini et al. (2016), also the King concentration parameter can play a role in the dynamical evolution of GCs and have an influence on their dynamical ages. Larger values of this parameter (in their work, $W_0 = 8.0$ contrary to $W_0 = 5.0$) correlate with a faster dynamical evolution of clusters in respect to clusters with lower concentrations. In the cluster models used in this thesis, no apparent differences are seen in terms of segregation when changing this parameter. Although, cluster with initially mixed concentrations have in general slightly lower initial half-mass relaxation times and are (arguably) favourable for forming IMBHs. In accordance with the arguments in Alessandrini et al. (2016), we also claim that the dynamical evolution of BHs in the core seems to dominate the effect of varying initial concentrations in regards to how segregated an evolved cluster becomes.

4.1.3 Dynamical age as a probe for IMBHs

Another exciting finding connected to the relaxation times was stated in Section 3.4. As mentioned, it is apparent in Fig. 3.17 and 3.18 that models hosting neither an IMBH nor a BHS can retain a substantial amount of binaries close to the core and indeed be heavily segregated. This is supported in Fig. 3.9 (left panel), where indeed these models are shifted towards larger segregation values whilst they also still maintain longer relaxation times (right panel) at 12 Gyr. This sets the basis for an important conclusion. We have seen that models that do not harbour an IMBH or a BHS still can have significant mass segregation, and even models with very high relaxation times (> 10 Gyr) show equally segregated clusters as the most segregated IMBH models. Since these do not always have short relaxation times, one cannot directly claim that heavily segregated clusters are dynamically old without resolving their central properties. The relaxation times can be a good proxy for ruling out the existence of a BHS, but more information is needed to distinguish between a few BHs or the presence of an IMBH.

On the contrary, further evidence can be given from the core binary fractions. A cluster showing depletion in binaries close to the core, having a short relaxation time scale and showing extensive segregation can probe the existence of an IMBH. If the cluster instead has the same properties but retains a substantial amount of binaries close to the core, this oppositely indicates very few retained BHs in the clusters. While these signatures could help distinguish these differences, we see that the initial binary fraction in clusters is another factor to consider, as the fractions in the cores of evolved clusters can be remarkably different depending on their initial binary fraction values.

It is also important to consider other initial cluster properties that can alter the relaxation times of clusters as they evolve and hence their segregation. For instance, two models with similar initial parameters but different tidal radii can change the number of escapers in clusters over time (c.f. Fig. 3.1). Many escapers produce rapid mass loss, which means that the cluster's relaxation time decreases as the cluster evolves. It is thus worth keeping in mind that many

initial factors play a role in how the relaxation time changes through the cluster’s evolution and how it connects to the evolved cluster’s segregation.

On an observational note, as suggested in many studies, the presence of an IMBH could be inferred by observing the kinematic properties of clusters (e.g., measuring LOS velocity dispersion near the clusters centre) or searching for electromagnetic radiation from accretion processes in the vicinity of the IMBH. IMBH detection is still limited by the lack of resolution needed to distinguish such a component in the crowded cores. The main issue is that we need the most dense cores to form IMBHs, but the densest core also implies many bright components in the centre that make it difficult to resolve individual velocities of stars. Analysing kinematic properties in clusters depending on if they harbour an IMBH, a BHS, both or none of these properties would add to our list of potential observable signatures for identifying their presence (Aros et al. 2020). Thus, future prospects would involve a more careful analysis of kinematics around the cores’ of the analysed cluster models.

4.1.4 The choice of stellar populations

Quantifying mass segregation between different stellar populations requires a few essential prescriptions; firstly, a large enough sub-sample of stars in each population is needed to reduce statistic errors and limit overlap between populations and secondly, as explained in Weatherford et al. (2018), the parameter space of choice must be plausible to observe. Turn-off luminosities are utilized since these are typically easily resolved from CM diagrams of clusters. Thirdly, populations must have apparent differences in average masses (such that their effect from dynamical friction from lower mass abundant stars and relaxation yield differences in segregation). We choose the limits close to Weatherford et al. (2020) for our populations due to the availability of observed segregation data. Too dim populations are typically more challenging to observe, whilst very heavy populations, in general, are fewer in numbers.

There are, however, more options available. Alessandrini et al. (2016) quantify the effect on mass segregation using BSS since these, in general, are centrally concentrated and provide significant segregation difference to a lighter population, whilst also being bright objects that are easy to observe. We find good agreement for the simulated MOCCA models with clear signs of segregation for both MS and heavier populations following Alessandrini et al. (2016) and Weatherford et al. (2020). However, some models include too few BSS (c.f. Sec. 2.1.2.1 for BSS formation paths), and therefore segregation results can be statistically insignificant.

Despite not being presented throughout the thesis, we find similar connections using other populations and parameters; for instance, the segregation for luminous binaries increases with decreasing 50 % binary radii, which is expected. Furthermore, this is also directly correlated with the influence radius of the central BHs, where a smaller influence radius yields smaller 50 % binary radii and, thus, more heavily segregated clusters. A support image can be seen in Fig. 5.1. Since there is a direct correlation between the influence radius and the number of BHs present, heavier segregation is seen for smaller influence radii. We stress that since binary populations play an important role in the dynamical evolution of clusters and are typically well resolved in observations, the possibility of comparing segregation between more types of binary populations can be considered to further improve upon our work. For instance, millisecond pulsars have been suggested to connect well to BH dynamics in clusters (Claire et al. 2019) and could be an interesting population to consider.

4.1.5 Comparing predictions between A^+ and Δ_{r50}

The Δ_{r50} and A_{31}^+ parameters depicted in Fig. 3.8 show similar relations in predicting BH ratios, with the Δ_{r50} parameter showing a slightly shallower slope for the number of BHs retained, suggesting that in general, there exists more models with very small segregation values ($\Delta_{r50}^{13} < 0.0025$). A shallower slope generally induces a smaller predicted number of BHs, implying larger predicted BH masses. Throughout the testing in our models, we found the A^+ parameter to be more robust, yielding fewer non-valid values (negative segregation).

Physically, negative segregation parameters are produced when the reference lighter population is more segregated than the heavier. We do not find any correlation in initial parameters for “reversely” segregated models, except that the majority have a smaller initial tidal radius ($r_t = 60$ pc as opposed to $r_t = 120$ pc). The more rapid mass loss and increased number of escaped light stars together with the dynamical heating of BHs can cause too large mixing between populations for the evidence of mass segregation. We stress that the segregation results seen in this thesis do not include negatives, but reversely segregated clusters were present in our results. Such discrepancies could be avoided by fine-tuning the turnoff luminosities and, therefore, average masses of the populations considered. Since our models still include a large sub-sample of values, we do not take any actions to avoid these.

A more interesting prospect is seeing how the two segregation parameters vary in the predicted number of BHs and IMBH masses. Using both MSD I and MSD II data, the relations for predicting these quantities as a function of the Δ_{r50} parameters are stated in equations (4.1) and (4.2). By performing the same procedures as for equations (3.3) and (3.4), but exchanging for the Δ_{r50} , we find similar, but slightly different fits

$$\log_{10}(N_{\text{BHs}}) = (-0.88 \pm 0.07) \log_{10}(\Delta_{r50}^{13}) - (0.11 \pm 0.12) \quad (4.1)$$

$$\log_{10}(M_{\text{IMBH}}) = (0.55 \pm 0.05) \log_{10}(\Delta_{r50}^{13}) + (4.35 \pm 0.08). \quad (4.2)$$

Predictions based on the Δ_{r50} with included uncertainties is stated in Table 5.1, together with some general properties of the clusters. We assume the same clusters to harbour potential IMBH candidates as in Table 3.1. Figure 4.1 shows the difference between BH predictions for the two segregation parameters, using the heaviest and lightest MS populations as a comparison to the numbers derived by Weatherford et al. (2020). Besides (generally) larger predicted numbers for the A_{31}^+ parameter, larger uncertainties are observed for Δ_{r50} . In particular for NGC 5466. This cluster has an extremely small segregation parameter, and as stated in Section 3.5.3, previous works have suggested the retention of many BHs in this system. Despite that our predicted value using the Δ_{r50} indicate the presence of a BHS, the uncertainties are too significant to make the predicted number reliable.

Due to the anti-correlation between the number of BHs and higher segregation values, the predicted BH masses for the Δ_{r50} parameter instead (slightly) over predicts IMBH masses compared to the A_{31}^+ , but with better overlap between the two parameters. Fig. 4.2 displays one outlier however, NGC 6093. The discrepancy becomes apparent when comparing Table 3.1 and Table 5.1. The segregation value in the latter table is almost an order of magnitude smaller for this cluster. Since our fit indicates that segregation increases with increasing IMBH masses, the low segregation values will under predict the IMBH mass compared to the A_{31}^+ parameter. The large standard deviations come partly from the large uncertainty in the measured Δ_{r50} parameter but also from the fitting errors for low segregation values. Note however, that the scatter in data around the fit is very large and that the fit is idealized for the cluster models. Clusters might deviate by an order of magnitude compared to the fit due to the large scatter. Real observed clusters also vary in ages and initial parameters compared to models, which further can increase the uncertainties of our fits.

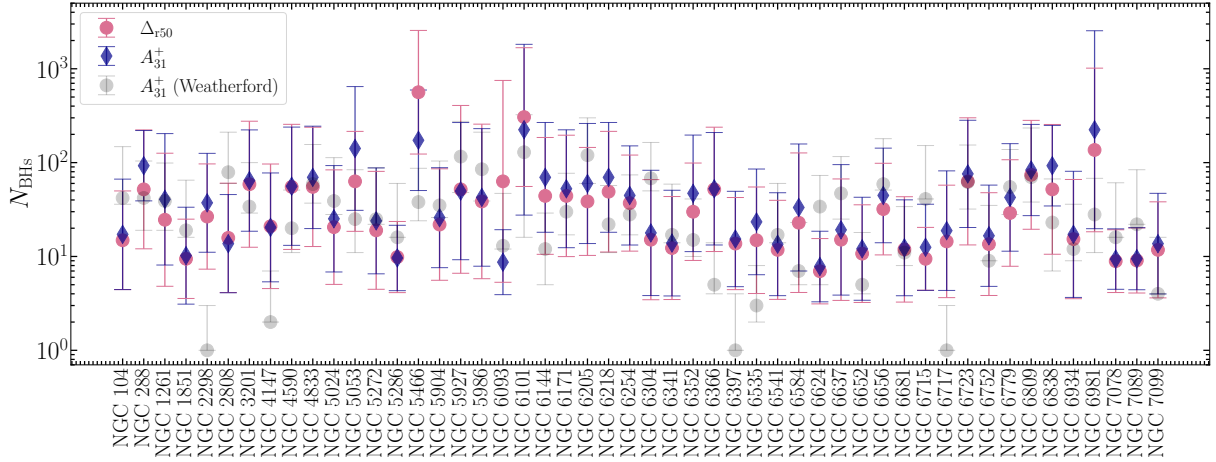


Figure 4.1: The predicted number of BHs from the relations found in equation (3.3) based on the observed segregation parameters (Tables. 3.1 and 5.1) for 50 MW GCs. The errorbars indicate the minimum and maximum predictions based on the uncertainty of the fits and the segregation parameters. The predictions are compared between the Δ_{r50} and A^+ parameters in pink and dark blue respectively, using the MS populations `pop3` and `pop1`. For reference, the predictions based on A_{31}^+ from Weatherford et al. (2020) is included in black shaded circles.

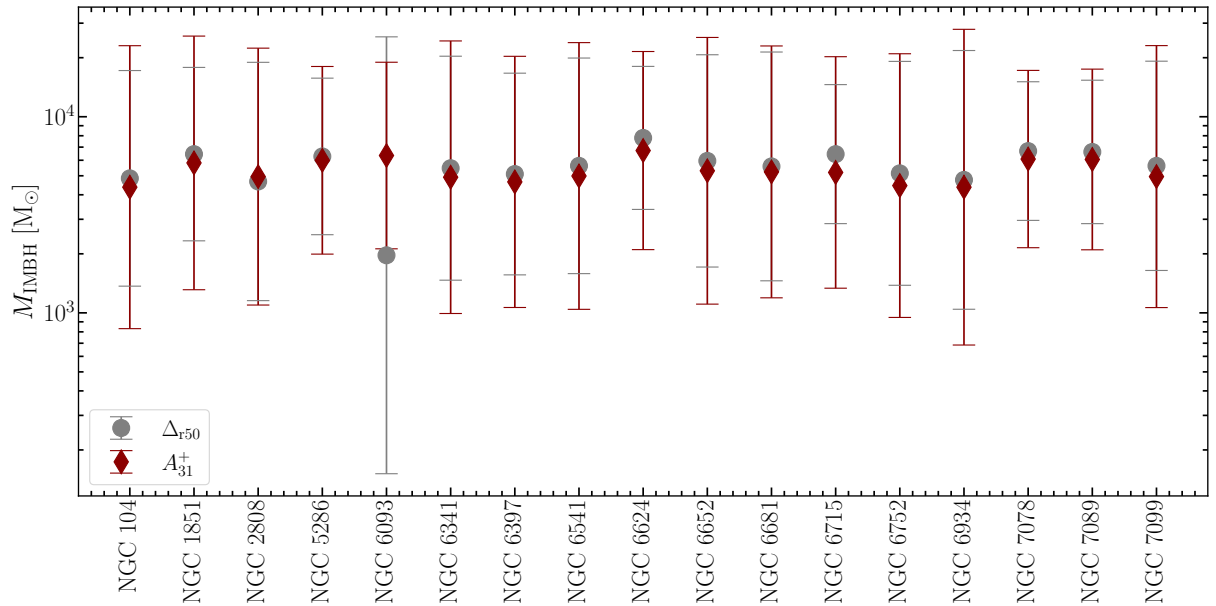


Figure 4.2: Analogous to Fig. 4.1 but instead displaying the predicted IMBH masses for clusters possessing a mass segregation value $A_{31}^+ \gtrsim 0.05$.

We stress that the simulated number of BHs and IMBH masses are strongly dependent on the natal kicks received at birth, the fallback mass onto the BHs and the formation paths of IMBHs. In particular, the natal kicks of BHs in real GCs are still strongly debated, with many up-to-date works finding various results (e.g., Belczynski et al. 2002; Pavluk et al. 2018; Atri et al. 2019). The current MOCCA code incorporates fallback prescriptions that produce very massive stellar-mass BHs and MSD II models retained a higher fraction of these BHs following their formation. This could be an explanation for the higher number of BHs predicted in this thesis as compared to other works (Askar et al. 2018a; Weatherford et al. 2020).

Furthermore, our predictions are based on the relations between the simulated number of BHs, BH masses and the observed segregation parameters. Although we do find values quite similar to previous works, the scatter around the power-law fits is still significant. For our predictions, other methods could have been used and compared; for instance, Askar et al. (2018a) predicts densities of BHS in Galactic GCs using observed $\log(L_v/r_{\text{hl}}^2)$ in MSD I and infer the numbers of BH from the gathered relation. A comparison with more variations of observed parameters could increase the statistical value of our predictions. Also note our arbitrarily chosen limit for which clusters' IMBH masses are predicted, in particular, for clusters having $A_{31}^+ \gtrsim 0.05$. While this choice is based on the segregation value in Fig. 3.21 beyond which most models containing IMBHs are present, we stress that a change of this limit would indeed change the number of models in our predictions that become candidates for hosting an IMBH.

4.2 Uncertainties and future prospects

4.2.1 The MOCCA Code

As described in Section. 2.1, the MOCCA code can simulate dynamical properties of clusters close to modern N-body codes by using a Monte Carlo treatment for the cluster evolution. Direct N-body methods calculate the gravitational interactions between any number of bodies in a chosen time step, which means that the resolution for following individual components and dynamical interactions between multiple stars becomes more accurate.

For this thesis, resolving the overall dynamical evolution in clusters is of higher importance than having extremely high precision between every multiple body interaction in hierarchical systems. However, we stress that such assumptions can indeed change the overall dynamical state of clusters. The Monte Carlo approach means that free parameters are of need, which are naturally covered in N-body codes, e.g., relaxation processes, interactions with distant objects and escapers in static tidal fields. The method assumes complete spherical symmetry, non-rotational clusters (rotational properties on GCs can accelerate core collapses and mass segregation) and the lack of higher-order multiples, which can play a role in the dynamical evolution of the cluster's core. Although these shortcomings do not strongly influence our work, keeping these assumptions in mind is important. MOCCA generally agrees in global properties compared to direct N-body codes (Giersz et al. 2013), and despite the MSD II not being produced to accurately represent real GCs, their characteristics are still impressively similar (Hypki et al. in prep.). Since the evolution of real GCs depends on a number of different processes, the need for assumptions and approximate prescriptions for the treatment of those processes is always necessary.

4.2.2 Dynamical formation of CVs and BBH

We studied but did not show the dynamical formation and semi-major axes of BBH and NS-MS at 10 Gyr for the clusters indicated in Fig. 3.10. The results indicate a higher fraction of dynamically formed binaries in the dense (initial core density of $\approx 2.4 \times 10^8 M_{\odot} \text{pc}^{-3}$) and dynamically older cluster that distribute closer to the cluster's core. Furthermore, these NS-MS binaries have in general lower semi-major axis distributions. From studying the distribution of exotica, this further indicates the connection between dynamically older clusters and more heavily segregated populations.

In terms of CV sources, it is important to stress that their detection are limited in GCs. Big surveys such as the Sloan Digital Sky Survey have successfully observed at deep magnitudes sufficient for detecting CV sources. However, in crowded environments like GCs, observations are still limited. Updated techniques for resolving these include $H\alpha$ imaging - CV sources typically have an excess in $H\alpha$ - but still, even deeper observations have to be made to detect

the dimmest populations of CVs. Finding a strong correlation between the relaxations times and dynamical formation of CVs can aid in constraining what kinds of clusters to look for when searching for CVs. However, we would need to extend our work to give clear signatures in the kinematic properties of cluster’s cores, to constrain their presence. Such an approach could involve detailed analyses of central velocity dispersion’s, since large dynamical interactions in GCs are needed for their formation (Belloni et al. 2016).

4.2.3 Observed data

As pointed out in Weatherford et al. (2020), the measured mass segregation is dependent on the radial limit of which stars are available in the survey. Furthermore, the ACS survey, which is used, has observations with a fixed angular size and the data consequentially relates to the heliocentric distance to the clusters. The limitations in radial limits from observations can also lead to biases, as the full range of stars is not resolvable. Clusters could also include outliers in the MS and heavier populations (deviating far from the bulk stars on the CM diagrams), leading to a bias in the segregation, however, these are indeed corrected for completeness (for details, see sec. 4.3 in Weatherford et al. 2018). To find similarities between our simulated clusters with observed ones, we find close matching pairs using mainly the central surface brightness and checking similarities in half-light radius, cluster mass and core radius.

4.2.3.1 47 Tuc

As pointed out in, e.g., Section. 3.5.1, it is hard to find models that match in each of these prospects. For instance, the core- and half-light radius for 47 Tuc was challenging to find in our models. In this case, our half-light radius was about 1.3 pc larger than the observed one which typically generates smaller segregation values, but we still over predict the IMBH mass compared to, e.g., Ye et al. (2021). Despite 47 Tuc being one of the most analysed clusters in the MW observationally, there still exists uncertainties in e.g, the mass-to-light ratios close to the core ($\approx \pm 0.1 M_{\odot} L_{\odot}^{-1}$) and potential signs of rotation (Baumgardt et al. 2020). We do, however, support the claim of the presence of an IMBH here since we do see a large binary fraction of 17 % in the innermost 0.05 pc and with an initially binary fraction 0.95 (c.f. Fig. 3.18).

4.2.3.2 NGC 3201

NGC 3201 also possesses large uncertainties inside the innermost 20 arc seconds in its mass-to-light ratio, further indicating strong dynamical activity. Our values are still overpredicted, however, compared to Weatherford et al. (2020) despite them also using the segregation as an estimate for the BH retention. Their method is based on generating a KDE over the observed Δ (both Δ_{r50} and A^+), using the same radial limits as in this work. From that point, random samples of Δ are drawn from a normal distribution and BH number fractions are sampled, assuming mass-to-light ratios of $M/L = 2$. We simply use power-law fits to the simulated data for our estimations (however, we find our values to agree very well with the other works; Askar et al. 2018a; Kremer et al. 2019a). Another possible explanation for the difference in the inferred N_{BHs} compared to Weatherford et al. (2020) could be the tuning of the BH fallback, which sets the number of retained BHs in simulated clusters. We stress that despite that both our and Weatherford et al. (2020)’s work use the same segregation parameters for our predictions, the differences in methods can really bias the final outcomes.

4.2.3.3 NGC 6535

NGC 6535 is further interesting to discuss since it has been suggested to host an IMBH while still maintaining relatively low segregation and central surface brightness values. In MSD I, we find a particular IMBH model close to its central surface brightness and segregation values. For the close IMBH model, we find a large binary fraction in the core of $\approx 35\%$ for the innermost 0.05 pc. Another close model with similar segregation and surface brightness does not harbour an IMBH and also possesses a large core binary fraction of 25%. The initial binary fractions were 0.3 and 0.95, respectively, in these cases. From our models, it is still uncertain whether the cluster hosts an IMBH or very few BHs and would be a promising candidate to further explore in future works.

4.2.4 Future prospects and improvements

We have performed a quantitative analysis of how mass segregation and distributions of various stellar populations affect GCs observational signatures. When investigating distinct cluster models (Table 2.3 and Table 2.4), we limit ourselves to clusters with similar initial parameters. The results are generally biased towards pin-pointing clusters with initial parameters that show substantial differences in the investigated parameters. Despite also conducting analyses for all models in MSD I and MSD II, to diagnose how observational signatures depend on the initial state of clusters, one could be more careful and fully distinguish between clusters with similar initial masses, densities, and binary fractions. Note also that cluster models are set to be on circular orbits in their tidal fields around the Galaxy. Clusters on eccentric orbits could indeed have varying mass losses throughout their orbits, leading to more evaporation of stars that could alter relaxation times.

Furthermore, we limit ourselves to the method presented in Weatherford et al. (2020) for measuring mass segregation, but as pointed out in, e.g., Wu and Zhao (2021), there exist several additional methods to quantify this. According to Paust et al. (2010), one can use the stellar mass function slopes as a proxy for the segregation in clusters, where usually, mass functions are steeper in more evolved and segregated clusters. This would involve finding the stellar mass functions in the MSD outputs and connect it to the clusters dynamical age (Sollima and Baumgardt 2017).

Another way to measure the segregation parameter in clusters is to analyse how close an evolved cluster is to being in equipartition ($\sigma \sim m^{-\eta}$, where $\eta = 0.5$ for equipartition), thus how the velocity dispersion scales with stellar mass (Trenti and Marel 2013). According to the authors, the presence of an IMBH can quench mass segregation¹ and decrease η . Performing this in our work would involve selecting populations with varying masses and analysing the slope in the $\sigma - m$ plane. Since this is correlated to the mass function slopes for the populations, this yields biases in the excess or depletion of low-mass stars. A steeper IMF provides more energy for light stars and more substantial segregation.

Trenti and Marel (2013) perform direct N-body methods and find that a central IMBH quenches segregation. In this work, we claim that the presence of a central IMBH instead enhances the segregation. In the work conducted by Trenti and Marel (2013), stellar and binary evolution was not implemented, meaning that the dynamics connected to, e.g., mass loss processes were excluded. However, a massive central IMBH can cause a rapid mass loss in clusters due to evaporation, leading to substantial segregation. A future implementation would be to check whether our cluster models still evolve to be more heavily segregated in the presence of IMBHs when measuring the segregation based on equipartition.

¹however, as pointed out by Wu and Zhao 2021, this quenching could also be generated by a substantial amount of stellar-mass BHs in the core, similar to what we predict

Future improvements would involve a more careful analysis of the total mass of BHs in GCs. Whilst we find apparent differences in the segregation between IMBH models and BHS models regarding dynamical ages, binary fractions and central surface brightness, we made no claims about the total masses of the central systems. As pointed out in, e.g., Wu and Zhao (2021), quenching of mass segregation can be found both for a large central system of stellar-mass BHs with a large total mass and for IMBH models. In many cases, since we cannot resolve deep into the cores of GCs, there is uncertainty about whether the majority of mass comes from a single massive BH or many smaller BHs. In particular, if the fraction of the IMBH-to-cluster mass is substantial, the large influence radius could quench segregation.

As pointed out in Askar et al. (2017), MSD I simulations have shown some clusters where IMBH masses can stand for up to 50 % of the total cluster mass. In the MSD II data, the median IMBH- to cluster mass ratio is 0.18 %, while a larger 4 % for MSD I, which suggests that IMBH are not massive enough (in terms of the cluster mass) to quench mass segregation significantly. This also means that IMBH masses above $10^3 - 10^4 M_{\odot}$, at least in the MSD II, are rare. Similar claims have been shown by, e.g., Baumgardt et al. (2020), which suggests that the central surface brightness and kinematic profiles in observed GCs predict the presence of IMBHs with masses above $10^4 M_{\odot}$ to be rare.

Finally, analysing the kinematic properties in clusters in the presence of a BHS or an IMBH would be a future step to signatures their central states. In this work, we determine signatures using photometric measurements of the distributions of stars. By combining these methods, further constraints can be put on the central properties of GCs.

4.3 Conclusions

Recent theoretical and observational studies have indicated evidence for stellar-mass BH candidates retained in GCs, while some predict the existence of IMBHs in their cores. This study has analyzed how the retention of numerous stellar-mass BHs or an IMBH influence the distribution and properties of observable stellar populations in simulated GCs using MSD I and II. In summary, we analyze how the central state determines mass segregation between main-sequence, giant and BSS populations; how binaries distribute and deplete depending on the number of BHs retained; the connection between the dynamical age of clusters and the presence of CVs; and finally give predictions over numbers and masses of BHs and IMBHs in observed MW GCs. The findings in this thesis can be summarized as follows:

- Following previous studies (e.g., Askar et al. 2018a; Kremer et al. 2019a), we confirm that clusters with initially larger half-mass radii evolve towards a more sparse morphology, typically retaining a larger sample of BHs, which excites lighter stars via dynamical heating. As expected, these clusters host, in general, larger half-light radii, have lower central surface brightness and central densities. Segregation between different populations is more strongly seen in IMBH models compared to BHS models.
- The mass segregation in this thesis is quantified using the relative cumulative radial distributions between stellar populations. Dynamically old clusters are generally more segregated than dynamically young clusters since clusters with shorter relaxation times typically retain fewer BHs. Furthermore, the densest models with large IMBHs dominate in the regime of mass segregation and have, in general, central surface brightness values $> 10^4 L_{\odot} \text{pc}^{-2}$. The initial concentration of populations seems to have a negligible effect on mass segregation compared to the energy provided by BHs.
- Heavy populations, such as BSS and binaries are good indicators for probing dynamical ages and segregation in clusters. We find that clusters with shorter relaxation times have an increased formation rate of BSS and that these are typically heavily segregated in clusters with dense cores. However, some clusters show signs of BSS bimodality, and have an excess of BSS also in the cluster's outskirts. We also find that clusters harbouring IMBHs deplete their core binary fractions compared to models hosting many BHs.
- Dynamically older clusters retain a higher fraction of low semi-major axis binaries and form more exotic objects dynamically, such as WD-MS and NS-MS binaries. However, the initial binary fraction and semi-major axes of binaries alter their survival rates in clusters. Models with lower initial binary fraction begin with initially tighter orbits than models with high initial binary fractions. We conclude that such models tend to retain more binaries closer to the core, but higher initial binary fractions are needed to reproduce the binary fractions outside cluster's half-light radius, in particular for models harbouring a BHS.
- We predict the number of retained BHs in 50 observed GCs based on their segregation in addition to potential masses of IMBHs in 17 clusters with substantial segregation values. Good agreements are found between our predicted number of BHs with other recent works in NGC 3201 (with $N_{\text{BHs}} = 64_{-45}^{+158}$), the support of a BHS in NGC 5466 ($N_{\text{BHs}} = 173_{-122}^{+420}$) and an IMBH candidate in NGC 6535 ($M_{\text{IMBH}} = 3701_{-2959}^{+14744} M_{\odot}$). We find an overestimate in IMBH masses for 47 Tuc and NGC 6624 compared to previous works. Our approach predicts a higher number of retained BHs in observed cluster compared to previous studies. This may be due to the updated treatment for the evolution of BH progenitors in the MOCCA code which results in a higher fraction of retained BHs.

- The work concludes that the clusters dynamical state strongly indicates present-day presence of a BHS or an IMBH. Short relaxation times suggest the presence of an IMBH if the model displays prominent segregation, but similar segregation values are achieved in clusters where there is an absence of a BHS and an IMBH. We claim that such clusters tend to retain a higher binary fraction in the core as compared to the models that have an IMBH in their centre. We show that this result depends on the clusters' initial binary fractions. We also find that relaxation times and mass segregation are sufficient for ruling out the existence of a BHS, but additional information about core binary fractions and central surface brightness is needed to more appropriately resolve the central states of GCs. To resolve these challenges, a proper kinematic analysis of clusters harbouring either a BHS or an IMBH could give further insights into helping determine their presence at the centre of GCs.

Bibliography

- Abbott, Richard et al. (2020). “Gw190521: A binary black hole merger with a total mass of 150 M_{\odot} ”. *Physical review letters* 125.10, p. 101102.
- Alessandrini, Emiliano, Barbara Lanzoni, Francesco R Ferraro, Paolo Miocchi, and Enrico Vesperini (2016). “Investigating the mass segregation process in globular clusters with blue straggler stars: the impact of dark remnants”. *The Astrophysical Journal* 833.2, p. 252.
- Arca Sedda, Manuel, Abbas Askar, and Mirek Giersz (2018). “MOCCA-Survey Database–I. Unravelling black hole subsystems in globular clusters”. *Monthly Notices of the Royal Astronomical Society* 479.4, pp. 4652–4664.
- Aros, Francisco I, Anna C Sippel, Alessandra Mastrobuono-Battisti, Paolo Bianchini, Abbas Askar, and Glenn Van De Ven (2021). “Using binaries in globular clusters to catch sight of intermediate-mass black holes”. *Monthly Notices of the Royal Astronomical Society* 508.3, pp. 4385–4398.
- Aros, Francisco I., Anna C. Sippel, Alessandra Mastrobuono-Battisti, Abbas Askar, Paolo Bianchini, and Glenn van de Ven (Dec. 2020). “Dynamical modelling of globular clusters: challenges for the robust determination of IMBH candidates”. *MNRAS* 499.4, pp. 4646–4665.
- Askar, Abbas, Manuel Arca Sedda, and Mirek Giersz (2018a). “MOCCA-SURVEY Database I: Galactic globular clusters harbouring a black hole subsystem”. *Monthly Notices of the Royal Astronomical Society* 478.2, pp. 1844–1854.
- (Aug. 2018b). “MOCCA-SURVEY Database I: Galactic globular clusters harbouring a black hole subsystem”. *MNRAS* 478.2, pp. 1844–1854.
- Askar, Abbas, Mirek Giersz, Wojciech Pych, and Emanuele Dalessandro (2018c). “COCOA code for creating mock observations of star cluster models”. *Monthly Notices of the Royal Astronomical Society* 475.3, pp. 4170–4185.
- Askar, Abbas, Mirek Giersz, Manuel Arca Sedda, Ammar Askar, Mario Pasquato, and Agostino Leveque (2019a). “Stellar-mass Black Holes in Globular Clusters: Dynamical consequences and observational signatures”. *Proceedings of the International Astronomical Union* 14.S351, pp. 395–399.
- Askar, Abbas, Magdalena Szkudlarek, Dorota Gondek-Rosińska, Mirek Giersz, and Tomasz Bulik (2017). “MOCCA-SURVEY Database–I. Coalescing binary black holes originating from globular clusters”. *Monthly Notices of the Royal Astronomical Society: Letters* 464.1, pp. L36–L40.
- Askar, Ammar, Abbas Askar, Mario Pasquato, and Mirek Giersz (2019b). “Finding black holes with black boxes—using machine learning to identify globular clusters with black hole subsystems”. *Monthly Notices of the Royal Astronomical Society* 485.4, pp. 5345–5362.
- Atri, P et al. (2019). “Potential kick velocity distribution of black hole X-ray binaries and implications for natal kicks”. *Monthly Notices of the Royal Astronomical Society* 489.3, pp. 3116–3134.
- Bahramian, Arash et al. (2017). “The ultracompact nature of the black hole candidate X-ray binary 47 Tuc X9”. *Monthly Notices of the Royal Astronomical Society* 467.2, pp. 2199–2216.

- Baumgardt, H, A Sollima, and M Hilker (2020). “Absolute-band magnitudes and mass-to-light ratios of Galactic globular clusters”. *Publications of the Astronomical Society of Australia* 37.
- Belczynski, K et al. (2016). “The effect of pair-instability mass loss on black-hole mergers”. *Astronomy & Astrophysics* 594, A97.
- Belczynski, Krzysztof, Tomasz Bulik, Chris L Fryer, Ashley Ruiter, Francesca Valsecchi, Jorick S Vink, and Jarrod R Hurley (2010). “On the maximum mass of stellar black holes”. *The Astrophysical Journal* 714.2, p. 1217.
- Belczynski, Krzysztof, Vassiliki Kalogera, and Tomasz Bulik (2002). “A comprehensive study of binary compact objects as gravitational wave sources: evolutionary channels, rates, and physical properties”. *The Astrophysical Journal* 572.1, p. 407.
- Belloni, Diogo, Abbas Askar, Mirek Giersz, Pavel Kroupa, and Helio J Rocha-Pinto (2017). “On the initial binary population for star cluster simulations”. *Monthly Notices of the Royal Astronomical Society* 471.3, pp. 2812–2828.
- Belloni, Diogo, Mirek Giersz, Abbas Askar, Nathan Leigh, and Arkadiusz Hypki (2016). “MOCCA-SURVEY database I. Accreting white dwarf binary systems in globular clusters–I. Cataclysmic variables–present-day population”. *Monthly Notices of the Royal Astronomical Society* 462.3, pp. 2950–2969.
- Belloni, Diogo, Mirek Giersz, Liliana E Rivera Sandoval, Abbas Askar, and Paweł Ciecielag (2019). “MOCCA-SURVEY database I. Accreting white dwarf binary systems in globular clusters–IV. Cataclysmic variables–properties of bright and faint populations”. *Monthly Notices of the Royal Astronomical Society* 483.1, pp. 315–331.
- Benacquista, Matthew J and Jonathan MB Downing (2013). “Relativistic binaries in globular clusters”. *Living reviews in relativity* 16.1, pp. 1–99.
- Binney, James and Scott Tremaine (2011). *Galactic dynamics*. Princeton university press.
- Breen, Philip G and Douglas C Heggie (2013). “Dynamical evolution of black hole subsystems in idealized star clusters”. *Monthly Notices of the Royal Astronomical Society* 432.4, pp. 2779–2797.
- Chaisson, Eric, Stephen McMillan, and Emily Rice (2008). *Astronomy today*. Pearson/Addison Wesley San Francisco, CA.
- Chatterjee, Sourav, Stefan Umbreit, John M Fregeau, and Frederic A Rasio (2013). “Understanding the dynamical state of globular clusters: core-collapsed versus non-core-collapsed”. *Monthly Notices of the Royal Astronomical Society* 429.4, pp. 2881–2893.
- Claire, S Ye, Kyle Kremer, Sourav Chatterjee, Carl L Rodriguez, and Frederic A Rasio (2019). “Millisecond Pulsars and Black Holes in Globular Clusters”. *The Astrophysical Journal* 877.2, p. 122.
- Davies, Melvyn B (2013). “Globular Cluster Dynamical Evolution”. *Planets, Stars and Stellar Systems. Volume 5: Galactic Structure and Stellar Populations* 5, p. 879.
- De Rijcke, Sven, Pieter Buyle, and Herwig Dejonghe (2006). “Upper limits on the central black hole masses of 47 Tuc and NGC 6397 from radio continuum emission”. *Monthly Notices of the Royal Astronomical Society: Letters* 368.1, pp. L43–L46.
- Di Carlo, Ugo N. et al. (Nov. 2021). “Intermediate-mass black holes from stellar mergers in young star clusters”. *MNRAS* 507.4, pp. 5132–5143.
- Ferraro, FR et al. (2012). “Dynamical age differences among coeval star clusters as revealed by blue stragglers”. *Nature* 492.7429, pp. 393–395.
- Fregeau, John M, P Cheung, SF Portegies Zwart, and FA Rasio (2004). “Stellar collisions during binary–binary and binary–single star interactions”. *Monthly Notices of the Royal Astronomical Society* 352.1, pp. 1–19.

- Fryer, Chris L, Krzysztof Belczynski, Grzegorz Wiktorowicz, Michal Dominik, Vicky Kalogera, and Daniel E Holz (2012). “Compact remnant mass function: dependence on the explosion mechanism and metallicity”. *The Astrophysical Journal* 749.1, p. 91.
- Gieles, Mark (2012). “Mass loss of stars in star clusters: an energy source for dynamical evolution”. *arXiv preprint arXiv:1209.2071*.
- Gieles, Mark, Eduardo Balbinot, Rashid ISM Yaaqib, Vincent Hénault-Brunet, Alice Zocchi, Miklos Peuten, and Peter G Jonker (2018). “Mass models of NGC 6624 without an intermediate-mass black hole”. *Monthly Notices of the Royal Astronomical Society* 473.4, pp. 4832–4839.
- Giersz, M., A. Askar, L. Wang, A. Hypki, A. Leveque, and R. Spurzem (Aug. 2019). “MOCCA survey data base- I. Dissolution of tidally filling star clusters harbouring black hole subsystems”. *MNRAS* 487.2, pp. 2412–2423.
- Giersz, Mirek (1998). “Monte Carlo simulations of star clusters—I. First results”. *Monthly Notices of the Royal Astronomical Society* 298.4, pp. 1239–1248.
- (2001). “Monte Carlo simulations of star clusters—II. Tidally limited, multimass systems with stellar evolution”. *Monthly Notices of the Royal Astronomical Society* 324.1, pp. 218–230.
- (2006). “Monte Carlo simulations of star clusters—III. A million-body star cluster”. *Monthly Notices of the Royal Astronomical Society* 371.1, pp. 484–494.
- Giersz, Mirek, Douglas C Heggie, and Jarrod R Hurley (2008). “Monte Carlo simulations of star clusters—IV. Calibration of the Monte Carlo code and comparison with observations for the open cluster M67”. *Monthly Notices of the Royal Astronomical Society* 388.1, pp. 429–443.
- Giersz, Mirek, Douglas C Heggie, Jarrod R Hurley, and Arkadiusz Hypki (2013). “MOCCA code for star cluster simulations—II. Comparison with N-body simulations”. *Monthly Notices of the Royal Astronomical Society* 431.3, pp. 2184–2199.
- Giersz, Mirek, Nathan Leigh, Arkadiusz Hypki, Nora Lützgendorf, and Abbas Askar (2015). “MOCCA code for star cluster simulations—IV. A new scenario for intermediate mass black hole formation in globular clusters”. *Monthly Notices of the Royal Astronomical Society* 454.3, pp. 3150–3165.
- Giesers, Benjamin et al. (2018). “A detached stellar-mass black hole candidate in the globular cluster NGC 3201”. *Monthly Notices of the Royal Astronomical Society: Letters* 475.1, pp. L15–L19.
- Giesers, Benjamin et al. (2019). “A stellar census in globular clusters with MUSE: Binaries in NGC 3201”. *Astronomy & Astrophysics* 632, A3.
- Göttgens, Fabian et al. (2021). “Central kinematics of the Galactic globular cluster M80”. *Monthly Notices of the Royal Astronomical Society* 507.4, pp. 4788–4803.
- Grindlay, Jonathan E, Craig Heinke, Peter D Edmonds, and Stephen S Murray (2001). “High-resolution x-ray imaging of a globular cluster core: Compact binaries in 47Tuc”. *Science* 292.5525, pp. 2290–2295.
- Harris, William E (1996). “A catalog of parameters for globular clusters in the Milky Way”. *The Astronomical Journal* 112, p. 1487.
- (2010). “A new catalog of globular clusters in the Milky Way”. *arXiv preprint arXiv:1012.3224*.
- Harris, William E, Gretchen LH Harris, and Matthew Alessi (2013). “A Catalog of Globular Cluster Systems: What Determines the Size of a Galaxy’s Globular Cluster Population?” *The Astrophysical Journal* 772.2, p. 82.
- Heggie, Douglas C (1975). “Binary evolution in stellar dynamics”. *Monthly Notices of the Royal Astronomical Society* 173.3, pp. 729–787.
- Hénault-Brunet, Vincent, Mark Gieles, Antonio Sollima, Laura L Watkins, Alice Zocchi, Ian Claydon, ELENA Pancino, and Holger Baumgardt (2019). “Mass modelling globular clusters in the Gaia era: a method comparison using mock data from an N-body simulation of M 4”. *Monthly Notices of the Royal Astronomical Society* 483.1, pp. 1400–1425.

- Hénon, M (1971). “Monte Carlo models of star clusters”. *Astrophysics and Space Science* 13.2, pp. 284–299.
- Hobbs, George, DR Lorimer, AG Lyne, and M Kramer (2005). “A statistical study of 233 pulsar proper motions”. *Monthly Notices of the Royal Astronomical Society* 360.3, pp. 974–992.
- Hurley, Jarrod R, Christopher A Tout, and Onno R Pols (2002). “Evolution of binary stars and the effect of tides on binary populations”. *Monthly Notices of the Royal Astronomical Society* 329.4, pp. 897–928.
- Hypki, Arkadiusz and Mirek Giersz (2013). “mocca code for star cluster simulations–I. Blue stragglers, first results”. *Monthly Notices of the Royal Astronomical Society* 429.2, pp. 1221–1243.
- (2017). “MOCCA code for star cluster simulations–VI. Bimodal spatial distribution of blue stragglers”. *Monthly Notices of the Royal Astronomical Society* 471.3, pp. 2537–2552.
- Janka, Hans-Thomas (Sept. 2013). “Natal kicks of stellar mass black holes by asymmetric mass ejection in fallback supernovae”. *MNRAS* 434.2, pp. 1355–1361.
- Kamlah, AWH et al. (2021). “Preparing the next gravitational million-body simulations: Evolution of single and binary stars in Nbody6++ GPU, MOCCA and McLuster”. *arXiv preprint arXiv:2105.08067*.
- Karttunen, Hannu, Pekka Kröger, Heikki Oja, Markku Poutanen, and Karl J. Donner (2003). *Fundamental astronomy*. 5th ed. Springer.
- King, Ivan R. (Feb. 1966). “The structure of star clusters. III. Some simple dynamical models”. *AJ* 71, p. 64. DOI: [10.1086/109857](https://doi.org/10.1086/109857).
- Kissler, Markus (2019a). URL: http://ned.ipac.caltech.edu/level5/Sept13/Kissler/Kissler_contents.html.
- (Aug. 2019b). *KINEMATICS OF GLOBULAR CLUSTERS*. URL: <https://ned.ipac.caltech.edu/level5/Sept13/Kissler/Kissler6.html>.
- Kızıltan, Bülent, Holger Baumgardt, and Abraham Loeb (2017). “An intermediate-mass black hole in the centre of the globular cluster 47 Tucanae”. *Nature* 542.7640, pp. 203–205.
- Kremer, Kyle, Sourav Chatterjee, S Ye Claire, Carl L Rodriguez, and Frederic A Rasio (2019a). “How initial size governs core collapse in globular clusters”. *The Astrophysical Journal* 871.1, p. 38.
- Kremer, Kyle, S Ye Claire, Sourav Chatterjee, Carl L Rodriguez, and Frederic A Rasio (2019b). “The Role of “black hole burning” in the evolution of dense star clusters”. *Proceedings of the International Astronomical Union* 14.S351, pp. 357–366.
- Kremer, Kyle, S Ye Claire, Nicholas Z Rui, Newlin C Weatherford, Sourav Chatterjee, Giacomo Fragione, Carl L Rodriguez, Mario Spera, and Frederic A Rasio (2020). “Modeling Dense Star Clusters in the Milky Way and Beyond with the CMC Cluster Catalog”. *The Astrophysical Journal Supplement Series* 247.2, p. 48.
- Kroupa, Pavel (1995). “The dynamical properties of stellar systems in the Galactic disc”. *Monthly Notices of the Royal Astronomical Society* 277.4, pp. 1507–1521.
- (2001). “On the variation of the initial mass function”. *Monthly Notices of the Royal Astronomical Society* 322.2, pp. 231–246.
- Kulkarni, SR, Hut, Piet, and Steve J McMillan (1993). “Stellar black holes in globular clusters”. *Nature* 364.6436, pp. 421–423.
- Leigh, Nathan, Alison Sills, and Christian Knigge (2007). “Where the blue stragglers roam: searching for a link between formation and environment”. *The Astrophysical Journal* 661.1, p. 210.
- Leigh, Nathan WC, Mirek Giersz, Michael Marks, Jeremy J Webb, Arkadiusz Hypki, Craig O Heinke, Pavel Kroupa, and Alison Sills (2015). “The state of globular clusters at birth–II. Primordial binaries”. *Monthly Notices of the Royal Astronomical Society* 446.1, pp. 226–239.

- Lützgendorf, Nora, Holger Baumgardt, and JMD Kruijssen (2013). “N-body simulations of globular clusters in tidal fields: Effects of intermediate-mass black holes”. *Astronomy & Astrophysics* 558, A117.
- Maliszewski, Konrad, Mirek Giersz, Dorota Gondek-Rosińska, Abbas Askar, and Arkadiusz Hypki (2021). “MOCCA-SURVEY Database II—Properties of Intermediate Mass Black Holes escaping from star clusters”. *arXiv preprint arXiv:2111.09223*.
- Mann, Christopher R, Harvey Richer, Jeremy Heyl, Jay Anderson, Jason Kalirai, Ilaria Caiazzo, Swantje D Möhle, Alan Knee, and Holger Baumgardt (2019). “A Multimass Velocity Dispersion Model of 47 Tucanae Indicates No Evidence for an Intermediate-mass Black Hole”. *The Astrophysical Journal* 875.1, p. 1.
- Mapelli, Michela (July 2016). “Massive black hole binaries from runaway collisions: the impact of metallicity”. *MNRAS* 459.4, pp. 3432–3446.
- (2017a). *Core Collapse and Reversal*. URL: <http://web.pd.astro.it/mapelli/2017dynamics2.pdf>.
- (Sept. 2017b). *Dynamical processes induced by mass spectrum*. URL: <http://web.pd.astro.it/mapelli/2017dynamics4.pdf>.
- (2017c). *Dynamics of Stars and Black Holes in Dense Stellar Systems*.
- Messier, Charles (1784). “Catalogue des Nebuleuses et des amas d’ttoiles Connais”. *Temps1784*, pp. 227–269.
- Miller, M. Coleman and Edward JM Colbert (2004). “Intermediate-mass black holes”. *International Journal of Modern Physics D* 13.01, pp. 1–64.
- Miller, M. Coleman and Douglas P. Hamilton (Feb. 2002). “Production of intermediate-mass black holes in globular clusters”. *MNRAS* 330.1, pp. 232–240.
- Miller-Jones, James CA et al. (2015). “Deep radio imaging of 47 Tuc identifies the peculiar X-ray source X9 as a new black hole candidate”. *Monthly Notices of the Royal Astronomical Society* 453.4, pp. 3918–3931.
- Morscher, Meagan, Bharath Pattabiraman, Carl Rodriguez, Frederic A Rasio, and Stefan Umbreit (2015). “The dynamical evolution of stellar black holes in globular clusters”. *The Astrophysical Journal* 800.1, p. 9.
- Pattabiraman, Bharath, Stefan Umbreit, Wei-keng Liao, Alok Choudhary, Vassiliki Kalogera, Gokhan Memik, and Frederic A Rasio (2013). “A parallel Monte Carlo code for simulating collisional N-body systems”. *The Astrophysical Journal Supplement Series* 204.2, p. 15.
- Paust, Nathaniel EQ et al. (2010). “The ACS survey of galactic globular clusters. VIII. Effects of environment on globular cluster global mass functions”. *The Astronomical Journal* 139.2, p. 476.
- Pavlik, Václav, Tereza Jeřábková, Pavel Kroupa, and Holger Baumgardt (2018). “The black hole retention fraction in star clusters”. *Astronomy & Astrophysics* 617, A69.
- Peñaloza, Francisco, Peter Pessev, Sergio Vásquez, Jura Borissova, Radostin Kurtev, and Manuela Zoccali (2015). “Chemical Abundances of the Highly Obscured Galactic Globular Clusters 2MASS GC02 and Mercer 5”. *Publications of the Astronomical Society of the Pacific* 127.950, p. 329.
- Perera, BBP, BW Stappers, AG Lyne, CG Bassa, Ismaël Cognard, Lucas Guillemot, Michael Kramer, Gilles Theureau, and Grégory Desvignes (2017). “Evidence for an intermediate-mass black hole in the globular cluster NGC 6624”. *Monthly Notices of the Royal Astronomical Society* 468.2, pp. 2114–2127.
- Peterson, Charles J and Ivan R King (1975). “The structure of star clusters. VI. Observed radii and structural parameters in globular clusters.” *The Astronomical Journal* 80, pp. 427–436.
- Piotto, Giampaolo et al. (2004). “Relative frequencies of blue stragglers in galactic globular clusters: Constraints for the formation mechanisms”. *The Astrophysical Journal* 604.2, p. L109.

- Portegies Zwart, Simon F., Holger Baumgardt, Piet Hut, Junichiro Makino, and Stephen L. W. McMillan (Apr. 2004). “Formation of massive black holes through runaway collisions in dense young star clusters”. *Nature* 428.6984, pp. 724–726.
- Puls, Joachim, Jorick S. Vink, and Francisco Najarro (Dec. 2008). “Mass loss from hot massive stars”. 16.3-4, pp. 209–325.
- Sarajedini, Ata et al. (2007). “The ACS survey of galactic globular clusters. I. Overview and clusters without previous Hubble Space Telescope photometry”. *The Astronomical Journal* 133.4, p. 1658.
- Sedda, Manuel Arca, Abbas Askar, and Mirek Giersz (2019). “MOCCA-SURVEY Database I. Intermediate mass black holes in Milky Way globular clusters and their connection to supermassive black holes”. *arXiv preprint arXiv:1905.00902*.
- Shishkovsky, Laura et al. (2018). “The MAVERIC Survey: A Red Straggler Binary with an Invisible Companion in the Galactic Globular Cluster M10”. *The Astrophysical Journal* 855.1, p. 55.
- Sollima, Antonio and Holger Baumgardt (2017). “The global mass functions of 35 Galactic globular clusters: I. Observational data and correlations with cluster parameters”. *Monthly Notices of the Royal Astronomical Society* 471.3, pp. 3668–3679.
- Spitzer, LYMAN (1987). “Dynamical evolution of globular clusters((Book))”. *Princeton, NJ, Princeton University Press, 1987, 191*.
- Strader, Jay, Laura Chomiuk, Thomas J Maccarone, James CA Miller-Jones, and Anil C Seth (2012). “Two stellar-mass black holes in the globular cluster M22”. *Nature* 490.7418, pp. 71–73.
- Trenti, Michele and Roeland van der Marel (2013). “No energy equipartition in globular clusters”. *Monthly Notices of the Royal Astronomical Society* 435.4, pp. 3272–3282.
- Wang, Long, Rainer Spurzem, Sverre Aarseth, Mirek Giersz, Abbas Askar, Peter Berczik, Thorsten Naab, Riko Schadow, and MBN Kouwenhoven (2016). “The DRAGON simulations: globular cluster evolution with a million stars”. *Monthly Notices of the Royal Astronomical Society* 458.2, pp. 1450–1465.
- Weatherford, Newlin C, Sourav Chatterjee, Kyle Kremer, and Frederic A Rasio (2020). “A Dynamical Survey of Stellar-mass Black Holes in 50 Milky Way Globular Clusters”. *The Astrophysical Journal* 898.2, p. 162.
- Weatherford, Newlin C, Sourav Chatterjee, Carl L Rodriguez, and Frederic A Rasio (2018). “Predicting Stellar-mass Black Hole Populations in Globular Clusters”. *The Astrophysical Journal* 864.1, p. 13.
- Webb, Jeremy J, Enrico Vesperini, Emanuele Dalessandro, Giacomo Beccari, Francesco R Ferraro, and Barbara Lanzoni (2017). “Modelling the observed stellar mass function and its radial variation in galactic globular clusters”. *Monthly Notices of the Royal Astronomical Society* 471.4, pp. 3845–3855.
- Wu, Wenbo and Gang Zhao (2021). “Mass Segregation as a New Indicator of Binary, IMBH, and Stellar-mass Black Hole Systems in Globular Clusters”. *The Astrophysical Journal* 908.2, p. 224.
- Ye, Claire S, Kyle Kremer, Carl L Rodriguez, Nicholas Z Rui, Newlin C Weatherford, Sourav Chatterjee, Giacomo Fragione, and Frederic A Rasio (2021). “Compact Object Modeling in the Globular Cluster 47 Tucanae”. *arXiv preprint arXiv:2110.05495*.

Chapter 5

Appendices

Appendix A

5.1 Influence radii and luminous binaries

As stated in Section. 4.1.4 other parameters can also probe the segregation of a cluster among observable populations. Fig. 5.1 depicts the 50 % observable binary radius as a function of the A_{31}^+ parameter, colour coded by the influence radius of BHs in the system. As expected, smaller influence radii are connected to weaker dynamical heating of BHs, leading to larger segregation values. For our models, the influence radius of IMBH models is generally < 1 pc; however, clusters hosting very massive IMBHs in comparison to their mass can indeed possess larger influence radii that can quench the segregation values. Since the distribution of binaries directly connects to the heating of BHs, the binary radius increases with the influence radius and the number of BHs retained.

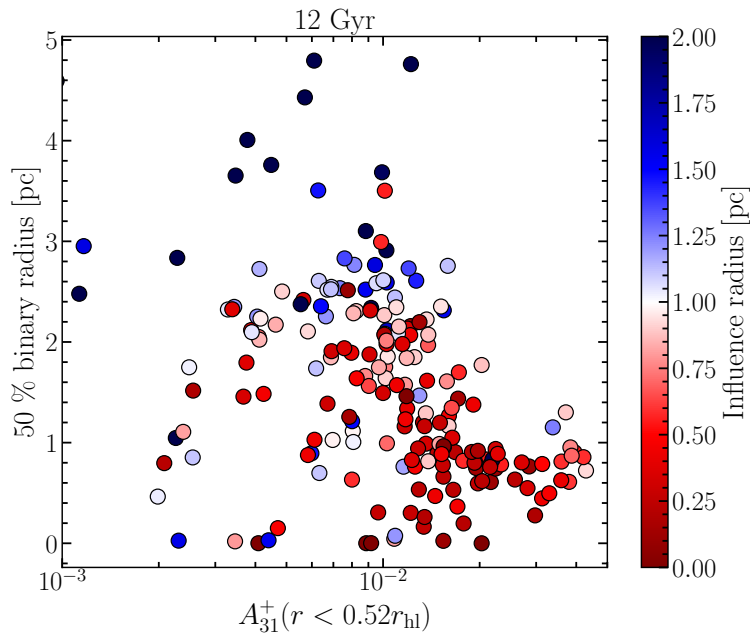


Figure 5.1: Correlation of mass segregation and the 50 % binary radius of clusters. The colour bar indicates the influence radius of the central BHs for each model in the MSD II.

5.2 Radial distributions

Here, we show the cumulative radial distributions of more stellar populations for the reader to compare their segregation and numbers. The cumulative radial distributions of the various stellar populations defined in Fig. 2.1 can be seen in Fig. 5.2. The top left panel indicates single stellar populations for the IMBH cluster model defined in Table. 2.4. The top right panel indicates binary populations. The few BHs retained in this model tend to distribute far out in the cluster, except for the IMBH, which is located in the cluster’s core. Other heavy components dominate the innermost core, such as NS (grey) and giants (dashed red). There is a clear segregation difference between the various MS populations, with the heaviest population (purple line) showing much stronger segregation than their lighter companions (orange and blue lines). A zoom-in inside the observational core radius reveals that the populations that are most significant in number (MS and WDs) have some or a few components extremely close to the centre, presumably feeding the IMBH with mass. A similar trend is observed in the binary populations in the top right panel, where the WD and RG binaries show the strongest segregation.

As opposed to the IMBH model, we see apparent differences in the bottom panels, which shows the same properties, but for the BHS cluster model in Table. 2.4. Most notably is the clear separation between the numerous BHs, dominating the innermost pc. We still notice the trend that heavier objects are more segregated than lighter ones, although it is evident that the dynamical heating from the central BHs mixes the rest of the populations. In other words, the “gap” between populations is smaller, which is especially apparent when comparing the various MS populations. For the binary populations, there are slightly larger numbers of binaries present. The numerous BHs can interact with these binaries, and if they are soft enough, these can disrupt or be ejected. Since the initial half-mass radius is ≈ 2.5 times larger, in this case, the escape velocity is reduced, and the probability for soft binaries to escape is increased. Despite this, the presence of the massive IMBH generates far more dynamical interactions in the core that can disrupt, eject or merge even the hardest binaries and hence, the binary populations are more depleted here. As seen in Fig. 3.19, binaries are not only depleted in absolute numbers, but the fraction of binaries is also lower for the IMBH model at 12 Gyr. We retain some BBH in the BHS model, while in the IMBH case, the deep potential and large velocity dispersion near the centre disrupt most of these binaries in the system, or they have merged with the IMBH.

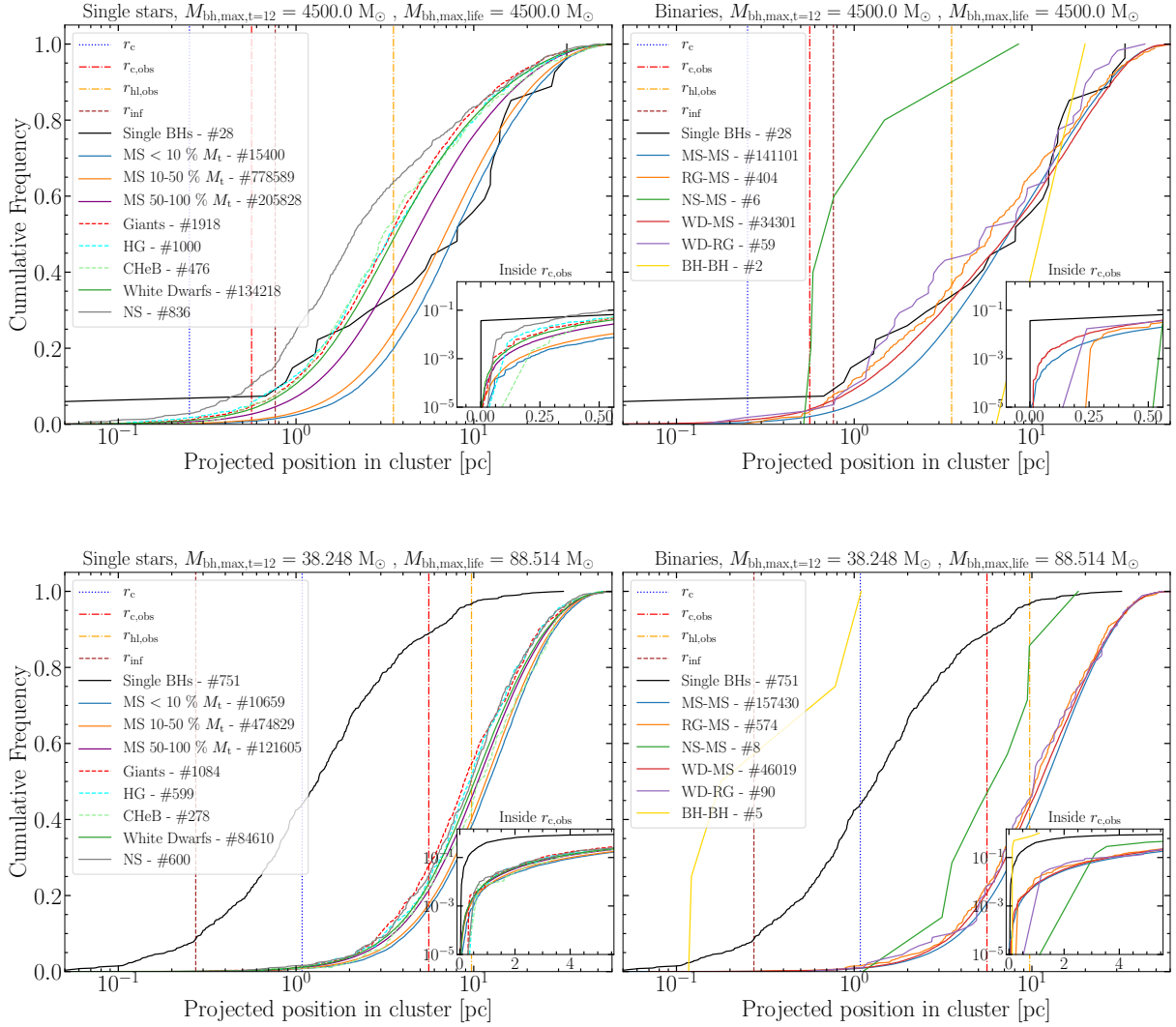


Figure 5.2: Radial distribution of various stellar populations from the MSD II as a function of the projected position in the cluster for the two clusters in Table 2.4. Top rows indicate the IMBH model, while the bottom row shows the BHS. Vertical lines indicate several various radii in the clusters. Note here that M_t stands for the turnoff mass of the specific cluster considered, $M_{\text{bh,max,t=12}}$ is the mass of the most massive BH at 12 Gyr and $M_{\text{bh,max,life}}$ is the most massive BH present in the cluster during its evolution. The left panels indicate single stars, and the right panels indicate binaries. In the giants and WD populations, we include all their different types (c.f Fig. 2.1). We include an inset plot showing the various distributions inside the observational core radius.

5.3 Observational signatures

Figs. 5.3 and 5.4 show further comparisons between the MSD II models with observed data. They display the observed cluster masses as a function of the fraction of the core- and half-light radius in addition to cluster mass as a function of central escape velocity. For the data available in the Harris (2010) catalogue, cluster masses are derived assuming a mass-to light ratio $M/L = 2$. The same quantities are extracted from Baumgardt et al. (2020). For the latter catalogue, we also extract the escape velocities. Together, they form the grey circles in the figures. Green crosses denotes clusters where segregation values are available.

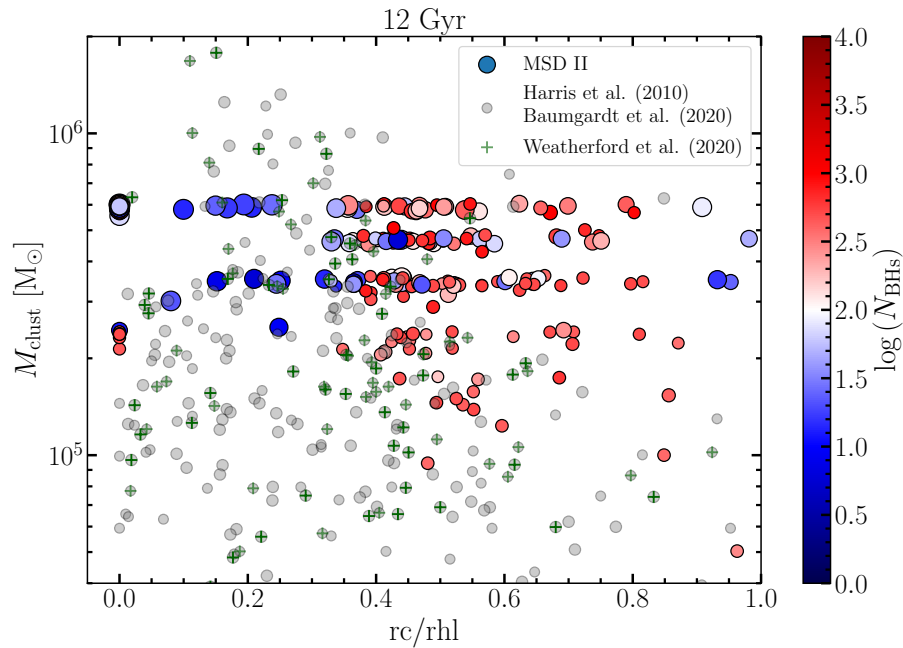


Figure 5.3: The mass of simulated clusters as a function of the ratio between the core- and half-light radius. In colour-gradient dots we show the MSD II simulation values, coloured after the number of BHs retained.

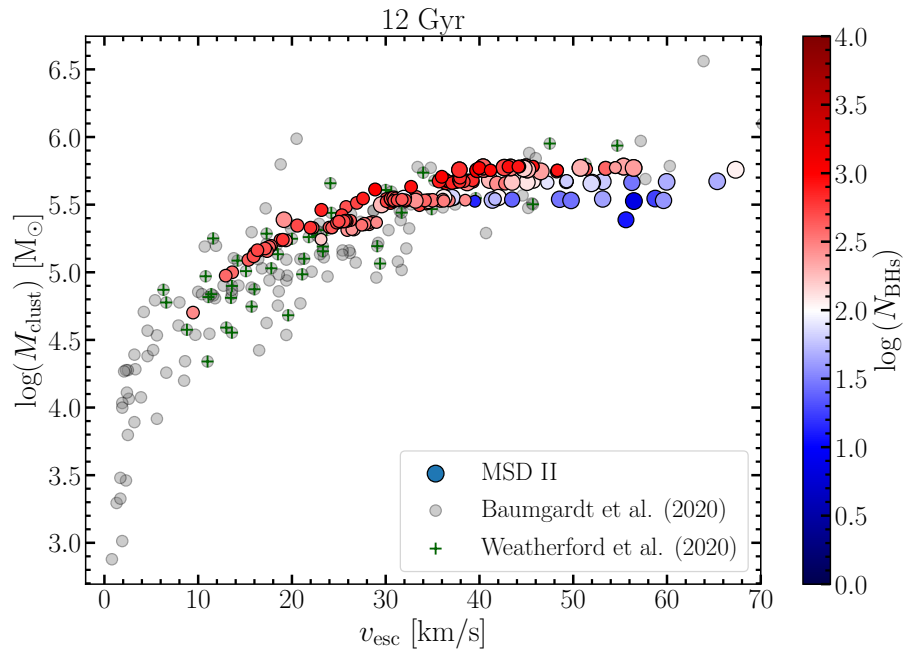


Figure 5.4: Analogous to Fig. 5.3 but instead showing the logarithm of the mass of the clusters as a function of the clusters' central escape velocities. Here, only catalogued data from Baumgardt et al. (2020) is included.

Appendix B

5.4 Numbers and masses of BHs and IMBHs for Δ_{r50}

The following table indicates cluster properties and predictions of BH numbers and masses of potential IMBHs in observed clusters based on the Δ_{r50}^{13} parameter. The estimates can be compared to Table 3.1, which indicates similar estimates, but based on A_{31}^+ .

Table 5.1: Similar to Table 3.1 but instead based on the fit for the Δ_{r50}^{13} .

Cluster Name	Number of black holes	IMBH mass [M_{\odot}]	Δ_{r50}^+	$\pm 1\sigma$	M/L [$M_{\odot} L_{\odot}^{-1}$]	r_{hl} [pc]	$L_{cluster}$ [$10^2 L_{\odot}$]	$\log_{10} \Sigma_c$ [$L_{\odot} pc^{-2}$]
NGC 104*	17^{+49}_{-32}	4403^{+13710}_{-3333}	0.062	0.009	1.96	3.64	45.6	4.34
NGC 288	90^{+123}_{-52}	0^{+0}_{-0}	0.015	0.002	2.16	5.83	4.32	2.43
NGC 1261	40^{+161}_{-32}	0^{+0}_{-0}	0.035	0.014	1.63	3.25	11.2	3.79
NGC 1851	10^{+23}_{-7}	6062^{+14812}_{-4301}	0.104	0.03	1.66	1.75	19.2	5.32
NGC 2298	37^{+87}_{-26}	0^{+0}_{-0}	0.032	0.007	1.91	2.4	2.92	3.55
NGC 2808	13^{+32}_{-9}	5062^{+12762}_{-3624}	0.058	0.013	1.51	2.45	57.2	4.62
NGC 3201*	63^{+155}_{-44}	0^{+0}_{-0}	0.013	0.003	2.16	3.8	7.41	3.32
NGC 4147	20^{+57}_{-15}	0^{+0}_{-0}	0.042	0.0015	1.64	2.54	2.38	3.62
NGC 4590	55^{+180}_{-42}	0^{+0}_{-0}	0.014	0.003	1.8	4.43	6.78	2.97
NGC 4833	68^{+171}_{-48}	0^{+0}_{-0}	0.014	0.002	1.74	3.25	11.8	3.49
NGC 5024	25^{+67}_{-18}	0^{+0}_{-0}	0.043	0.01	1.77	6.43	25.7	3.36
NGC 5053	136^{+486}_{-106}	0^{+0}_{-0}	0.012	0.001	2.55	12.37	2.91	1.49
NGC 5272	24^{+64}_{-17}	0^{+0}_{-0}	0.047	0.009	1.61	3.39	25.2	3.87
NGC 5286	9^{+12}_{-5}	6274^{+8381}_{-3588}	0.099	0.019	1.48	2.37	23.9	4.59
NGC 5466	166^{+403}_{-117}	0^{+0}_{-0}	0.004	0.001	1.44	9.53	4.15	1.93
NGC 5904	25^{+62}_{-18}	0^{+0}_{-0}	0.04	0.008	1.81	3.51	21.8	3.86
NGC 5927	49^{+214}_{-39}	0^{+0}_{-0}	0.015	0.011	1.63	3.47	16.9	3.68
NGC 5986	42^{+185}_{-34}	0^{+0}_{-0}	0.021	0.018	1.9	2.77	17.6	3.83
NGC 6093	8^{+10}_{-4}	6682^{+8810}_{-3800}	0.012	0.016	2.08	1.76	16.3	4.53
NGC 6101	213^{+1523}_{-187}	0^{+0}_{-0}	0.002	0.003	2.56	9.56	6.96	2.21
NGC 6144	68^{+183}_{-50}	0^{+0}_{-0}	0.018	0.003	2.49	3.63	3.18	2.88
NGC 6171	51^{+168}_{-30}	0^{+0}_{-0}	0.018	0.004	2.22	2.86	3.38	3.32
NGC 6205	58^{+197}_{-45}	0^{+0}_{-0}	0.021	0.006	2.31	3.46	23.6	3.66
NGC 6218	68^{+193}_{-50}	0^{+0}_{-0}	0.016	0.003	1.92	2.83	5.58	3.34
NGC 6254*	44^{+104}_{-31}	0^{+0}_{-0}	0.022	0.003	1.86	2.97	11.0	3.65
NGC 6304	17^{+65}_{-14}	0^{+0}_{-0}	0.061	0.025	1.57	1.95	8.03	4.38
NGC 6341	14^{+37}_{-10}	5020^{+14364}_{-3720}	0.077	0.023	2.16	2.39	16.3	4.01
NGC 6352	46^{+35}_{-17}	0^{+0}_{-0}	0.028	0.004	2.21	2.88	2.93	3.06
NGC 6366	51^{+154}_{-38}	0^{+0}_{-0}	0.015	0.003	1.71	3.77	2.19	2.58
NGC 6397	15^{+34}_{-10}	4720^{+11372}_{-3335}	0.068	0.004	1.66	2.16	5.82	5.07
NGC 6535	23^{+62}_{-17}	0^{+0}_{-0}	0.062	0.015	2.64	2.67	0.83	3.88
NGC 6541	13^{+34}_{-9}	5103^{+13931}_{-3735}	0.081	0.02	1.75	2.29	16.7	5.07
NGC 6584	33^{+124}_{-26}	0^{+0}_{-0}	0.038	0.018	1.34	3.44	7.61	3.24
NGC 6624	8^{+11}_{-4}	7133^{+10543}_{-4254}	0.147	0.051	2.09	2.33	7.47	4.37
NGC 6637	19^{+76}_{-15}	0^{+0}_{-0}	0.061	0.026	1.72	2.41	9.01	3.76
NGC 6652	12^{+31}_{-8}	5464^{+14887}_{-3997}	0.09	0.032	1.8	1.47	2.67	4.10
NGC 6656*	44^{+96}_{-30}	0^{+0}_{-0}	0.026	0.002	2.05	3.15	23.2	3.99
NGC 6681	12^{+28}_{-8}	5386^{+13007}_{-3808}	0.08	0.026	1.84	2.14	6.30	5.12
NGC 6715	12^{+23}_{-8}	5346^{+10856}_{-3582}	0.104	0.009	2.1	3.58	84.8	4.92
NGC 6717	18^{+63}_{-14}	0^{+0}_{-0}	0.064	0.02	1.55	3.65	2.31	3.89
NGC 6723	74^{+202}_{-54}	0^{+0}_{-0}	0.012	0.005	2.01	3.55	8.81	3.29
NGC 6752	16^{+41}_{-11}	4495^{+12015}_{-3271}	0.069	0.013	2.34	2.87	11.8	4.83
NGC 6779	42^{+115}_{-30}	0^{+0}_{-0}	0.029	0.007	1.74	2.95	10.7	3.59
NGC 6809	81^{+167}_{-54}	0^{+0}_{-0}	0.01	0.002	2.06	4.58	9.37	2.95
NGC 6838	90^{+152}_{-56}	0^{+0}_{-0}	0.015	0.004	1.72	3.41	3.81	2.87
NGC 6934	17^{+44}_{-13}	4403^{+17551}_{-3520}	0.06	0.024	1.52	2.95	8.95	3.46
NGC 6981	213^{+2211}_{-195}	0^{+0}_{-0}	0.005	0.004	1.35	4.14	5.10	2.89
NGC 7078	9^{+10}_{-5}	6378^{+7639}_{-3476}	0.111	0.009	1.58	2.03	40.1	5.85
NGC 7089	9^{+11}_{-5}	6344^{+7878}_{-3514}	0.109	0.012	1.75	3.04	35.4	4.34
NGC 7099	13^{+33}_{-9}	5062^{+13302}_{-3666}	0.081	0.017	1.91	2.54	7.49	4.79